Modeling of material and architectural quality of trabecular bone

Dissertation

zur Erlangung des akademischen Grades
Doktor der Naturwissenschaften (Dr. rer. nat.)
in der Wissenschaftsdisziplin Theoretische Physik

eingereicht an der
Mathematisch-Naturwissenschaftlichen Fakultät
der Universität Potsdam

angefertigt am
Max-Planck-Institut für Kolloid- und Grenzflächenforschung

von

Davide Ruffoni
geboren am 11. Januar 1979 in Varese, Italien

Potsdam, im September 2007

Contents

Abstract

Trabecular bone is the spongy type of bone found in humans inside vertebrae and in long bones close to joints. In this thesis the biological material trabecular bone is investigated theoretically at two different levels of its structural hierarchy. In the first part, the focus is on the bone material which evolves in time as a result of two processes. During the process of remodeling small bone packets are continuously resorbed from the bone surface and new packets are deposited. In the mineralization process the mineral content in the initially unmineralized new bone packet increases. As a consequence, trabecular looks like a "patchwork" of bone packets with different mineral content. This heterogeneity of the mineral content can be characterized by a frequency distribution of the mineral content, called the bone mineralization density distribution (BMDD). The BMDD describes the volume of bone with a given mineral content detected in a bone sample. A partial differential equation is developed to describe how remodeling and mineralization influences the amount and the homogeneity of the mineral content. The model is first used to extract information on the mineralization kinetics from the experimentally measured peak-shaped BMDD of healthy humans. The model is then applied to more clinically relevant questions. The time evolution of the BMDD was predicted and compared with experimental data for the two cases of accelerated bone turnover, as typically observed in osteoporosis, and slowed turnover, as caused by standard medications used to treat osteoporosis. Important dynamical effects are discovered, leading to a transient homogenization of the mineral content in the case of turnover reduction, while the opposite is true for increased turnover.
In the second part of the thesis, the connection between trabecular bone architecture and its mechanical performance is investigated. The trabecular architecture is idealized as a cellular solid consisting of a two dimensional network of cylindrical beams (trabeculae). The aim is to find a mechanical description of the structure which allows to identify mechanically weak elements. For this purpose the cellular structure is viewed as consisting of different "nodes", where a node is defined by a set of trabeculae joined together at a junction point. The mechanical behavior of a node in two different environments is compared. Either the node is part of a periodic

lattice which is constructed with identical copies of itself, or acts as a defect in a regular isotropic lattice. The comparison demonstrates that in addition to the specific geometry of the node, the neighboring nodes also strongly influence its deformation behavior. Only in special cases is the geometrical information of the node enough to predict its mechanical behavior.

Chapter 1

Motivations

Bone has attracted the attention of physicists and engineers for centuries, with one of the first examples being Galileo's analysis of the aspect ratio of bones from different sized animals [1]. Nowadays, there are at least two prominent characteristics that attract the interest of the material physics community. Firstly, its self-organized hierarchical structure, which goes from the macroscopic (cm) down to the molecular (nm) length scale (see Fig. 1.1). And secondly, its dynamical nature which enables bone to maintain and adapt to its mechanical environment. To understand how bone structure relates to the observed mechanical properties it is fundamental to investigate the behavior at each single hierarchical level. In addition, a more difficult and still unsolved question, is how the different levels interact. Basic biological processes, which enable bone to adapt to its environment, are bone remodeling and bone mineralization. In bone remodeling old or damaged bone is continuously substituted with new unmineralized bone and during bone mineralization new bone progressively increases its mineral content and thus its stiffness. In addition to biochemical signals, the main factor controlling the organization of bone structure is the local mechanical load. In this thesis bone is studied from two different points of view. Applying a "dynamical" framework, in the first part it is analyzed how, due to bone remodeling and mineralization, the bone material evolves with time. In a more "static" approach, in the second part, single "snapshots" of the network-like architecture of trabecular bone are investigated in terms of their mechanical performance.
A further motivation of this work stems from the alterations of the complex time evolving structure of bone by diseases, which in turn could decrease its mechanical performance. Most of these diseases are poorly understood, both from a medical and a materials science point of view. Although there is a large amount of data available from clinical studies of diseases in bone, it still remains to interpret the data in terms of the underling physics, which can in turn be used to get quantitative predictions of the mechanical response of bone. This thesis is aimed to bridge the gap between

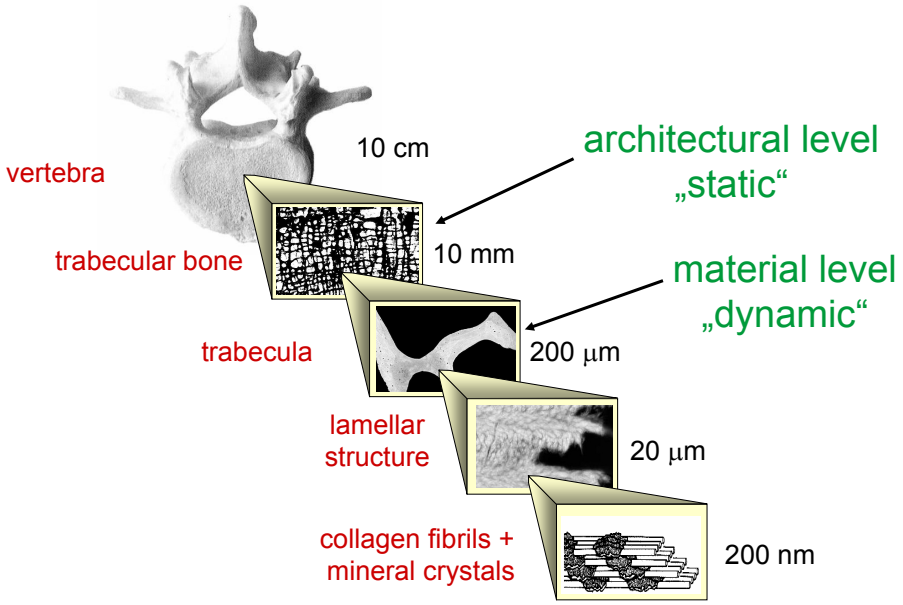

Figure 1.1: The hierarchical structure of bone extends over length scales of cm to mm. For example, the macroscopic scale (cm) includes a whole vertebra. At a lower scale (mm) trabecular bone can be distinguished from compact bone. Compact bone (not shown) is dense whereas trabecular bone exhibits a spongy architecture with a high porosity. Struts of the spongy architecture, called trabeculae are seen on a lower scale (μm) and their lamellar structure is investigated at an even lower scale. Eventually, at the microscopic level (nm) bone is viewed as nanocomposite of a soft but tough protein matrix and stiff but brittle mineral crystals. The two hierarchical levels, the thesis will focus on, are marked.

medicine and material physics by developing simple physical models of bone which can be used by the medical community.
Osteoporosis is a particularly important disease to study both because of its high prevalence in the aging community and for the dramatic reduction in the life quality of the people affected. An osteoporotic skeleton is characterized by a deterioration of mass, architecture and material properties, which manifest themselves as an increased probability for bone fractures.
Currently the main diagnostic method to assess osteoporosis is to measure *in vivo* the amount of bone. This is performed with a technique called dual-energy X-ray absorptiometry (DXA) which estimates from the amount of the adsorbed radiation how much bone is present. The result of these measurements, corrected by body size, is the bone mineral density (BMD) characterizing with a single scalar value the bone under investigation. According to the instruction of the World Health Organization

(WHO), a reference value for healthy people as a function of age is established and deviation of 2.5 standard deviation or more below this value defines an osteoporotic patient. When thinking at the intricate structure of bone it is obvious that there are several limitations in estimating the bone mechanics and in particular bone strength using BMD only. Estimating the risk of fracture with BMD does not identify all the people at risk and does not tell who will and who will not have a non traumatic fracture. The poor predictive power of BMD is also evident from the effects of an antiresorptive therapy where the significant reduction observed in fracture risk has almost no correlation with the small increase in BMD. In addition to bone mass the mechanical performance of bone depends, at the material level, on the collagen matrix, the mineral content and their interactions and spatial arrangement. At a bigger length scale, bone mechanics is more influenced by the intricate trabecular architecture. In turn, all the hierarchical levels are influenced by the way and the rate at which bone is remodeled and repaired. All these factors, which are not directly entering in the bone mass or BMD, are referred as bone quality.

The following two chapters of this thesis (chapters 2 and 3) focus on the material quality of bone, and the influence of the remodeling and mineralization processes on the heterogeneity of the mineral content. A partial differential equation is developed to describe these processes and is solved for scenarios of medical importance. In the second part of the work (chapters 4 and 5), the hierarchical level is changed from that of the material to that of the bone architecture. Rather than focusing on the dynamics of how the architecture evolves, we concentrate on the mechanical response of given architectures at a single point in time. The mechanics of idealized trabecular architectures are evaluated using geometric descriptors that extend the approaches based on just the bone mass. For this problem analytical solutions are compared with numerical results obtained using commercial finite element software.

The thesis will show that is sufficient to use relatively simple physical tools to extract "knowledge" from the big amount of available experimental data of human bone. Since the aim of our work must be to reach the medical community, an effort in publishing and presenting, has been made to make our models and results accessible and understandable to this community which normally communicates in a different language.

Chapter 2

Bone material quality

This chapter introduces the material which makes up bone and the processes of remodeling and mineralization, which are necessary to understand the simulational work described in chapter 3.
Bone material is composed by three very different constituents: a soft protein matrix, stiff mineral crystals and water. Even if the relative amount of these three components varies among bone types [2] approximately 35% of the total bone weight is given by the organic collagen component, 45% by the inorganic mineral and the remaining 20% by water [3]. The individual properties of collagen and mineral are shortly reviewed in sections 2.1 and 2.2, respectively. The interaction, at the nanometer level, of these two components leads to a nanocomposite material with remarkable mechanical properties, as explained in section 2.3. In addition to an intricate hierarchical structure, bone is a living material in the sense that it is continuously resorbed and reformed in a process called bone remodeling. In section 2.4 the main features of this biological process are explained. After new unmineralized bone is formed, it starts to mineralize by a formation of mineral crystals inside the protein matrix. The current understanding of this complex phenomenon is summarized in section 2.5. Due to bone remodeling, the mineralization of the bone matrix is far from uniform and evolves as a function of different remodeling scenarios as explained in section 2.6. In that introductory section special emphasis is devoted to the problem of measuring bone remodeling and to the changes in bone remodeling occurring during menopause and following clinical treatments. The reason for introducing those more clinical aspects, is that the model presented in the next chapter, aims to explain and simulate changes in the material properties - in term of mineralization of the bone matrix - which are observed experimentally.

2.1 Collagen matrix

Collagen is the most abundant protein in the human body. It is a "structural protein" in the sense that it provides tissues the ability to withstand mechanical forces. Different types of collagen can be found in almost all connective tissues: bone, skin, tendon, ligament, cornea and blood vessels. In bone, type I collagen comprises something like 85-90% of the total protein content [4]. The basic building block of the collagen fibers is the collagen molecule. It has a rod-like shape of about 300 nm long and 1.5 nm width and it is composed of three similar polypeptide chains that are folded together to form a triple helix. The triple-helical molecules self assemble to form fibrils in a staggered fashion (see Fig. 2.1). Along the axial direction adjacent molecules are shifted by a period D=67 nm that gives rise to a pattern of gap zones (35 nm long) and overlap zones (32 nm long) within the fibril [5]. This pattern was shown experimentally with TEM [6] and with neutron scattering [7]. The gap zones are fundamental when thinking about the mineralization of the collagen fibrils since they probably act as nucleation sites for the mineral particles [6].

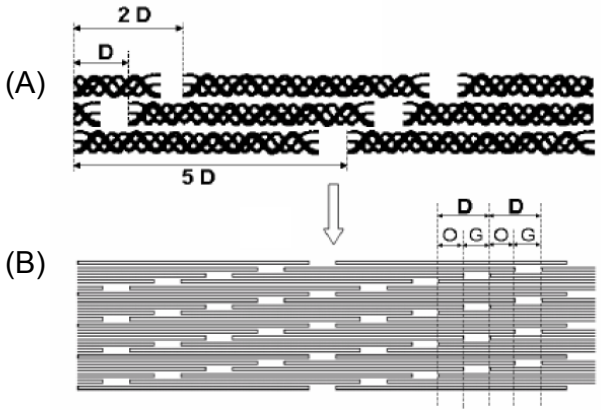

Figure 2.1: Self-assembly of collagen fibrils (after [8]). (A) the collagen molecules self-assemble with a staggering period of D. (B) this staggering results in a periodic density variation along the fibril axis. In the stripes labeled O, there is an overlap of all molecules. In the stripes labeled G (gap region), one molecule out of five is missing and the density is accordingly smaller.

The collagen matrix is stabilized by covalent cross-links between the collagen molecules which can be investigated, for instance, using Fourier-transform infrared microspectroscopy (microFTIR) [9]. Cross-link changes during aging and osteoporosis negatively correlate with bone mechanical performance [10, 11, 12].

2.2 Mineral crystals

In addition to the organic matrix, bone contains inorganic mineral. The bone mineral crystals are nanocrystals of calcium phosphate, analogous to the geologic mineral hydroxyapatite [$Ca_{10}(PO_4)_6(OH)_2$]. Bone mineral always contains impurities (e.g., phosphate ions, PO_4^{3-}, are often replaced by carbonate groups, CO_3^{2-}) and vacancies (e.g., missing OH^-)[13, 14]. Those small imperfections increase the solubility of bone crystals which are important also for the equilibrium of ions (calcium, phosphate and magnesium) in the body. Mineral crystal composition can be determined using spectroscopy methods like microFTIR [15] and Raman [16]. In addition to the atomic defects, bone mineral can incorporate also non-collagenous protein [17]. The precise role of those organic molecules is still not clear and most probably they are involved in regulating the mineralization process [14].
The shape of the mineral crystals is dictated by the well defined environment of the collagen matrix in which they nucleate and grow. As shown by transmission electron microscopy (TEM) [18, 19] and small-angle X-ray scattering (SAXS) [20, 13], mature bone crystals are flat plates with an average length of 50 nm, a width of 25 nm and a maximum thickness of 4 nm. In general those dimensions may be influenced by intrinsic (related to the composition and arrangement of the matrix) and extrinsic (related to age, health, diet, etc.) factors [21]. The longest dimension of the crystals correspond to the c-axis and this is aligned parallel to the collagen fibrils, the thickness of the mineral being limited by the available space within the hole zones [20]. Crystals are periodically located along the collagen fibrils, with an approximate period of 67 nm [22], which corresponds to the staggering distance of adjacent collagen molecules (see Fig. 2.2). The equatorial spacing between collagen molecules can vary from 1.6 nm in non-mineralized wet fibrils to 1.1 nm in dried conditions, where as in mineralized wet bone an intermediate value of 1.25 nm was found [24]. This suggests a very close packing of the collagen molecules when clusters of mineral crystals replace the water within the fibril [25].
An interesting consequence is the possibility to estimate the average amount of mineral content of the mineralized collagen matrix, starting from the knowledge of the amount of water which can be replaced by the mineral particles. The space occupied by free water within the fibril is 48 vol% in the gap zone and 35 vol% in the overlap zone. Since the fibril consists in 60% of gap and 40% of overlap zones, a value of the mineral content of 43 vol% can be reached [13].
The mechanical properties of bone crystals are quite difficult to compute due to their small size. An indication of the stiffness comes form the Young's modulus of large single crystals of hydroxyapatite which is 114 GPa [4]. In addition, combining *in situ* tensile testing with synchrotron X-ray diffraction and scattering, it was shown that the fracture strain of mineral crystals in bone is twice the fracture strain of bulk

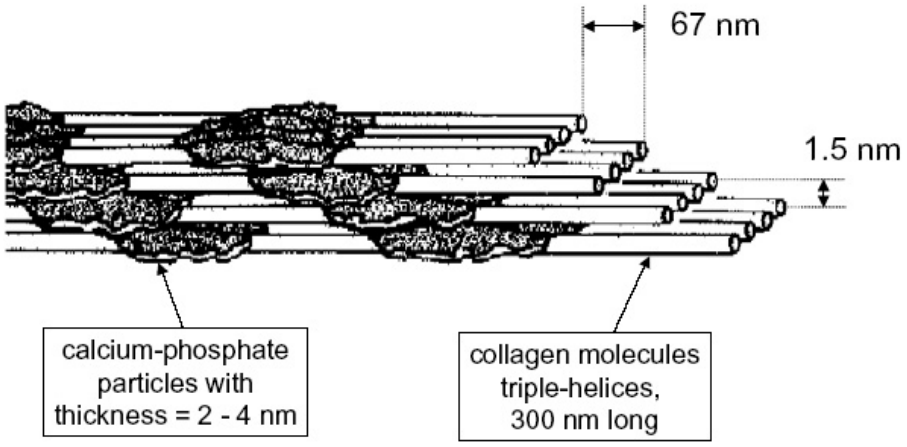

Figure 2.2: Sketch of a probable arrangement of the mineral particles in collagen fibrils. The flat plates mineral crystals are arranged parallel to each other and parallel to the collagen fibrils. The proposed nucleation of mineral particles inside the gap zone of collagen fibrils causes the staggering of the crystals (from [23]).

apatite [26]. Crystal properties like size, composition and orientation are known to influence the mechanics of bone. In aged bone, for instance, large crystal size are often found and this is associated with increased brittleness of bone [21]. Crystal orientation and arrangement in the collagen matrix are key factors for the properties of bone material (stiffness and resistance to fracture in particular), as explained in the following section.

2.3 Collagen-mineral nanocomposite

In bone, stiff mineral nanoparticles are embedded in a tough polymeric matrix. From a materials scientist point of view it is surprising to see how bone actually manages to combine the "best" properties of both constituents, namely the high Young's modulus of the mineral and the high toughness of the matrix. This can be best visualized in an Ashby-map [27, 28] obtained by plotting stiffness versus toughness (defined as fracture energy) of collagen, hydroxyapatite on the one hand, and bone-like materials on the other (see Fig. 2.3).

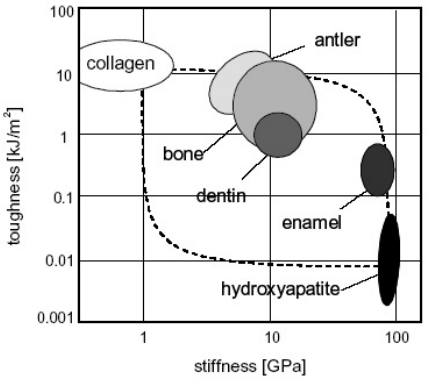

Figure 2.3: Ashby-map of the stiffness versus toughness for collagen, pure hydroxyapatite and calcified tissues where the basic building block is the mineralized collagen fibril. The dotted lines bounds the mechanical behavior of the composite materials and are obtained assuming parallel (Voigt) and serial (Reuss) arrangement for the mineral and collagen phases (from [23]).

Hydroxyapatite is very stiff but brittle whereas collagen is two orders of magnitude softer but approximately three orders of magnitude tougher. The behavior of the resulting bone composite cannot be explained by a simple linear (Voigt) or inverse (Reuss) rule of mixtures [29]. In a linear rule of mixtures, where collagen and mineral are loaded in parallel, the composite stiffness is basically the one of the mineral. The weak point of this arrangement is the fact that the strains in the two phases are identical and therefore the toughness is limited by the brittle mineral behavior. Conversely, in the inverse rule of mixture collagen and mineral are viewed in series and the elastic properties are governed by the collagen. In this situation the stresses are identical and therefore the overall possible load is limited by the stress which can be carried by the collagen phase.
A simple mechanical model which is able to explain how to combine stiffness and toughness in composite material, on the base of pure geometrical arguments, has

been introduced by Jäger and Fratzl [29]. The model is based on the staggered arrangement of stiff (mineral) elements embedded in a soft (protein) matrix (see Fig. 2.4).

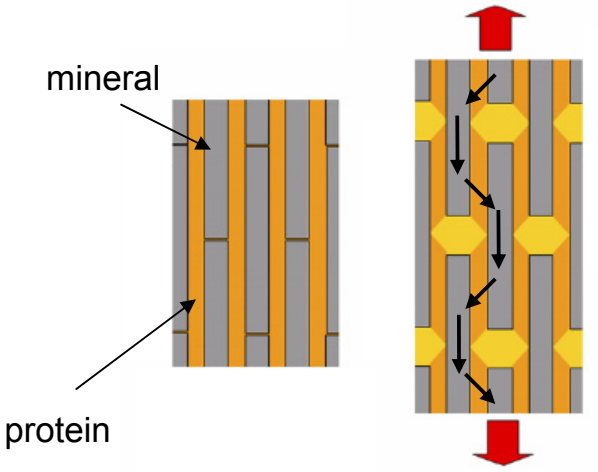

Figure 2.4: Two-dimensional model for mineral crystals arrangement in the collagen matrix. When the system is loaded (on the right), the stiff crystals carry tensile load whereas the thin matrix transfers load via high shear zones between the mineral (adapted from [23]).

With this geometry, under applied tensile load, the mineral platelets carry tensile stresses while the main task of the protein layer is to transfer the load between adjacent mineral crystals by shear. For small deformations, the resulting stiffness E_c, stress σ_c and strain ϵ_c, of the composite material can be expressed as [23, 30, 29]

$$\begin{cases} E_c &= \left(\frac{4(1-\Phi)}{G_p \Phi^2 \rho^2} + \frac{1}{\Phi E_m}\right)^{-1} \\ \sigma_c &= (1-\Phi)\,\sigma_p + \Phi \sigma_m \\ \epsilon_c &= \frac{2}{\rho}\frac{1-\Phi}{\Phi}\eta_p + \epsilon_m \end{cases}, \tag{2.3.1}$$

where E_m, σ_m and ϵ_m are the Young's modulus, tensile stress and tensile strain of the mineral phase; G_p, σ_p and η_p are the shear modulus, tensile stress and shear strain of the protein phase; Φ is the volume fraction of the mineral and ρ is the aspect ratio of the mineral crystals.
The first relation of Eq. 2.3.1 shows that one can compensate for the low stiffness of the protein phase just by increasing the aspect ratio of the mineral crystals. An aspect ratio of ρ=30, for example, could already compensate for a protein phase which is almost three order of magnitude softer than the mineral [23]. The second relation

in Eq. 2.3.1 says that most of the load is carried by the mineral phase which therefore must have a sufficiently high strength. This requirement is matched when mineral particles are very small. In fact numerical calculations showed that when the size of particles is smaller than a critical length - which depends on the surface energy of the particle material and on its theoretical strength - they become flaw-tolerant in the sense that they cannot have defects large enough to reduce their strength in a significant way [30, 23]. A rough estimation of this length for mineral crystal gives 30 nm [30] which is in agreement with the mineral crystals size reported in section 2.2. With the aspect ratio is possible to compensate for the soft protein matrix, however there is a draw back of this simple linear elastic model in that the strain of the composite cannot exceed too much the value of the brittle strain of the mineral, as shown by the third relation of Eq. 2.3.1. To correct for this, one has to consider that beyond a certain critical shear stress, the behavior is not linear anymore since the protein matrix starts to deform plastically. The flow of the protein matrix is the mechanism which allows the nanocomposite to have bigger strains than the mineral particles [31, 26].

2.4 Bone remodeling

In addition to a very smart arrangement of its main components on the nanometer level, bone has another remarkable property. It can self-adapt and self-repair to match the mechanical requirements of its environment. In bone physiology, the term bone remodeling in fact refers to the continuous resorption and deposition of bone carried out by two different cell types: the bone forming cells (osteoblasts) and the bone resorbing cells (osteoclasts). Bone remodeling probably exists for structural and metabolic reasons. From a structural viewpoint remodeling serves to repair microdamage, in order to avoid fatigue effects, and to adapt bone shape and microarchitecture to mechanical loads [32]. The mechanical adaption of bone structure was already proposed from anatomical observation at the end of the 19^{th} century. This is summarized in the so-called Wolff-Roux law which states that bone is deposited where mechanically needed and is resorbed wherever there is no mechanical need [33]. This concept was further developed by Frost who introduced the idea of a "mechanostat", i.e., that a mechanically controlled feedback loop is active in bone and regulates bone mass and architecture [34]. This type of structural remodeling is also known as targeted remodeling [35] in the sense that is targeted toward specific sites that maybe are experiencing particularly high or low strain states or that are maybe damaged by a microcrack.
Bone is the main calcium reservoir in the body and, although calcium ions can enter and leave the skeleton also by other mechanisms [36], remodeling probably is fundamental to regulate the concentration of ions in the extracellular fluids [32]. This does not require that remodeling occurs in a specific site and, as long as the mechanical quality is not compromised, can be carried out in a stochastic manner. The metabolic remodeling is therefore called non-targeted remodeling [35]. During bone remodeling osteoblasts and osteoclasts form a well organized team of cells called basic multicellular unit (BMU) that, in trabecular bone, travels across the bone surface and replace old with new bone. The remodeling process is normally subdivided into 5 phases: resting, activation, resorption, reversal and formation [37]. During the resting phase the surface of bone is covered and protected with lining cells (inactive osteoblasts), therefore no resorption or formation can take place. In the subsequent activation phase osteoclast precursors mature and are ready to resorb bone. Resorption takes place when bone lining cells withdraw, therefore exposing the mineralized bone surface to the action of osteoclasts. These aggressive cells, after attaching at the bone surface, create an acidic environment in order to dissolve both the mineral and the collagen phase. When this step is completed, small cavities called resorption pits with a dept of about 60 μm [38] are left on the trabeculae as fingerprints of osteoclast action. The reversal of the remodeling process takes place when resorption stops and

formation of new bone starts. The main actors of the formation phase are the osteoblasts and their role is to lay down unmineralized collagen matrix (osteoid) into the resorption pits. After deposition, the osteoid starts to mineralize. The mineralization process will be described in detail in the next section. During the formation process, osteoblasts may remain trapped in the bone matrix, where they become osteocytes. Osteocytes are networked with each other and to bone lining cells via small channels called canaliculi. This network is probably important in the maintenance of bone as it is believed to sense mechanical changes and to trigger targeted remodeling [33].
Remodeling is a key factor for the bone mechanical performance since it affects both bone architecture and material. Despite the ongoing clinical debate on which rate of bone remodeling is optimal for bone health [39], it is generally accepted that high remodeling rates as well as absent remodeling can dangerously reduce bone strength [40]. When the trabecular network is remodeled, the characteristic resorption pits generated by the osteoclasts could, from a mechanical point of view, act as stress concentrators, therefore weakening locally the trabecular structure [41]. If the increased remodeling is also accompanied by an imbalance in favor of bone resorption (e.g., osteoporosis) this can result in loss of bone mass by thinning, perforation and disconnection of the trabecular network [42]. Once a trabecula is lost, it is very unlikely that it will be reformed and in general, as we will see in the second part of this thesis, the mechanical competence of bone is reduced more dramatically when bone is lost due to the disappearance than to thinning of trabeculae [43]. On the contrary, low rates of bone remodeling lead to an accumulation of microdamage [44] which could eventually degrade bone toughness as suggested by animal models [45].
At the material level, remodeling influences the mean degree of mineralization, the size and composition of the mineral crystals and the amount of collagen cross-links. A high rate of bone remodeling, for example, reduces the degree of mineralization [46, 47] and therefore the stiffness of bone material. When remodeling slows down, the degree and the homogeneity of mineralization increases, which in turn could result in more brittle bone [48, 13].

2.4.1 How to measure bone remodeling rates

Since remodeling and in particular the remodeling rates (or turnover rates) are important input parameters for the mathematical model which is introduced in the next chapter, the main experimental methods and their limitations in the assessment of those rates should be shortly mentioned. A first indirect method to estimate the rates of bone remodeling is to measure biochemical markers of bone resorption or of bone formation released into the blood. Markers of bone resorption include, for instance, collagen breakdown products. Signs of bone formation are osteocalcin and cleavage products of procollagen synthesis [49]. Assessing bone remodeling with bone markers

is easy to perform but presents strong limitations like a big variability and the lack of specificity for bone since collagen is produced also in other tissues.
A second approach, which however is not that practical since it cannot be performed *in vivo*, is with standard bone histomorphometry [50]. Parameters of bone turnover measured with this technique includes for instance activation frequency (Ac.f), i.e., the frequency at which a given point on the surface undergoes remodeling per unit time, bone formation rate volume referent (BFR/BV) and bone resorption rate volume referent (BRs.R/BV) which are the fraction of total bone formed and resorbed per year, respectively. With this approach it was found that, with "physiological" remodeling rates, 20% of the total trabecular bone volume is remodeled per year [51]. To this corresponds a turnover time (i.e., the time needed to remodel an amount of bone equal to the actual total trabecular bone volume) of 5 years. Finally, a recent method to assess remodeling rates is via synchrotron radiation microtomography (SRμCT) [52]. This imaging method allows also to determine the ratio of low- to high-mineralized bone volume fractions (Bone Mineralization Ratio-Volume: BMR-V) and the ratio of the surface areas (Bone Mineralization Ratio-Surface: BMR-S). Those two quantities have been shown to correlate well with turnover indices from histomorphometry [52].

2.4.2 High and low bone turnover scenarios

Two fundamental clinical situations, where the alteration in the remodeling rates are shown to affect the mineralization pattern, are the increased turnover scenario observed in menopause, which could lead to osteoporosis, and the subsequent treatments to reduce the remodeling rates. The enormous interest in those situations is also evident from the fact that all the major pharmaceutical companies have produced a drug to influence the remodeling rates.
In the postmenopausal years, important changes in the remodeling cycle are mainly triggered by lack of estrogen hormones. Those changes may have a dramatic effects on bone material and architecture, thus leading to an increased probability for bone to fracture. Estrogen deficiency increases osteoclast recruitment, activation frequency of new remodeling sites and reduces osteoclast death, therefore prolonging the resorption phase [53]. When measured with bone remodeling markers, there is a wide range of turnover variation in menopause: from 20% to 150% increase [54, 55]. In terms of Ac.f. (in transiliac biopsy), remodeling doubles already one year after the menopause, triples 13 years later and remains elevated in osteoporosis [56]. During menopause, the osteoblasts are not able to follow the increased activity of the osteoclasts, therefore each resorption pit is refilled with less bone than it was resorbed, thus leading to a global bone volume loss. Also postmenopausal rates of bone loss are not well defined and vary widely across the population. An indicative value may be a bone

loss of 0.85% per year [57].
The increased bone fragility which characterizes osteoporotic bone can be reduced when antiresorptive treatments using bisphosphonates are given, as indicated by various clinical studies [58, 53]. Bisphosphonates is a class of drugs that inhibits the resorption of bone. Bisphosphonates molecules are negatively charged and therefore they have a high tendency to bind with calcium ions (Ca^{2+}). In the acidic environment generated by the osteoclasts to resorb bone, the negative charge of bisphosphonates is neutralized, the molecules therefore detach from bone surface and can enter in the osteoclasts. Among various bisphosphonates, the nitrogen-containing drug inhibits an enzyme for the production of cholesterol which results in compromised capacity of the osteoclasts to attach to the mineralized matrix and in the reduction of the osteoclasts life span [59].
Different bisphosphonates result in different amount of turnover reduction. For example using risedronate (a bisphosphonate medication which will be investigated with our model in more detail) the turnover marker shows a rapid and significant reduction of 54.2% already after 3 months [60]. Measurements with standard bone histomorphometrical parameters agree with this value: Ac.f and BFR/BV give roughly a 50% reduction for the risedronate treated patients after 3 years of treatment [61, 51].

2.5 Bone mineralization

The end product of the remodeling process is new unmineralized bone matrix which has replaced old mineralized bone. The subsequent step is the mineralization of the organic matrix. Macroscopically the mineralization of the bone matrix has been qualitatively described as a two step process [62, 13]. A rapid increase in the mineral content within the first weeks after osteoblast deposition, called primary mineralization, is then followed by a slower augmentation of the mineral component lasting for several years and referred to as secondary mineralization. The amount of mineral deposited during the primary mineralization is roughly 70% of the full mineralization capacity and the remaining 30% is slowly added during the secondary mineralization. Experimental information on the mineralization kinetics can be obtained with a labeling procedure [37]. Fluorescent compounds like tetracycline which have high affinity for the small newly formed mineral crystals are given to a patient some days before a biopsy in order to have a bone sample where the tetracycline is incorporated. The information obtained with those methods, however, is only limited to the earlier stages of the mineralization process and an experimental method to measure the full mineralization kinetics is still missing. Here theoretical modeling can usefully complement the lack of experimental data. In this thesis a model is proposed to derive quantitative information on the mineralization process [47] (see section 3.2.1. From a more microscopic point of view, bone mineral is initially laid down at discrete sites in the collagenous matrix. First, the mineral particles grow very fast in two dimensions with a strong increase in the particles surface. This phase could probably correspond to the primary mineralization. Later on, during secondary mineralization, those thin and elongated crystals increase further in thickness [63, 20].
Currently a hot topic of research is to understand how the process of mineralization is controlled in living tissues [64, 14]. The underlying physical chemistry of crystal formation is basically the same, both for biological and geological crystals. However, the resulting crystals can be strikingly different. While geological crystals are macroscopic in size and faceted, biocrystals are typically nano-sized , have geometrically intricate shapes [65, 14] (being still a single crystal!) and occur in well defined spatial organizations. *In vitro* experiments demonstrated the importance of organic additives, depending on the concentration of the additives crystals can be formed in almost arbitrary shapes [66, 14].
In classical theory of crystal growth, nucleation occurs when aggregates of ions have sufficient energy to form a first stable nucleus. This is the most energy-demanding step of crystal formation and can occur when the free energy required to form new interfaces (which goes with the square of the size of the forming nucleus) is balanced by the free energy released in the formation of bonds in the bulk of the aggregates (which is proportional to the cube of the nucleus radius) [14]. Since the initial sites

for mineralization are probably the hole zones between collagen fibrils, collagen was thought to act like an apatite nucleator [67]. The same type of collagen, however, is also present in other tissues that normally do not mineralize, thus suggesting that collagen alone could not explain the nucleation of mineral crystals. There are at least three other factors which play a key role in the mineralization process: increased local ion concentrations, removal of nucleation inhibitors (like osteopontin [68] or fetuin A [69]) and direct exposure of nucleators [70]. The picture is in fact quite complex since most of the macromolecules of the bone matrix can act both as apatite nucleators as well as apatite growth inhibitors, also as a function of their concentrations [70].
After the nucleation, crystals start to grow by addition of ions and ion clusters to the newly formed stable nucleus. Crystal growth requires less energy than nucleation since, after a critical size, the nucleation barrier is already passed. In addition, during crystal growth, new nuclei may form on the surface of a growing crystal, a process called secondary nucleation, allowing the growth to speed up. The collagen matrix in which the mineral crystals are growing influences their shape and the size. This is evident for instance in osteogenesis imperfecta (OI) also called brittle bone disease [71]. In OI a defect in the genetic code results in slightly different assembly of the bone collagen, which in turn, alters the mineral size, shape and composition [72, 70].

2.6 Bone mineralization density distribution (BMDD)

Due to bone renewal, which comprises two distinct biological processes (remodeling and mineralization), the mineral content in bone is not uniformly distributed. Trabecular bone thus appears like a patchwork of different bone packets each of them having different age and therefore different mineral content (Fig. 2.5A). The different degrees of mineralization in different areas of bone can be measured experimentally. The result of these measurements can be summarized by a frequency distribution of the mineral content, called the bone mineralization density distribution (BMDD). In the BMDD diagram (Fig. 2.5B), the x-axis represents the calcium content and the y-axis the frequency at which a particular calcium content is present. This distribution for trabecular bone has usually a distinct asymmetric peak which can be characterized by three parameters. The most frequent calcium content, i.e., the position of the peak, is denoted by Ca_{Peak}, the full width at half maximum is called Ca_{Width}, and the mean calcium content, Ca_{mean}, is defined as the first moment of the BMDD.

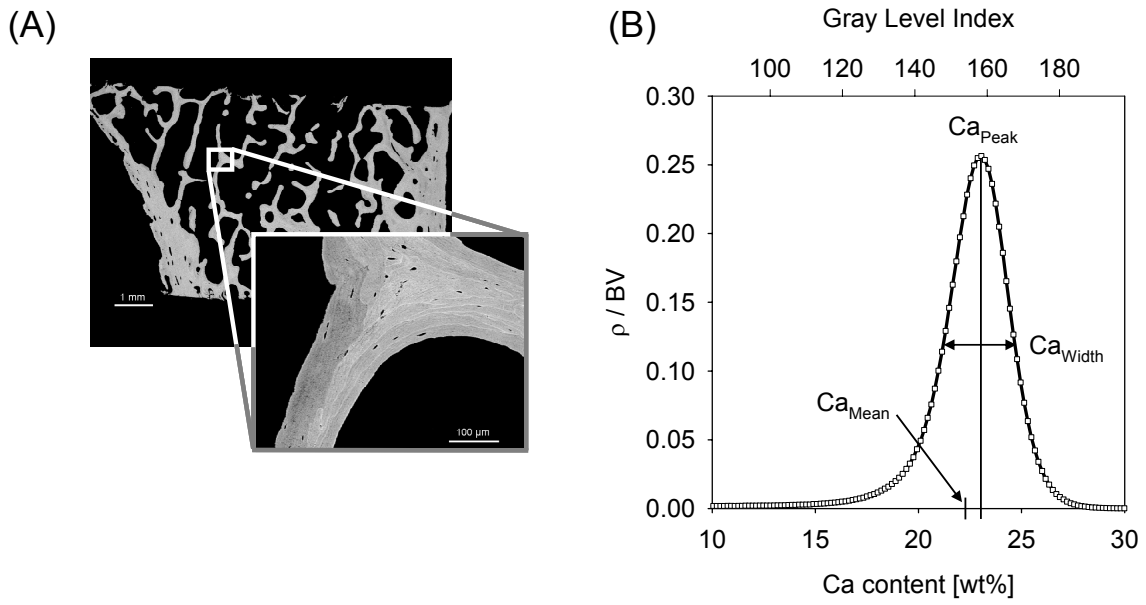

Figure 2.5: (A) backscattered electron image of transiliac bone biopsy (healthy female), the soft tissue or embedding medium is in black while the mineralized bone tissue is in gray. By zooming in, individual bone packets of different degree of mineralization can be seen. (B) corresponding peak-shaped BMDD distribution with the definition of three BMDD parameters: the most frequent calcium content (Ca_{Peak}), mean calcium content (Ca_{Mean}) and the full-width at half maximum (Ca_{Width}).

Despite their similar names, the bone mineralization density distribution (BMDD) and the bone mineral density (BMD) are quite different quantities. BMD is a single scalar value that reflects the mineral content in a given portion of bone which, in turn, depends on both, the total bone volume and the mean mineral content of the bone matrix [73, 74]. In contrast, the BMDD is not a simple number but a probability distribution which describes local differences in mineral content at the micrometer level.

2.6.1 How to measure the BMDD

Differences in mineral content within trabecular bone can be measured experimentally with three different techniques: quantitative microradiography (qMR) [62], quantitative backscattered electron imaging (qBEI) [73] and synchrotron radiation microtomography (SRμCT) [75]. They all are invasive techniques because of the requirement of bone biopsy. In qMR a bone section of 100 μm thickness is illuminated with an X-ray beam. The X-ray absorption is measured and the BMDD is derived from the contact microradiograph by analyzing the distribution of the X-ray attenuation in the different pixels. This method has a resolution of 40 μm and due to the relatively high sample thickness displays artifacts that come from projection effect errors [76]. SRμCT is based on the absorption of a monochromatic X-ray radiation from a synchrotron source by 3-dimensional bone samples. The monochromatic radiation allows the conversion of the gray level intensities (X-ray attenuation coefficients) in local mineral concentration. SRμCT is a quite powerful 3-dimensional measuring technique with a resolution of 4 μm per voxel. In addition to the BMDD, SRμCT gives access to the trabecular architecture. An example of a SRμCT image is given in Fig. 2.6 which shows a 3-dimensional mineralization distribution in an iliac crest biopsy: darker areas represent bone with low mineralization and younger age and in the brighter zones bone is older and more highly mineralized. In qBEI a bone specimen is irradiated with an electron beam and the amount of electrons that are back scattered from a thin surface layer of about 0.5 μm is detected. The probability of backscatter increases with the atomic number Z of the atoms interacting with the electron beam [78]. In bone tissue the element with the highest atomic number is calcium (Z=20) and therefore qBEI gives access to the local calcium content. The word *quantitative* indicates that a calibration needs to be performed in order to correlate the atomic number of the atoms in the sample and the back scattered signal in terms of its gray level. Carbon and aluminium are normally the reference materials used in the calibration. In addition, gray levels need to be translated into calcium concentration measured in weight%. This is done by considering as reference points the gray level to osteoid (unmineralized bone matrix) which is taken as 0 wt% Ca and the gray level of pure hydroxylapatite (HA) with 39.86 wt% Ca [73].

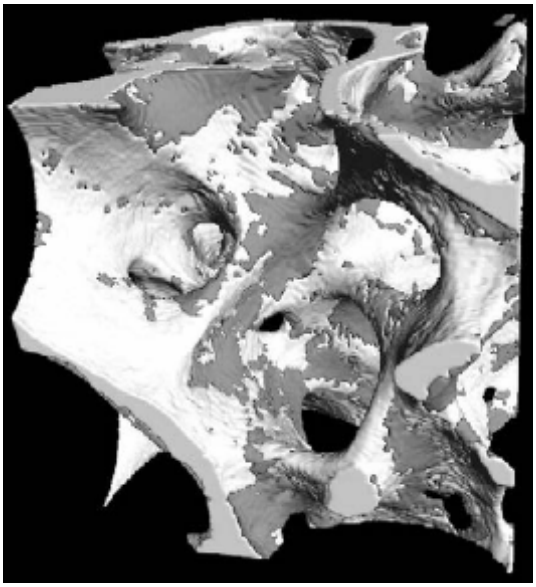

Figure 2.6: A gray-scale image in 3D of a 8.6 mm^3 volume of an iliac crest biopsy showing the spatial distribution of low-mineralized bone (dark areas) and high-mineralized bone (bright areas) in trabecular bone [77].

2.6.2 BMDD of healthy adults

Since the mean mineral content and homogeneity of mineralization are recognized as key points for the material quality of bone [13], it is important to establish whether or not the mineralization distribution is a characteristic conserved pattern for healthy people. Roschger et al. [79] investigated how the shape of the BMDD is influenced by ethnicity (African-American vs. Caucasian), skeletal site (ilium, vertebral body, patella, femoral neck and femoral head), gender and age (25 to 95 years). The main finding was the lack of a statistically significant influence of these biological variables on the BMDD [79]. The authors defined a reference BMDD for trabecular bone of healthy adults which can be used to detect changes in case of bone diseases or after bone treatments. The BMDD is therefore an important diagnostic tool to detect abnormal mineralization distributions that could contribute to reduce the mechanical competence of trabecular bone.
The reference BMDD of trabecular bone obtained in [79] is bell-shaped, presents a peak at about 23 wt% Ca content and is slightly asymmetric favoring lower mineral content (blue line in Fig. 2.7). To demonstrate how strong the BMDD can change due to bone diseases, in Fig. 2.7 the reference BMDD is compared with a BMDD from

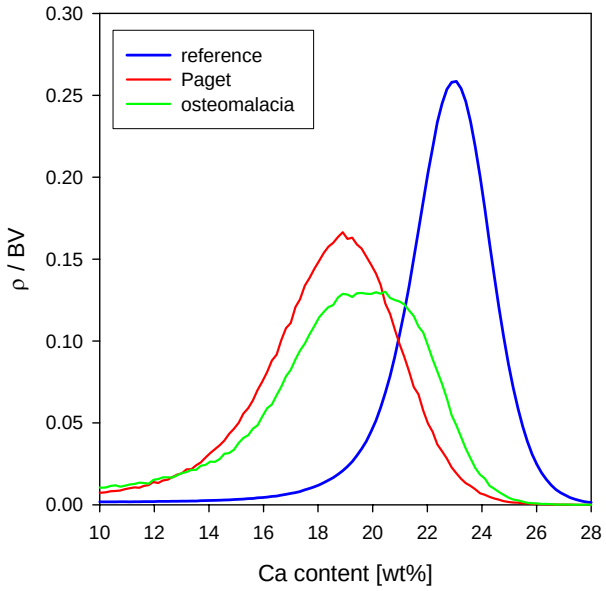

Figure 2.7: Reference BMDD (blue) compared with the BMDD from a patient with Paget's disease (red) and osteomalacia (green) caused by the celiac disease.

a patient with Paget's disease and osteomalacia (red and green line, respectively). Paget's disease is a disorder of bone remodeling which can affect isolated bones in the skeleton. In the diseased skeletal site, bone is softer and weaker than normal. Paget's disease is characterized by high bone turnover. Early in the course of the disease, old bone starts breaking down faster than new bone can be built. Over time, this is compensated by a subsequent increase in bone formation [37]. Osteomalacia, instead, is caused by a disorder in the mineralization process. In this disease bone normally has the right collagen structure but is lacking calcium, and therefore the osteoid (newly deposited unmineralized bone) fails to mineralize [37]. The corresponding BMDD is characterized by a mean mineral content, Ca_{Mean}, that is 20% less than in the reference BMDD.

2.6.3 BMDD in osteoporosis and antiresorptive treatments

Two very important scenarios, which will be also investigated with our mathematical model, are the wide spread cases of osteoporosis and the subsequent antiresorptive therapies. Since the changes in the mechanical performance cannot be explained in terms of simple bone mass, other influencing factors like the BMDD have been investigated. Recent results by Zoeher et al. [46] focus on the effect of osteoporosis and long-term treatment with risedronate on the mineralization pattern. The study

is based on the analysis of iliac crest bone biopsies at three different time points. The first biopsy was taken at baseline, i.e., in the osteoporotic condition and before giving medications. The second biopsy came from the opposite iliac crest, after three years of treatment. The last biopsy was removed after five years, from the same iliac crest as the baseline biopsy but far enough from the first site to avoid a bias of the mineralization distribution by bone healing processes. For each time point biopsies from at least 8 different patients were available and the corresponding BMDDs were generated with qBEI as described in section 2.6.1. Here, the BMDD data collected in [46] are averaged to obtain for each time point a representative BMDD.

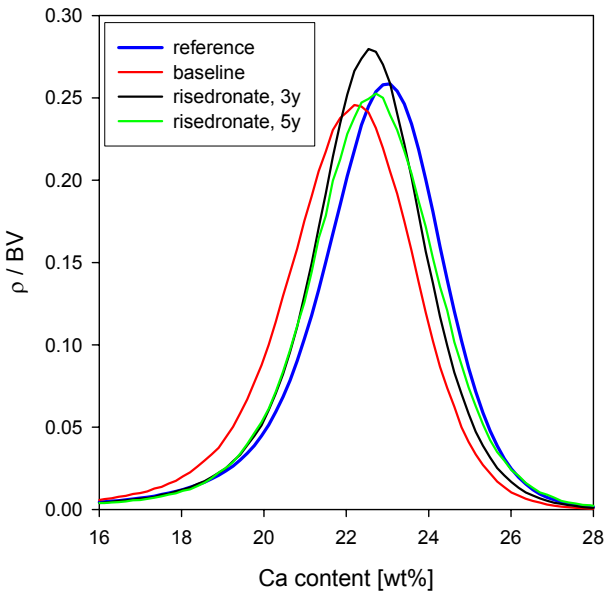

Figure 2.8: Reference BMDD (blue) and osteoporotic BMDD (red) along with the modification of the mineralization distribution after 3 (black) and 5 (green) years of treatment with risedronate. BMDDs are obtained by averaging the data reported in [46].

At baseline the osteoporotic BMDD (red line, Fig. 2.8) displays a lower degree of mineralization (low values of Ca_{Peak} and Ca_{Mean}), but a larger heterogeneity (high value of Ca_{Width}). This state, which reflects more newly formed bone matrix with a lower degree of mineralization, is consistent with the higher bone turnover of the osteoporotic patients (see section 2.4.2). After 3 years of treatment with risedronate (black line in Fig. 2.8) the peak of the distribution shifts to the right and gets narrower. While the shifting can be understood as a result of reduced turnover due to risedronate so that the bone packets have more time to mineralize, the narrowing is surprising. At the end of the treatments, at 5 years, the mean value, Ca_{Mean},

remains bigger than at baseline, Ca_{Peak} moves only slightly with respect to the 3-years position and the heterogeneity of the mineralization decreased compared to the 3-years time point (Fig. 2.8, green). In short, the behavior of Ca_{Mean} and Ca_{Peak} can be understood quite intuitively in term of different turnover rates, whereas the complex time evolution of the BMDD (also reflected in part by Ca_{Width}) requires more insights.
In the next chapter we present a mathematical model which allows the prediction of the time evolution of the mineralization distribution for different turnover situations, which will help to explain the experimental findings presented here.

Chapter 3

Mathematical model for the BMDD

In the previous chapter we have seen that the non uniform mineralization in bone can be described by a characteristic peak-shaped frequency distribution of the mineral content, called the BMDD. The distribution is the result of two dynamical processes: the remodeling process where small bone packets are renewed, and a subsequent mineralization during which the mineral content in the initially unmineralized bone packets increases. For healthy adults, the BMDD is virtually constant independent of biological parameters like sex, ethnicity, skeletal site and age [79]. Motivated by these experimental findings, we have developed a mathematical model to describe how remodeling and mineralization affect the shape of the BMDD.
The main purpose of our modeling will be:

- to investigate the steady state configuration of the BMDD to extract information on the underlining mineralization kinetics,
- to compute how different mineralization laws could give rise to different mineralization distributions and
- to simulate transient and steady-state configurations of the BMDD for different turnover rates of remodeling.

3.1 Model description

This section introduces all the model parameters and outlines how the two processes of mineralization and remodeling can be described in mathematical terms. Information about each variable are summarized, for example its dependent or independent character, its physical meaning and its connection with experimentally measurable

quantities. This part can also serve as kind of glossary for the symbols or quantities used.

Time, t, and calcium content, c
Time, t, and calcium content, c, are the two independent variables of our model. The value of the calcium content, measured in weight percentage of bone tissue (wt% Ca), can vary between 0 - corresponding to unmineralized bone (osteoid) - and a maximum value, c_{max}, which can be estimated based on the available volume in the collagen matrix to be about 56 vol% [29], i.e., close to 30 wt%.

BMDD, ρ
The BMDD is described as a function, $\rho(c,t)$, of the two independent variables time and calcium content. For a given bone sample, $\rho(c,t)dc$ is the total bone volume having a calcium content between c and $c+dc$, at time t. The measured BMDD histogram is usually normalized in a way that it sums up to 100% since independent data on bone volume is usually not available [73]. In our model $\rho(c,t)$ is defined in such a way that integrating over the whole range of calcium concentrations yields the bone volume $BV(t)$

$$\int_0^{c_{max}} \rho(c,t)dc = BV(t). \tag{3.1.1}$$

Consequently the quantity $\rho(c,t)dc/BV(t)$ denotes the probability that an elementary bone volume has a mineral content between c and $c+dc$.

Mineralization

Mineralization law, m(t)
The mineralization process is described by a mineralization law, $m(t)$. This function denotes how the calcium content in a newly deposited bone packet changes as a function of time. Since the calcium content is here assumed only to increase during the mineralization process, the function $m(t)$ is strictly monotonous and can therefore be inverted. The inverse function, $m^{-1}(c)$, then describes the time t needed to reach a calcium content of c starting from unmineralized bone matrix. In our model we assume for simplicity that the functional dependence of the mineralization law does not change with time. This assumption is realistic for healthy adults but maybe be erroneous during growth and for specific bone diseases like osteomalacia (see Fig. 2.7).

Mineralization velocity, v(c)
Closely connected with the mineralization law is the mineralization velocity, $v(c)$,

obtained from the time derivative of the mineralization law

$$v(c) \equiv \frac{dm}{dt}\left(m^{-1}(c)\right). \tag{3.1.2}$$

The mineralization velocity is therefore the slope of the mineralization law. The hypothesis of fast (primary) and slow (secondary) mineralization regimes corresponds to a non-constant velocity for different values of c. That $v(c)$ does not explicitly depend on time reflects the assumption of a fixed mineralization law. In addition, the constraint $v(c) > 0$ is a result of $m(t)$ being strictly monotonous.

Remodeling

Bone resorption - osteoclast action, ω_{OC}
Osteoclast action is described by a quantity which gives the probability of bone resorption. In principle, this resorption probability can depend on the calcium content. It was argued that osteoclasts could resorb preferentially mechanically damaged bone [44], which should be on average older and therefore higher mineralized. Likewise it can be argued that osteoclasts resorb preferentially younger, less mineralized bone, since they are more likely to encounter younger bone at the bone/marrow interface. To take into account this possible preference of resorption, the bone resorption preference rate, $\omega_{OC}(c,t)$, depends on both time and mineral content. $\omega_{OC}(c,t)\,\rho(c,t)\,dc\,dt$ gives the bone volume fraction with a calcium content between c and $c+dc$ which is removed between the time t and $t+dt$. $\omega_{OC}(c,t)$ can be connected to a parameter which is experimentally accessible with standard bone histomorphometry. The bone resorption rate, BRs.R/BV, defines the percentage of bone volume resorbed per year. The connection between ω_{OC} and BRs.R/BV is therefore established by (time, t, measured in years)

$$\frac{BRs.R}{BV}(t) = \int_{t-1}^{t}\int_{0}^{c_{max}} \frac{\omega_{OC}(c,t')\,\rho(c,t')\,dc}{BV(t')}\,dt'. \tag{3.1.3}$$

Bone deposition - osteoblast action, j_{OB}
The osteoblast activity, j_{OB}, can change during life time and is therefore in general time dependent. For instance in high turnover osteoporosis both deposition and resorption increase [56]. The osteoblast action in our model is mathematically described by a time dependent function, $j_{OB}(t)$. Again the model quantity, $j_{OB}(t)$, can be connected to a measurable quantity of bone histomorphometry, the bone formation rate, BFs.R/BV, by

$$\frac{BFs.R}{BV}(t) = \int_{t-1}^{t} \frac{j_{OB}(t')}{BV(t')}\,dt'. \tag{3.1.4}$$

Bone volume, BV(t)
The bone volume, $BV(t)$, can be derived from the deposition and resorption rate of the bone cells and is therefore not an independent parameter. Changes in bone volume occur due to an imbalance between the amount of bone resorbed by osteoclasts and the amount of bone deposited by osteoblasts during the remodeling process. The time evolution of the bone volume is therefore described by the following differential equation

$$\frac{dBV}{dt} = j_{OB}(t) - \int_0^{c_{max}} \omega_{OC}(c,t)\,\rho(c,t)\,dc. \tag{3.1.5}$$

3.1.1 The evolution equation of the BMDD

Before the rigorous mathematical description, an intuitive cartoon is presented which describes how mineralization and remodeling, when considered alone, may influence the mineralization distribution described by the BMDD. The starting point is a trabecula having a given mineralization distribution in terms of different bone packets with different mineral contents (different gray levels in Fig. 3.1A). For the case in which only mineralization occurs (Fig. 3.1B), the mineral content in each bone packet will increase with time according to the same mineralization law. The increase in mineral content is reflected by a shift of the BMDD to the right, towards higher mineralization values (Fig. 3.1C). The effect of an exclusive remodeling process can be depicted in the same way. Bone resorption, presented by resorption pits in (Fig. 3.1E) lowers the BMDD. The new unmineralized material laid down by the osteoblasts to refill the resorption pits is symbolized by a black bar at the very left of the BMDD diagram (Fig. 3.1F). In summary, the changes of the BMDD due to the mineralization can be seen as a flow from low to high values of the mineral content with an unchanged area under the curve corresponding to a constant bone volume. The effect of remodeling on the BMDD is that while flowing to the right towards higher c values, bone volume is lost due to some leakage to the flow (osteoclast action). Additionally the flow is fed from the very left (osteoblast action). Such flow problems can be mathematically described by a balance law which can be written schematically in the form

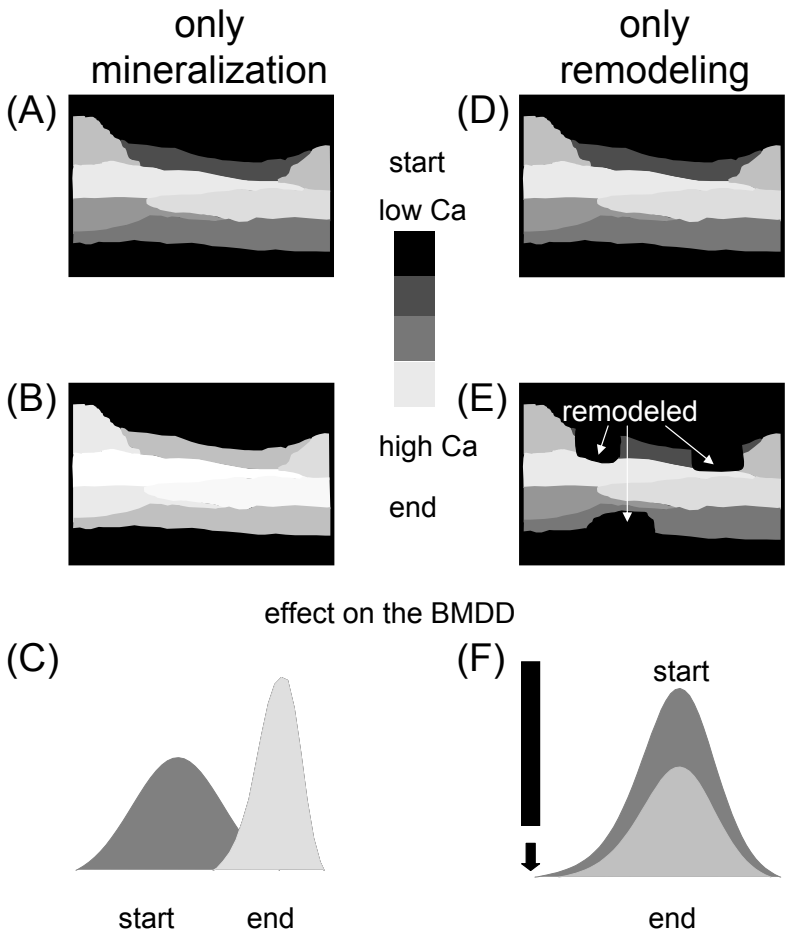

Figure 3.1: Sketch of the effect of mineralization and remodeling on the BMDD. Figures A, B and C illustrate how the mineralization process influences the mineralization distribution at the trabecular level. Due to the mineralization law the mineral content in each bone packet increases with time and the corresponding BMDD shift towards higher mineralization values. Figures D, E and F sketch the influence of the remodeling process: the osteoclasts simply lower down the BMDD whereas the osteoblasts add in new unmineralized material at the very left of the BMDD diagram (black bar). This is not seen in the BMDD curve if the osteoid does not mineralized.

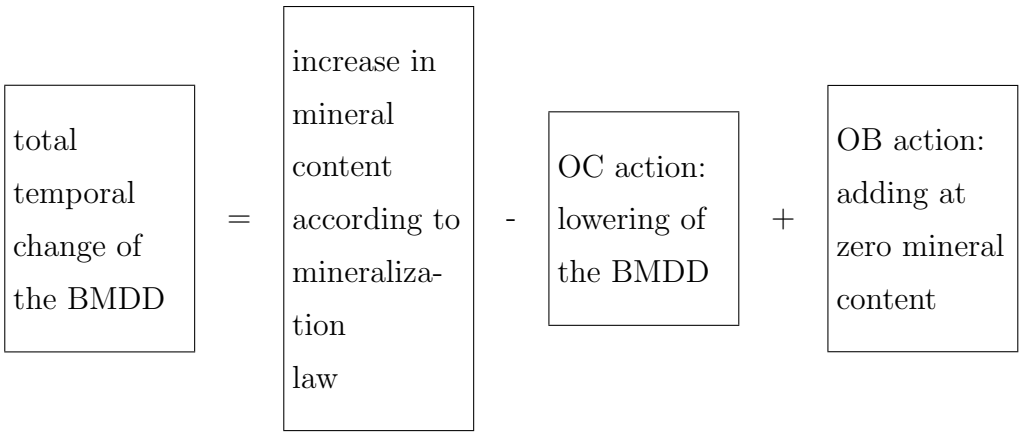

Based on these ideas, the evolution equation of the BMDD can be derived. Since this derivation is presented in detail in the appendix A of [47], only the final result is presented here. Note that for clarity reasons, in the thesis the notation of the mineralization law has been changed to $m(t)$.
The BMDD, ρ, evolves according to the following first order partial differential equation (PDE)

$$\frac{\partial \rho}{\partial t}(c,t) = -\frac{\partial}{\partial c}\left[\rho(c,t)\, v(c)\right] - \omega_{OC}(c,t)\, \rho(c,t)\,, \tag{3.1.6}$$

with the boundary condition at $c = 0$

$$\rho(c=0,t)\, v(c=0) = j_{OB}(t). \tag{3.1.7}$$

Equation 3.1.6 can be solved (numerically) once the cell action functions (i.e., $\omega_{OC}(c,t)$ and $j_{OB}(t)$), and the mineralization law $m(t)$ - and therefore the mineralization velocity $v(c)$ - are specified. For simple assumptions on the form of the $\omega_{OC}(c,t)$, $j_{OB}(t)$ and $v(c)$, equation 3.1.6 can be even solved analytically. Before describing an analytical solution (section 3.1.3) and a high resolution numerical method (section 3.1.4), the steady-state solution of equation 3.1.6 is discussed in the next section. The analysis of this type of solution is strongly motivated by the important experimental evidence that for healthy adults the BMDD is almost constant, independent of sex, ethnicity, skeletal site and age [79]. In the framework of our model this experimental observation means that in healthy adult humans a balance between bone remodeling and mineralization should maintain the reference BMDD unchanged.

3.1.2 Steady state solution

Under the assumption of steady-state, $\rho(c,t)$ and $\omega_{OC}(c,t)$ become functions only of the mineral content, i.e., $\rho(c)$ and $\omega_{OC}(c)$. Equation 3.1.6 and its boundary condition

3.1.7, become also time independent and simplify to

$$\begin{cases} \frac{d}{dc}\left[\rho(c,t)\, v(c)\right] = -\omega_{OC}(c)\, \rho(c) \\ \rho(c=0)\, v(c=0) = j_{OB} \end{cases} . \tag{3.1.8}$$

This ordinary differential equation can be solved analytically. The solution can be found in the appendix B of [47]. Here only the most important results are presented which can always be expressed in the form of two transformations. Either for a known mineralization law the BMDD is calculated or, vice versa, for a known BMDD the mineralization law is expressed.
The general solution for the mineralization law, expressed as $m^{-1}(c)$, is given by

$$m^{-1}(c) = \int_0^c \frac{\rho(c')\, dc'}{\int_{c'}^{c_{max}} \omega_{OC}(c'')\, \rho(c'')\, dc''}. \tag{3.1.9}$$

The inverse transformation reads

$$\rho(c) = j_{OB} \frac{m^{-1}(c)}{dc}\, exp\left(-\omega_{OC}(c) m^{-1}(c)\right) exp\left(\int_0^c \frac{d\omega_{OC}(c')}{dc'} m^{-1}(c') dc'\right) . \tag{3.1.10}$$

Under the assumption that the osteoclasts remove bone independent of its mineral content, i.e., $\omega_{OC}(c) = \bar{\omega}_{OC}$, Eq. 3.1.5 simplifies to $j_{OB} = BV\, \bar{\omega}_{OC}$. Furthermore as a consequence of the loss of the time dependence, the time unit can be chosen freely. The BMDD remains unchanged, for instance, in the case where both mineralization and remodeling are sped up by the same factor. Introducing a dimensionless time τ defined as t/t_{TO}, where t_{TO} is the turnover time, the transformations can be written in a more compact form

$$\frac{\rho(c)}{BV} = -\frac{d}{dc}\left[exp\left(-\tau(c)\right)\right] \tag{3.1.11}$$

and

$$\tau(c) = -ln \int_c^{c_{max}} \frac{\rho(c')}{BV} dc' . \tag{3.1.12}$$

3.1.3 Analytical solution

The evolution equation 3.1.6, classified as a first order linear PDE, can be solved analytically with the method of the characteristics in special cases.
Such a special case is when an exponential mineralization law is assumed, i.e.,

$$m(t) = 1 - exp(-t/t_{MI}), \tag{3.1.13}$$

where t_{MI} denotes a time constant characterizing the mineralization kinetics and when the remodeling is assumed to be completely suppressed, leading to

$$\frac{\partial \rho}{\partial t}(c,t) = -\frac{\partial}{\partial c}\left[\rho(c,t)\, v(c)\right] . \tag{3.1.14}$$

The mineralization law in inverted form reads as

$$m^{-1}(c) = -t_{MI}\, ln(1-c). \tag{3.1.15}$$

The mineralization velocity $v(c)$, obtained by differentiating the mineralization law 3.1.13 with respect to time t and then inserting Eq. 3.1.15, is then simply a linear decreasing function of the mineral content (Fig. 3.2B)

$$v(c) = \frac{1}{t_{MI}}(1-c). \tag{3.1.16}$$

Eq. 3.1.14 simplifies to

$$\frac{\partial \rho}{\partial t} + \frac{1}{t_{MI}}(1-c)\frac{\partial \rho}{\partial x} = \frac{1}{t_{MI}}\rho\,, \tag{3.1.17}$$

along with some initial condition for the mineralization distribution $\rho(c, t=0) = \hat{\rho}(c)$. The method of characteristics can be now applied to find an analytical solution for Eq. 3.1.17. The idea behind this method is to look for particular lines, called characteristic lines or characteristics, along which the PDE simplifies to an ordinary differential equation (ODE). Performing a coordinate transformation from the c-t coordinate system to the new s-c_0 system, the characteristics equations have the following form

$$\begin{cases} \frac{dt}{ds} &= 1 \\ t(s=0) &= 0 \end{cases} \tag{3.1.18}$$

$$\begin{cases} \frac{dc}{ds} &= 1/t_{MI}\,(1-c) \\ c(s=0) &= c_0 \end{cases} \tag{3.1.19}$$

which gives

$$\begin{cases} t &= s \\ c_0 &= 1-(1-c)exp(s/t_{MI})\,. \end{cases} \tag{3.1.20}$$

The characteristic curves $c(t) = 1-(1-c_0)exp(t/t_{MI})$ are plotted in Fig. 3.2C for different values of c_0. When $c_0 = 0$ the resulting characteristic is exactly the mineralization law. The other characteristics describe also the increase in mineral content, now for bone packets which display already a mineral content c_0 at $t = 0$. In the new $s - c_0$ coordinate system, the PDE 3.1.17 simplifies to the ODE

$$\begin{cases} \frac{d\rho}{ds} &= 1/t_{MI}\rho \\ \rho(s=0) &= \hat{\rho}(c_0) \end{cases} \tag{3.1.21}$$

which can be easily solved with the result

$$\rho(s) = \hat{\rho}(c_0) exp(s/t_{MI}). \tag{3.1.22}$$

Inserting now the expression for c_0 and s in Eq. 3.1.22 we obtain the analytical solution of the evolution equation in terms of the mineral content c and time t

$$\rho(c,t) = \hat{\rho}\left(1 - (1-c) exp(t/t_{MI})\right) exp(t/t_{MI})\,. \tag{3.1.23}$$

Assuming that the initial condition $\hat{\rho}(c)$ is a Gaussian function, Fig. 3.2D describes the time evolution due to the mineralization process. As time proceeds, the BMDD moves to the right and gets narrower as a result of a decreasing mineralization velocity. This simple result obtains specific significance when contrasted to the numerical solution in the case when bone remodeling is only partly suppressed (see section 3.10).

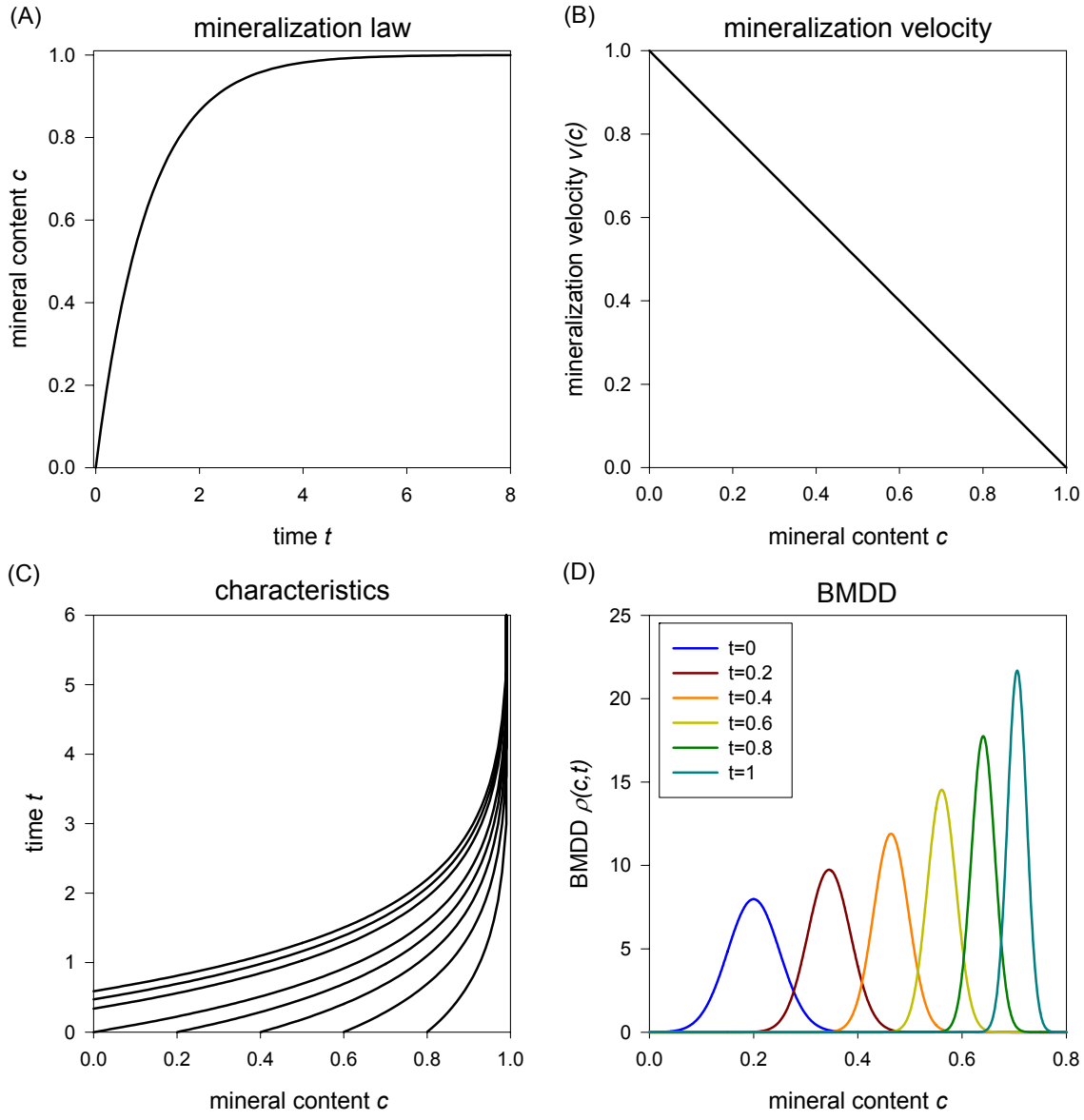

Figure 3.2: (A) a simple exponential mineralization law characterized by a single time constant. (B) the corresponding mineralization velocity is a linear decreasing function of the mineral content. (C) the characteristic curves which describe the increase in the mineral content in bone packets having an initial mineral content c_0. (D) the time evolution of the BMDD corresponds to a shift to the right and a narrowing of the peak.

3.1.4 Numerical solutions

In general situations where analytical solutions are not available, Eq. 3.1.6 needs to be solved with a suitable numerical method. Classical finite difference schemes fail to approximate the solution of such PDEs since they can give rise to non physical oscillations. High resolution finite volume methods [80] have been developed to overcome these limitations.

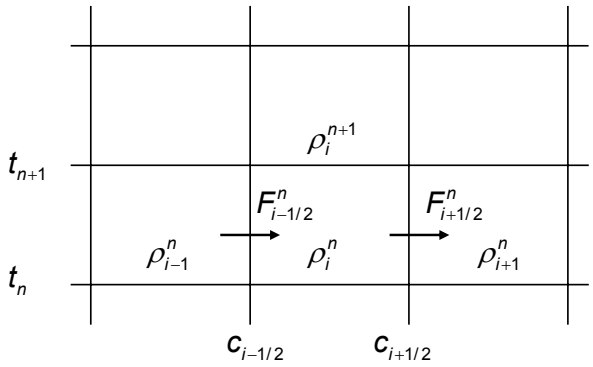

Figure 3.3: Illustration of a finite volume method for updating the cell average ρ_i^n by fluxes at the cell edges.

In finite volume methods, rather than point wise approximations at grid points as in finite difference methods, the integration domain is broken into intervals called finite volume or grid cells. The discrete variable, ρ_i^n, has the meaning of cell average of $\rho(c, t_n)$ over each grid cell in the interval from $c_{i-1/2}$ to $c_{i+1/2}$

$$\rho_i^n \equiv \frac{1}{\Delta c} \int_{c_{i-1/2}}^{c_{i+1/2}} \rho(c, t_n) dc \,. \tag{3.1.24}$$

The quantity ρ_i^n is modified in each time step by the flux through the edges of the grid cells, as sketched in Fig. 3.3. In the finite volume framework, an explicit time marching algorithm has the following general form

$$\rho_i^{n+1} = \rho_i^n - \frac{\Delta t}{\Delta c} \left(F_{i+1/2}^n - F_{i-1/2}^n \right) \tag{3.1.25}$$

where $F_{i-1/2}^n$ and $F_{i+1/2}^n$ are approximations to the average flux along $c = c_{i-1/2}$ and $c = c_{i+1/2}$, respectively. The primary problem in finite volume method is to determine good numerical flux functions (stable and accurate) based on the approximated cell averages ρ_{i-2}, ρ_{i-1}, ρ_i and ρ_{i+1}. In the high resolution finite volume methods, the flux at the boundary of each grid cell contains a combination of a low-order stable flux $F_L(\rho_{i-1}, \rho_i)$ and a higher-order accurate flux $F_H(\rho_{i-2}, \rho_{i-1}, \rho_i)$. This combination is

weighted by a so-called "flux limiter" which controls the local solution behavior and allows one to decide whether to use a more stable or a more accurate flux function. The key point is that to control the local behavior of the solution which, from the finite volume point of view, is described by its average value over each grid cells, one needs to make some assumptions on the form of the solution $\tilde{\rho}(c, t_n)$ inside each interval $(c_{i-1/2}, c_{i+1/2})$. A simple, but already very useful assumption, is to describing the solution inside the finite volume cells with a linear function

$$\tilde{\rho}(c, t_n) = \rho_i^n + \sigma_n^i \, (c - c_i) \tag{3.1.26}$$

where σ_n^i is the slope of the linear reconstructed function. The local behavior of the solution can now be controlled by a reasonable guess for σ_n^i including information of ρ_i^n of the nearest and next-nearest grid cells. Near strong variation of the solution between adjacent grids, the slope σ_n^i can be reduced in order to avoid oscillations.
Since also a source term is present in Eq. 3.1.6, we need to use a fractional-step or operator splitting method, where the idea behind is to split up the problem in two sub-problems that can be solved independently [80]:

$$\text{Problem A:} \quad \frac{\partial \rho}{\partial t}(c, t) + \frac{\partial}{\partial c}\left[\rho(c, t)\, v(c)\right] = 0 \tag{3.1.27}$$

$$\text{Problem B:} \quad \frac{\partial \rho}{\partial t}(c, t) = -\omega_{OC}(c, t)\, \rho(c, t) \tag{3.1.28}$$

For each of these two sub-problems we can use suitable numerical methods: for problem A we need a high resolution method of the type presented before, whereas problem B can be solved also analytically. The full implementation of the numerical method adopted is reported in appendix A.

3.2 Results and discussion

First the steady state relationship between the mineralization law and the BMDD, which is mathematically summarized in the transformations 3.1.11 and 3.1.12, is investigated. We start by showing how different mineralization laws influence the shape of the resulting steady-state BMDD. In the next step we solve the "inverse" problem, i.e., starting from the experimental data of the reference BMDD we derive the underling mineralization law for healthy humans. The last step of the steady state analysis is the assessment of the influence of turnover on the final form of the mineralization distribution. Since these results were already published in [47], the following two sections concentrate on the discussion of three key figures.
By solving Eq. 3.1.6 numerically, with the method presented in the previous section, the full time evolution of the BMDD as a function *i)* of a change in turnover and *ii)*

of the rate at which this change is applied, can be predicted. An extensive study of the influence of these two turnover variables on the transient configurations of the BMDD and on the BMDD parameters Ca_{Mean}, Ca_{Peak} and Ca_{Width} is performed. The computation results are compared with experimental data obtained from patients with high turnover osteoporosis and turnover reduction due to bisphosphonates treatments.

3.2.1 Effect of mineralization law

Due to experimental difficulties in determining the increase of the mineral content in a bone packet as a function of time, no mineralization law has been quantitatively proposed in the bone literature both for healthy humans and for patients with disorders in the mineralization process. To gain a better understanding of the effect of the mineralization law on the resulting shape of the BMDD, we chose simple, hypothetical mineralization laws (Fig. 3.4A) and then calculated the corresponding BMDDs (Fig. 3.4B) using Eq. 3.1.11. The hypothetical mineralization laws are an exponential function with a small time constant (fast mineralization), large time constant (slow mineralization), two exponentials and a double linear function. All equations are summarized in table 2 of [47].

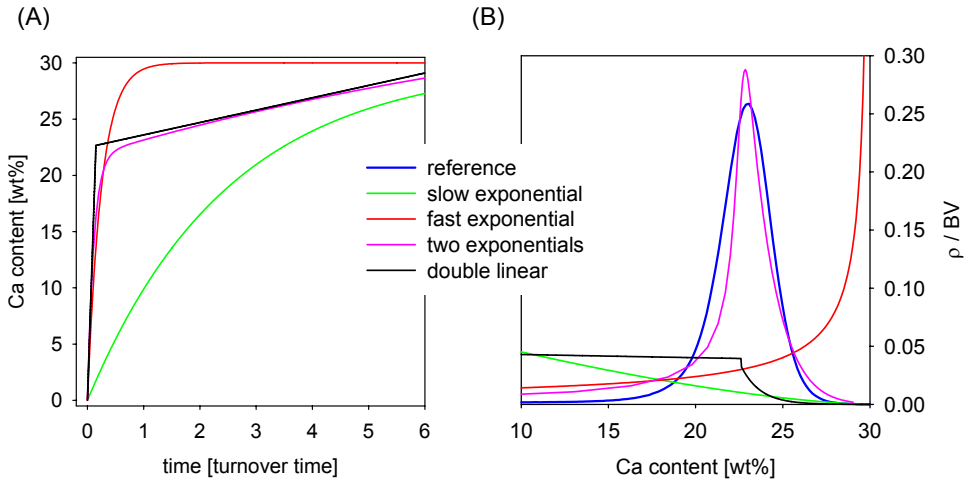

Figure 3.4: (A) different hypothetical functions to describe the mineralization law: exponential growth with one slow time constant ($\tau_{MI} = 5$) or one fast time constant ($\tau_{MI} = 0.25$), green and red line respectively; double linear function (black) and sum of two exponentials (pink) with two time constants ($\tau_1 = 9$ and $\tau_2 = 0.09$). (B) comparison between the reference BMDD (blue) and the simulated BMDDs considering the mineralization laws defined in (A).

The conclusion of this test of mineralization laws is that laws with a single time constant fail to reproduce the characteristic peak of the reference BMDD. Exponential mineral laws result in monotonous BMDDs (Fig 3.4B). Either mineralization is so fast that the mineral content in most of the bone packets come close to the maximum value before being remodeled (red curve in Fig. 3.4), or, in the case of slow remodeling, bone is remodeled while it is still almost unmineralized, therefore the BMDD decreases monotonously from c=0. A mineralization law which is consistent with the peak-shaped form of the reference BMDD is characterized by at least two time constants. In the first time regime, the mineralization process dominates, which leads to an increase in the amount of not yet fully mineralized bone. Conversely, when the mineralization process slows down significantly and drops behind the remodeling process, the amount of higher mineralized bone starts to decrease due to bone resorption causing a peak in the BMDD. Due to the mineralization process, the bone packets shift in the BMDD diagram from low to high mineral content. The slowing down of the mineralization velocity leads to a kind of "traffic jam" of the moving bone packets in the diagram, with the result that the different bone packets pile up giving rise to a peak in the BMDD. According to this picture, the more rapid the reduction in the mineralization velocity, the sharper becomes the peak of the BMDD.
Being interested in the mineralization law which results exactly in the reference BMDD, there is no need to proceed with guessing adequate mineralization laws. Instead Eq. 3.1.12 can be used which allows a back-transformation of the BMDD to the underlying mineralization law. Since Eq. 3.1.12 defines a nonlinear transformation, it is important to start from the raw data which were used to define the reference BMDD (see Fig. 3.5A). The input data were the BMDDs of 52 samples, both autopsies and biopsies, of healthy adult humans having different age, sex, ethnicity and skeletal site analyzed in reference [79]. Using Eq. 3.1.12 the mineralization law for each of the 52 BMDDs was calculated separately. The results were then averaged resulting in a mineralization law of healthy adult humans and its standard deviation describing the increase in the mineral content in a bone packet over several decades in time (Fig. 3.5B, note the logarithmic time scale of the insert). Since the input data is only numerical data, the resultant mineralization law is not an analytical mathematical function. However, a sum of two hyperbolic functions give a reasonable fit to the numerically calculated mineralization law. According to the obtained law, mineralization proceeds extremely fast (within days) up to a value of about 18 wt% Ca. After this initial mineralization surge, a smooth transition follows, which leads for later times to an approximately linear increase in the mineralization as a function of time. The slope in this regime is about three orders of magnitude smaller than for the initial part of the mineralization law. Assuming a turnover time of 5 years [51], the increase in the mineral content is predicted over decades.

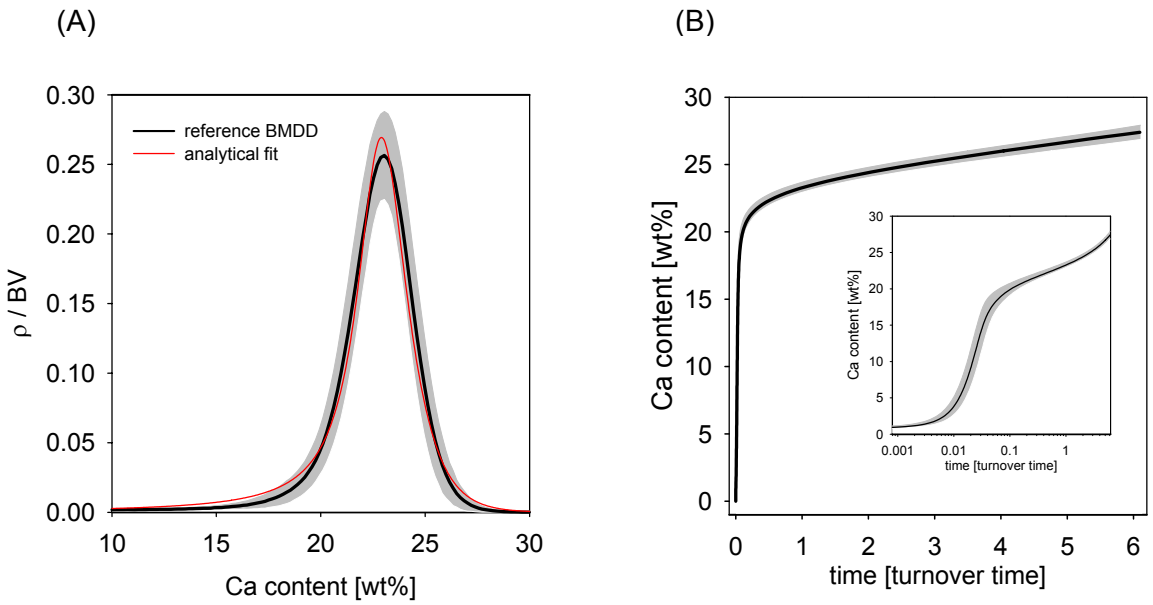

Figure 3.5: (A) measured reference BMDD: the black line shows the curve obtained averaging 52 BMDDs from healthy adult humans with the standard deviation boundaries (gray area). The red line denotes the analytical fitting using a sum of two hyperbolic functions for the mineralization law. (B) the corresponding calculated mineralization law: the black line shows the derived mineralization law together with its standard deviation. In a semi-logarithmic plot (insert) the biphasic nature of the mineralization law is evident.

3.2.2 Steady state effect of turnover rate

The mineralization law obtained for healthy humans (Fig. 3.5B) is used to investigate the effect of changes in the remodeling process on the final form of the BMDD. With the help of Eq. 3.1.11 the BMDD as a result of different values for the turnover rate can be predicted. The effect of a higher turnover rate is a shift of the peak to values of lower mineralization, while a reduced turnover results in a shift to the right (red and green line in Fig. 3.6A, respectively). The shift of the peak position is also reflected in the monotonously increasing function of Ca_{Peak} plotted in Fig. 3.6B.
While in the considered interval of the turnover time with respect to the healthy turnover time between 0.1 and 4, Ca_{Peak} increases only by a factor of 1.19, the mean Ca content, Ca_{Mean}, increases by a factor 1.56. This discrepancy of the behavior of Ca_{Peak} and Ca_{Mean} is due to the change in the shape of the BMDD as characterized by the width of the peak, Ca_{Width}, and its asymmetry.
The next section will show that the full time evolution of the BMDD is not a simple shift of the peak, but gives rise to interesting transient configurations.

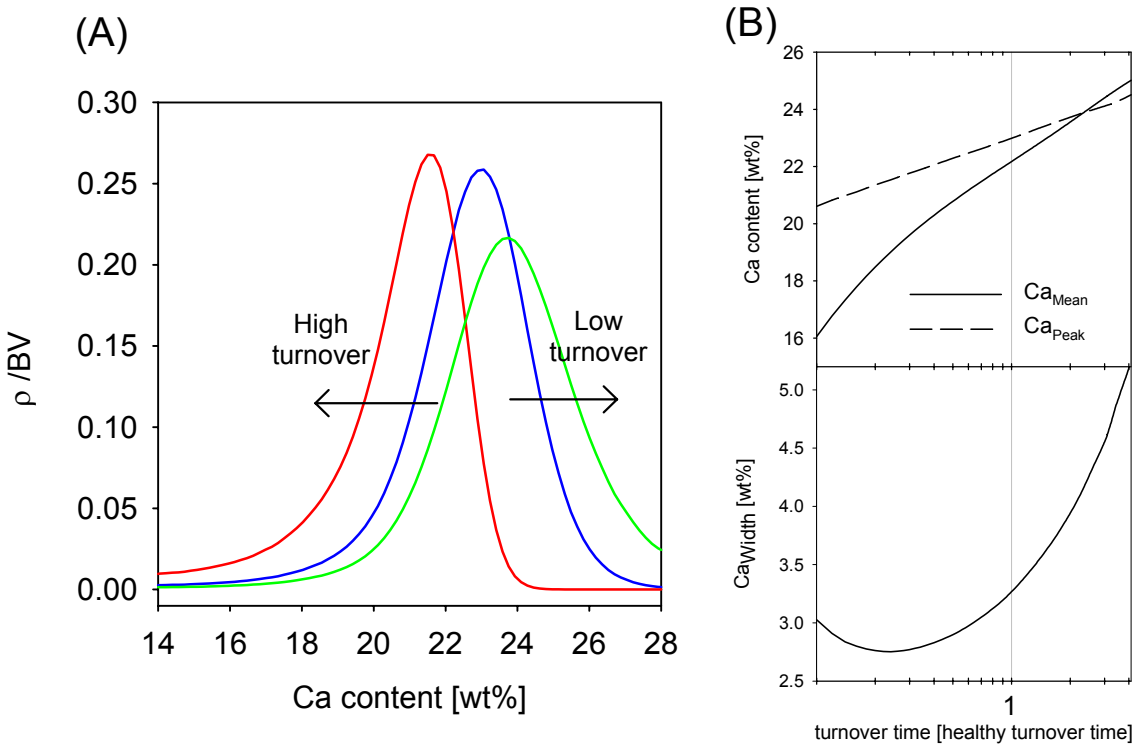

Figure 3.6: (A) effect of different turnover times keeping the same mineralization law of Fig. 3.5B: the blue line denotes the reference BMDD, the red line presents a high turnover situation (4 times increased turnover with respect to the normal turnover time) and the green line is the result of a 2 times reduced turnover. In both cases a constant bone volume and a steady state condition for BMDD is assumed. (B) most frequent calcium content (Ca_{Peak}), mean calcium content (Ca_{Mean}) and full-width at half maximum of the peak (Ca_{Width}) plotted against different turnover times. The turnover times are normalized by the healthy turnover time, which corresponds to the turnover of the reference BMDD (i.e., 0.1 refers to a 10 times increased turnover).

3.2.3 Time evolution of the mineralization distribution

For the dynamical simulations we also assume that the mineralization law does not change with time. Changes in the turnover after menopause or after administration of bisphosphonates are known to occur initially fast and then level off. We assume that this variation in turnover can be well described by an exponential function. In the model, changes in turnover are introduced via a varying osteoclast action

$$\omega_{OC}(t) = \omega_{OC-i} + (\omega_{OC-f} - \omega_{OC-i}) \left[1 - exp\left(-\frac{t}{t_{OC}}\right)\right], \qquad (3.2.1)$$

where ω_{OC-i} denotes the initial turnover rate, ω_{OC-f} the final one and t_{OC} describes the time constant of the change between these two values. When the osteoblast action, j_{OB}, follows the changed resorption with an equal law, the bone volume remains unchanged. Different time dependence for both types of bone cells lead otherwise to a change in bone volume according to Eq. 3.1.5.
In the following we study the effect of the magnitude of the variation in the turnover rate ($\omega_{OC-f}/\omega_{OC-i}$) and the effect of how fast the turnover rate is varied (t_{OC}) on the time evolution of the BMDD and on the three BMDD parameters Ca_{Mean}, Ca_{Peak} and Ca_{Width}. In particular two scenarios are investigated: *i)* the increase of the bone turnover due to hormonal changes after menopause and *ii)* a decrease in turnover as an example of antiresorptive treatment of an osteoporotic patient.

Increased turnover as a model for menopausal changes

The hormonal changes at the onset of menopause have an effect also on bone remodeling. Measurements of these effects (see also section 2.4.2) gave the following values which are also used as input data for our simulations. The bone remodeling rate in postmenopausal women was found to be between 1.2 and 5 times higher than in premenopausal women [54, 56]. Here simulations are reported where the turnover rate is assumed to be 1.25, 2.5 and 5 times increased in comparison to healthy premenopausal reference values (i.e., a turnover time of 5 years [51]). Since these changes in turnover have been reported to occur rather slowly [56, 81], time constants for turnover change (Eq. 3.2.1) of 1 and 5 years were chosen. Also a very short time constant, t_{TO}, of only 1 month was tested to see the influence of this parameter. To take into account the bone loss after menopause simulations have been performed with both a bone loss of 0.85% per year [57] and a constant bone volume. The bone volume reduction showed only very minor effects on the shape of the BMDD. The loss in bone volume is just reflected by a lowering of the curve, without affecting the characteristic shape.
Starting with the reference BMDD defined for healthy adults in [79], Fig. 3.7 shows the time evolution of the BMDD when the turnover rate is increased 2.5 times with a time constant of 1 year. As already shown in the analysis of the steady state solu-

tion of the evolution equation (section 3.2.2), the main difference between the initial BMDD and its "final" configuration for later times is a shift of the peak towards lower values of the mineral content. The time evolution of the BMDD, however, is far from being a smooth movement of the peak towards lower Ca values. At the beginning the initial peak at about 23 $wt\%Ca$ decreases in height due to increased osteoclast activity without changing its position. The concurrent increased osteoblast activity leads to enhanced bone deposition, whose mineral content increases quickly during primary mineralization. In the BMDD diagram this leads to the appearance of a second peak, which moves in from the left. For the parameters used in Fig. 3.7, after about 2 years the two peaks have approximately the same height, while after 3 years the old peak is vanished and is visible only as a shoulder in the new shifted main peak. After 5 years the new peak has grown to its final height, and with the exception of Ca values larger than approximately 23.5 $wt\%$ where small differences can be still observed, is indistinguishable with the equilibrium configuration.
The temporal change of bone turnover with the values chosen in the simulations, together with the time development of two key parameters characterizing the BMDD, Ca_{Peak} and Ca_{Mean}, are plotted in Fig. 3.8. Since Ca_{Peak} marks the position of the highest peak in the BMDD, the discontinuity in Fig. 3.8C corresponds to the distance in the time-axis between the old shrinking peak and the newly formed one. For larger changes in the turnover the new peak position is reached faster, also due to the fact that the new equilibrium positions for larger turnover changes are at smaller values of the Ca content.
The same holds for Ca_{Mean}, which decreases after change in turnover from an initial value, Ca_{Mean-i}, and attains a new reduced value, Ca_{Mean-f}. This decrease can be well described by an exponential decay similar to Eq. 3.2.1

$$Ca_{Mean}(t) = Ca_{Mean-i} + (Ca_{Mean-f} - Ca_{Mean-i}) \left[1 - exp\left(-\frac{t}{t_{Ca}}\right)\right], \qquad (3.2.2)$$

where t_{Ca} denotes the time constant of how fast the new reduced value of Ca_{Mean} is attained. Surprisingly, larger changes in the turnover are accommodated more quickly than smaller one, which is reflected in the corresponding values for t_{Ca}. For a 5 times reduction of the turnover t_{Ca} is 2 years, while a reduction of 2.5 times results in t_{Ca}=7 years. As expected, when the change in turnover occurs faster, then also the equilibration of the new peak position and of Ca_{Mean} occurs faster (see Fig. 3.8F).

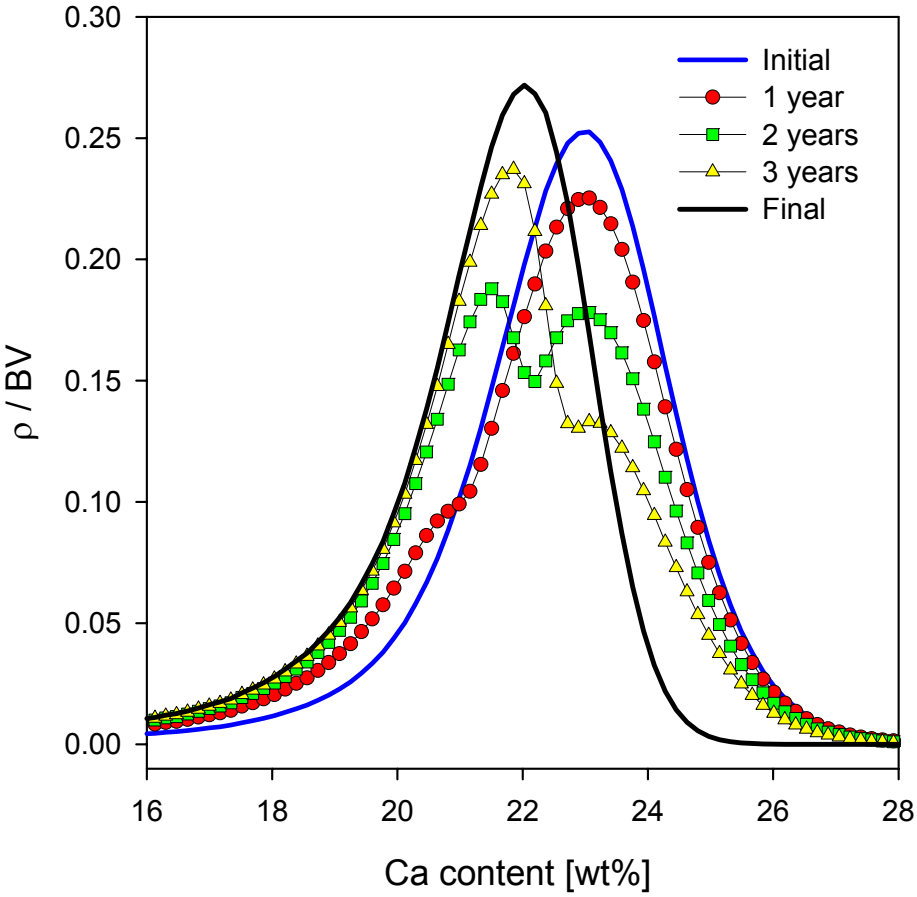

Figure 3.7: Simulated time evolution of the BMDD starting with the healthy reference BMDD (full blue line) and increasing the turnover by a factor of 2.5 exponentially with a time constant of 1 year. Mineralization distributions are given at 1, 2 and 3 years. At 5 years (not shown) the BMDD coincides with the new equilibrium configuration (black line) for Ca values below 23.5 wt%.

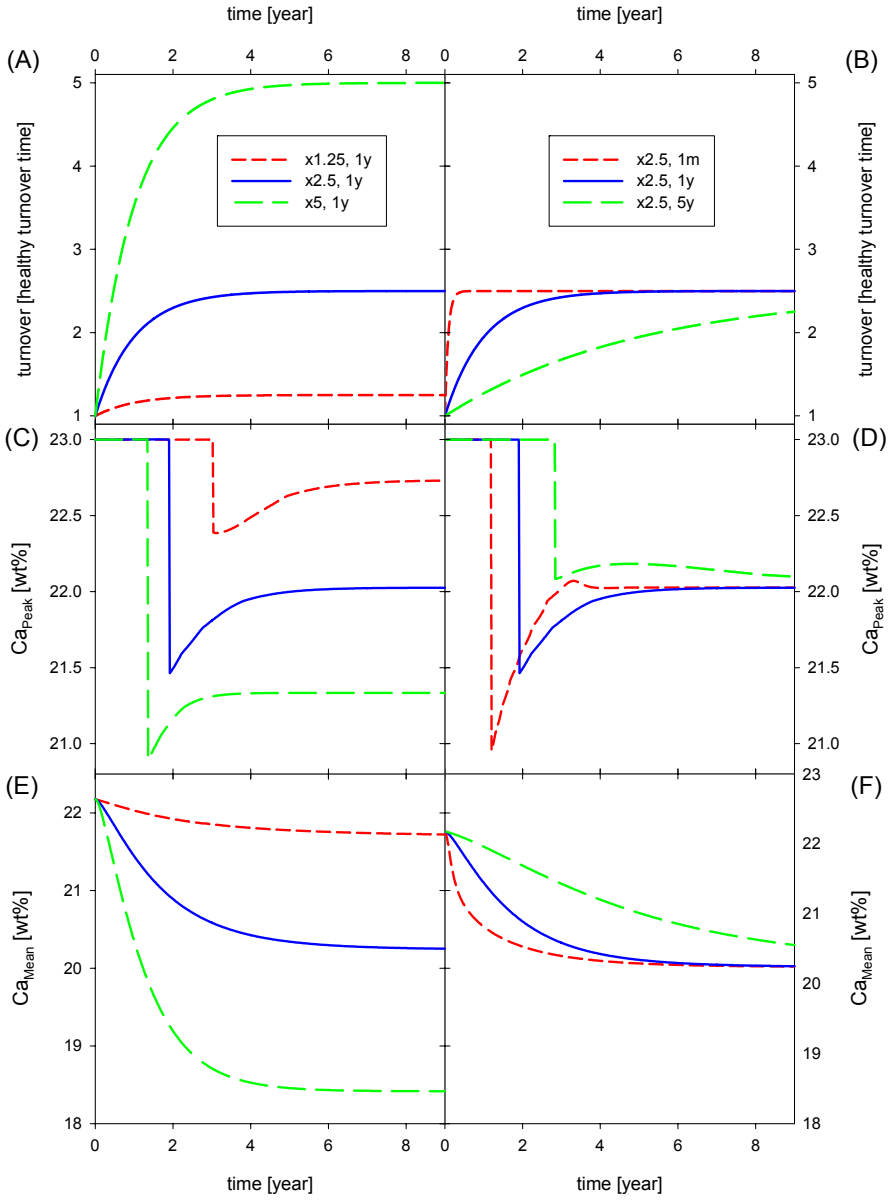

Figure 3.8: Time development turnover changes and of corresponding changes of Ca_{Peak} and Ca_{Mean}. Left, the turnover is changed by a factor of 1.5, 2.5, and 5 with the same time constant t_{OC} of 1 years. Right, the turnover is always increased 2.5 times, but with different velocities corresponding to time constants t_{OC}= 1 month, 1 and 5 years. The change in Ca_{Mean} can always be fitted by an exponentially decaying function like Eq. 3.2.2.

Reduced turnover as a model for antiresorptive treatments

Bisphosphonates are administered to osteoporotic patients to reduce bone turnover. In this work specifically the action of the bisphosphonate risedronate is simulated, since its effects are very well documented by clinical studies making use even of triple temporal biopsies of the same patient (see section 2.6.3 for more information about this study). Although the interindividual variability is high, the effect of risedronate on bone is a reduction of about 50% of the remodeling rate [51], which is substantial after 3 to 6 months after treatment initiation [60]. In the simulations, the initial condition was an average over 5 BMDDs from osteoporotic patients having participated in the study mentioned above. For this condition a turnover of 2.5 higher than the healthy turnover was assumed. Reported here are simulations with reduced turnover of 30, 50 and 60 % and with time constants of turnover reduction, t_{TO}, (reflecting the temporal efficacy of the drug) of 6 months, 1 year and 3 years. Fig.3.9 shows an example of the time evolution of the BMDD when the turnover rate is reduce from an initial rate 2.5 times higher than the healthy turnover to a final rate only 1.25 times higher than the healthy turnover, with a time constant of 6 months. The reduction of turnover results on the long term, after the system is re-equilibrated, in a new peak shifted to higher Ca content (peak marked as "final" in Fig. 3.9). Again the transient configurations of the BMDD are of interesting shape. The transient peak displays an unusual large height and small width. This behavior correspond to a strong homogeneity of the mineral content in bone. Furthermore it is remarkable that the position of the peak overshoots its final position, as can be seen after 5 years (Fig. 3.9), therefore performing a peculiar first-right-then-left movement.
How this behavior of the BMDD depends on the specific change in turnover is shown in Fig. 3.10. In the top row the different changes of the magnitude of turnover (left) and the velocity of turnover change (right) are plotted with time. Starting from its initial position at 22.2 wt% Ca, the peak moves to the right much further than its final position at about 22.8 wt% Ca. The overshooting of the peak is strongest, when the turnover reduction is large and occurs fast. Under exactly these circumstances, the peak width takes very small values. After some initial reductions, which are probably due to a non completely equilibrated initial condition, Ca_{Mean} increases again in an exponential way. Comparison with the measured BMDDs available at 3 and 5 years (triangle and square in Fig. 3.10, respectively) shows good agreement in the behavior of Ca_{Peak} and Ca_{Mean}. Also qualitatively the intermediate reduction of Ca_{Width} is reproduced, although in the simulations this effect is more pronounced. It is a general feature of our computational results, that simulated BMDDs tend to be narrower than the measured ones. The reason could be the biological variability between individuals and even for one individual biological factors like the diet can change during the long observation time. Such variabilities cannot be easily incorporated in the model.

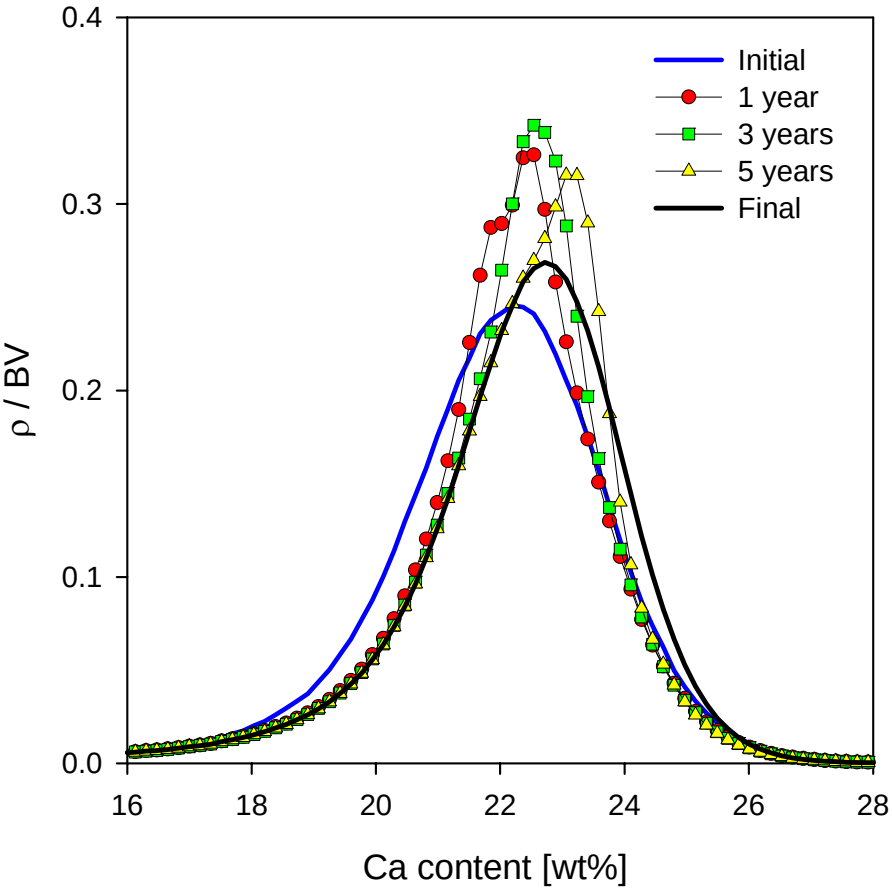

Figure 3.9: Simulated time evolution of the BMDD starting with a BMDD obtained by averaging over 5 BMDDs of osteoporotic women after menopause. It is assumed that the turnover at baseline is 2.5 times increased compared to normal and that the antiresorptive therapy slows down the turnover to half of its initial value with a time constant of 6 months. Mineralization distributions are plotted at 1, 3 and 5 years.

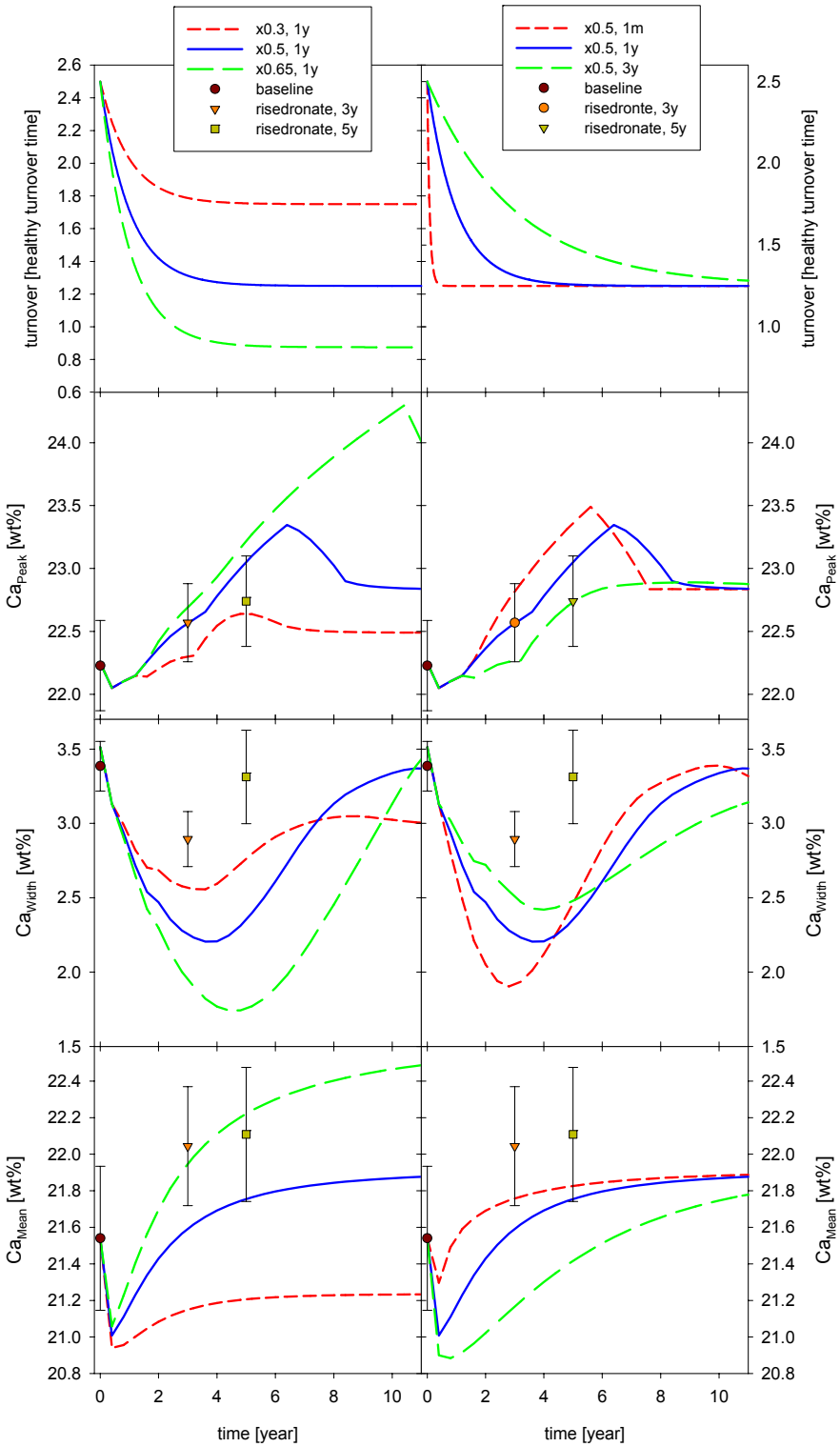

Figure 3.10: Time development of Ca_{Peak}, Ca_{Width} and Ca_{Mean}. Left, the turnover is reduced 30%, 50% and 65% with the same time constant t_{OC} of 6 months. Right, the turnover is always reduced 50%, but with different velocities corresponding to time constants t_{OC} = 1 month, 1 and 3 years.

3.3 Conclusions and outlook

The remodeling activities of bone cells together with the time course of mineralization of newly formed bone matrix generate a characteristic mineralization pattern that can be described by the BMDD. The dynamical evolution of the BMDD is strongly influenced by variations in the remodeling rates and interestingly by the sign of these variations. By this we mean that an increase in turnover causes a transient double peak, while a reduction leads transiently to a very pronounced BMDD peak. The proposed theoretical framework is independent of bone type and can therefore also be applied to cortical bone. However, the definition of a reference BMDD for healthy adults in cortical bone has not yet been obtained. This is not unexpected considering the poor equilibration of the BMDD in cortical bone due to its slow remodeling. Another application of our model would be to investigate the mineralization kinetics in animals. In bone research, animals like mice and dogs are often employed as models to understand bone and to perform clinical studies. The metabolic functions usually depend on animal size, being faster in smaller animals. Therefore it would be interesting to compare mineralization laws in different animals and ask whether they can be superimposed by appropriately rescaling time. In terms of bone material quality, this work can be seen only as a first step since the mechanical implication of changes in the BMDD still need to be assessed. It is known that highly mineralized bone tends to be stiffer but more brittle. However how the heterogeneity of the BMDD is reflected in the mechanical properties is difficult to predict. From a mechanical point of view the specific location of the bone packets of different mineral content has to be considered, an information completely disregarded by the BMDD. Analysis of single trabeculae indicated more mineralized bone packets are concentrate along the middle axis of the trabecula, whereas the surface is occupied predominately by less mineralized bone [82]. The standard physical tool to improve this deficiency of the BMDD is by introducing spatial correlation functions.

Chapter 4

Bone architectural quality

Trabecular bone is the spongy type of bone that can be found inside vertebral bodies or close to joints. Its network like architecture, like bone material, undergoes dynamical changes and evolves in time due to bone remodeling. When looking at trabecular structures, for example inside a human vertebra or inside a femoral head (Fig. 4.1), it is obvious that the trabecular arrangement is neither completely regular nor completely random. Even if the trabeculae seem to be placed where there is a mechanical need, a rigorous mathematical formulation of the "optimization" principle to explain the trabecular arrangement is still missing [83].

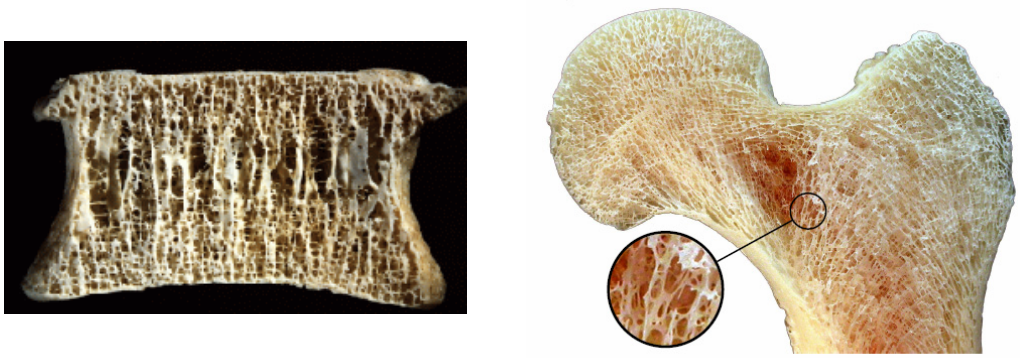

Figure 4.1: Inside a vertebral body (left) the trabeculae run mainly along the vertical and horizontal direction. Conversely, inside a femoral head (right) the trabecular arrangement is more complex and probably reflects a less simpler loading pattern.

From a mechanical view point, despite its intrinsic dynamical nature, trabecular bone architecture is normally studied considering static "snapshots". This is the point of view adopted in the second part of this thesis, where the focus will be on

the architecture-mechanics relationship in trabecular bone. An open and important question is which architectural parameters, that could ideally be measured *in vivo*, one should introduce and evaluate to have a robust prediction of trabecular fragility without performing a direct mechanical test-to-failure. Of course this is not only interesting for trabecular bone but, more in general, for all those materials which have an internal microstructure. The books of Gibson and Ashby [84] for ordered cellular solids and of Torquato [85] for random heterogeneous materials provide excellent introductions to the field.

The most established procedure to determine the effect of bone microarchitecture on its global mechanical behavior comprises three main steps. The first step is the imaging of the trabecular bone microarchitecture and the measurement of some architectural parameters. In section 4.1 the main non destructive imaging methods which allows a complete three dimensional reconstruction of the trabecular structure are presented. Successively, in section 4.2, the parameters that have been introduced to quantify the trabecular structure are reported, focusing only on those parameters which have a mechanical connotation.

The second step is to compute trabecular bone mechanical properties. This can be done with a theoretical approach, i.e., employing cellular solid theories, spring models or the finite element method. Experimental alternatives are direct mechanical tests on bone samples or techniques using rapid prototyping (see section 4.3).

The last step is to establish a connection between architectural descriptors and mechanical properties as reported in section 4.4. In general the predictive value of a parameter is investigated by looking at how much of the variations in the mechanical properties it can explain. Most of the results in this last section have been obtained with the help of cellular solid models. Cellular solids are very useful tools in studying architecture-mechanics relationships since their internal geometry can be varied in a controlled manner and the resulting effects on the mechanical performance can be established.

4.1 Imaging of trabecular bone architecture

The most used and recent three dimensional imaging techniques for the assessment of trabecular bone microarchitecture, *in vitro* and in some cases also *in vivo*, include X-ray micro-computed tomography (XRμCT), synchrotron radiation micro-computed tomography (SRμCT), peripheral quantitative computed tomography (pQCT) and magnetic resonance imaging (MRI). The first three methods are based on the attenuation of an X-ray beam through the bone sample. In fact, in XRμCT and SRμCT a bone specimen is rotated around its its central axis and at each point in the rotation the attenuation of the beam when passing thorough the specimen is collected. A mathematical reconstruction algorithm, based on the Radon transform [86], is then employed to reconstruct a full 3-dimensional image from the set of two dimensional density projections. With XRμCT nowadays a resolution of about 30 μm can be achieved, with SRμCT a resolution down to even 7 μm is feasible [87]. XRμCT has also been used *in vivo* to detect architectural changes in animal studies [88]. A very interesting approach is to use an imaging method like XRμCT or SRμCT in combination with microcompression test on bone specimen [89, 87]. Taking a series of "images" of trabecular bone during a "quasi-static" mechanical test enables a three dimensional visualization and quantification on the trabecular bone failure mechanism at the level of individual trabeculae. Those studies indicate that trabecular bone failure is characterized by the formation of localized failure bands rather than a sudden catastrophic event (see Fig. 4.2), a failure behavior known from cellular solids [90, 91].
pQCT is an *in vivo* technique used clinically which allows measurements on human extremities (typically the wrist, radius and calcaneus) with a resolution of about 100 μm. Even if the resolution is comparable with the trabecular dimensions, pQCT seems very useful since it can detect age- and disease-related changes in trabecular microstructure [92].
MRI is based on the magnetization of hydrogen nuclei and essentially produces a map of hydrogen distribution contained in soft tissue, fat and water. In MRI imaging the hydrogen of the bone marrow is viewed whereas bone itself appears dark. When used *in vitro* this technique presents a resolution down to 10 μm [93] whereas *in vivo* on the order of 150 μm [94]. The main advantage with respect to pQCT is the absence of ionizing radiation delivered to the patient.
Due to the fast improvements in the imaging technologies, is not unrealistic to think that in the near future, the full 3-dimensional trabecular architecture of living patients may be (even routinely) available. Therefore it is quite urgent to develop tools for a fast mechanical analysis of these images and which, consequently, allows a more adequate patient-specific therapy.

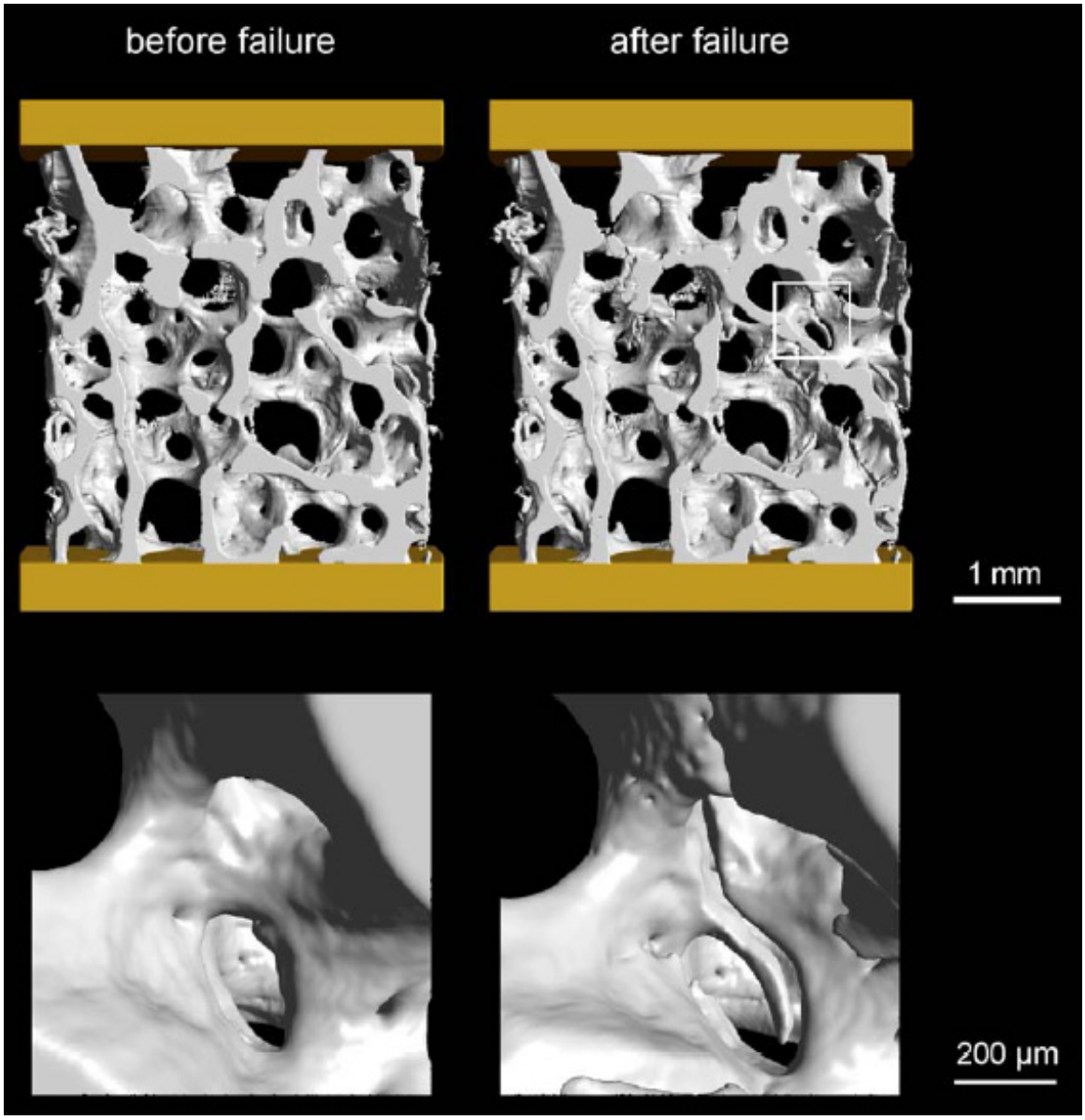

Figure 4.2: 3-dimensional visualization of a trabecular bovine bone sample subjected to compression before and after tissue failure. The image on the right side shows an oblique fracture band ranging from the upper left to the lower right of the sample. A detailed view of the region indicated in the white frame shows a crack formation and crack opening in three dimensions (from [87]).

4.2 Quantification of trabecular bone architecture

The result of the imaging methods described in the previous section is a representation of the intricate three dimensional trabecular bone architecture in a binary set of voxels. Each voxel denotes either a small cubic volume element of bone, or of marrow. The next step is to reduce this information (which for a vertebral body is about 1 GB) and therefore to search for parameters which characterize by only a few numbers the complex trabecular architecture. Among the numerous parameters which have been introduced to fulfill this task, here only parameters that have a clear mechanical connotation will be considered. They could be subdivided into five main groups, according to the quantities that they try to define:

- amount of bone
- geometry of the trabeculae
- degree of anisotropy
- connectivity
- rod-plate architecture

Anisotropy, connectivity and rod-plate architecture require a closer analysis and will therefore be presented in the three following subsections. The amount of bone is intuitively defined by counting the number of bone voxels divided by the total number of voxels. The situation already becomes more difficult when quantifying the geometry of the trabeculae with parameters like mean trabecular number (Tb.N.), mean trabecular thickness (Tb.Th) and mean trabecular spacing (Tb.Sp). Definitions of these parameters for a single trabecula can be ambiguous since trabeculae do not have simple cylindrical forms [95, 96]. In addition to those more "classical" parameters, a new set of studies try to quantify trabecular bone architecture and its changes due to osteoporosis or micro-gravity conditions, using tools from theoretical physics like symbolic dynamics, measures of complexity [97, 98] and generalized recurrence plots [99].

4.2.1 Degree of anisotropy

In general material anisotropy defines differences in the material distribution in space when measured along different axes. There are several ways to define material anisotropy and it was demonstrated that different methods yield different results [100]. The mean intercept length (MIL) was the first method introduced to measure anisotropy of trabecular bone [101]. The basic idea is to superimpose a linear grid with a given orientation α on a bone section and to count the number of intersections

I between the grid and the bone-marrow interface (see Fig. 4.3). The resulting MIL as a function of the orientation is then

$$MIL(\alpha) = \frac{L}{I(\alpha)}\,, \tag{4.2.1}$$

where L is the total line length of the grid. MIL varies with the orientation α and it was observed that for planar sections of trabecular bone, a polar plot of MIL as a function of α could be approximated by an ellipse. Generalized to 3 dimensions, MIL measurements in trabecular bone results in an ellipsoid which can be described with a second rank tensor, called fabric. The fabric tensor provides a description of the orthotropic architectural anisotropy in trabecular bone, where its eigenvectors give the three main directions of the spatial material distribution and its eigenvalues give the degree of material anisotropy along the main directions [100].

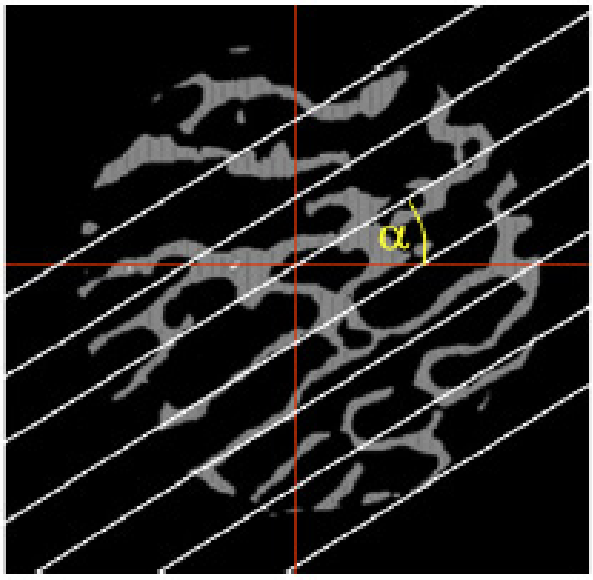

Figure 4.3: A linear grid rotated by an angle α is superimposed on a two-dimensional cross-section of trabecular bone. The mean intercept length (MIL) is calculated from the length of the intercepts between the grid and the bone structure (from [23]).

4.2.2 Connectivity

Intuitively connectivity describes the number of redundant trabeculae in cancellous bone, i.e., the number of trabeculae that may be cut without increasing the numbers of separate parts in the bone structure [102]. Connectivity is not simply a "mean"

coordination number of a structure and from topological studies it is accepted that, instead of calculating directly the connectivity of a structure, it is easier to start with the Euler number [102]. In 3-dimensional structures the Euler number, χ, is given by

$$\chi = \beta_0 - \beta_1 + \beta_2 \,, \tag{4.2.2}$$

where β_0 is the number of separated bone parts, β_1 is the number of redundant connection inside the bone structure and β_2 is the number of completely enclosed marrow cavities. For bone it is assumed that no trabeculae are completely isolated from the main structure (β_0=1) and that no marrow space exists fully isolated from the remaining environment (β_2=0). The number of redundant trabeculae can therefore be expressed as

$$\beta_1 = 1 - \chi \,. \tag{4.2.3}$$

In a voxel-based 3-dimensional reconstruction, the Euler number χ is obtained simply by looking at the voxels filled with bone and combining the number of voxel corners a_0, voxel edges a_1, voxel faces a_2 and voxel volumes a_3 inside a given volume of interest according to [100]

$$\chi = a_0 - a_1 + a_2 - a_3 \,. \tag{4.2.4}$$

In addition one has to correct for the artificially unconnected trabeculae that are generated when analyzing only a subregion of the entire trabecular network. Various algorithms for implementing these corrections are reported by Odgaard et al. [102].

4.2.3 Rods and plates decomposition

A method to simplify the complex architecture of trabecular bone, is to decompose the trabecular structure into two basic elements: rods and plates [96]. The procedure to obtain this decomposition comprises various steps [96, 103]. First, starting from a digital image of trabecular bone, a shape preserving skeletonisation algorithm with a topological optimization procedure is applied. As a result, the bone architecture is reduced to a one-voxel thick skeleton; subsequently a point classification algorithm which is able to say, for each point in the skeleton, whether it belonged to a rod or to a plate, is employed. Eventually, according to this new classification, a final algorithm is utilized to expand the elements of the skeleton to their original size. This operation results in a spatially decomposed bone structure where rods and plates are labeled with a different color (see Fig. 4.4). The overall morphology of trabecular bone can change quite a lot and, in general, low relative density structures are more rod-like whereas high relative density structures present a more plate-like architecture (see Fig. 4.4). A previous attempt for quantification of whether the structure of trabecular bone is more rod-like or plate-like was done by Hildebrand et al. [105]

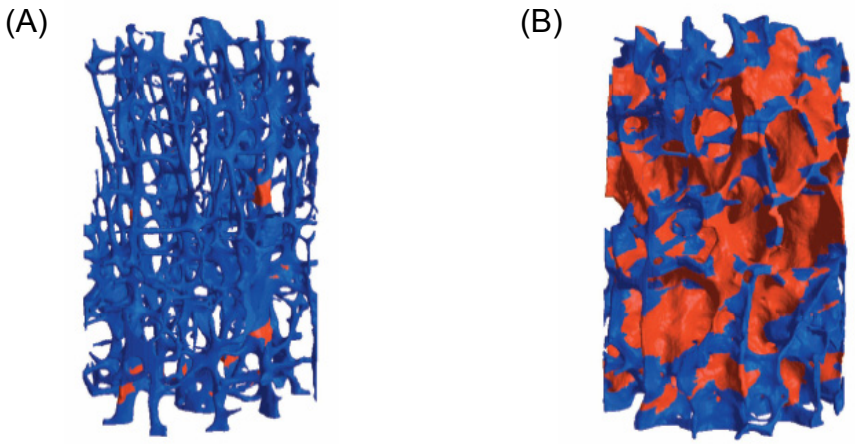

Figure 4.4: Spatial decomposition of trabecular bone into rod (blue) and plate (red) elements. (A) low relative density structures tend to have a more rod-like architecture, (B) whereas with higher relative density, trabecular bone is characterized by a more plate-like architecture (from [104]).

with the introduction of a structure model index (SMI). SMI is defined as

$$SMI = 12\,\frac{< H > BV}{BS} \tag{4.2.5}$$

where $< H >$ is the mean surface curvature, BV is the bone volume and BS the bone surface. SMI is defined in the range from 0 (for perfect plates) to 3 (for perfect rods). The main limitation of SMI was that this index is mainly determined by the arrangements of the plates, in fact for very dense plate-like structures characterized by negative mean curvature (a Swiss cheese can be an example [96]) SMI takes negative values. The spatial decomposition into rods and plates does not suffer from this limitation, and in addition, it can improve standard three-dimensional morphometry measurements when they are applied to the individual rods and plates [96].

4.3 Assessment of trabecular bone mechanics

The quantification of the mechanical performance of trabecular bone can be done in several ways. Experimentally different methods have been introduced to asses the mechanical properties of trabecular bone [106]. A direct mechanical test on a bone sample gives information of both, elastic and post-yield behavior. Compression and tensile testing have been used for measuring the Young's modulus and ultimate strength of trabecular bone [107]. However, the mechanical tests are limited by the

requirement of a bone specimen, by the destructive nature which allows a specimen to be tested only once and by the artifacts coming from the fixation of the bone sample [108]. When testing experimentally a bone sample, the result is influenced by the nonhomogeneous material properties. Being interested only in the architecture, this can be disadvantageous.
Alternatively, one can build physical replicas of trabecular bone architecture using rapid prototyping (RP) technologies [109]. In RP, starting from a digital image of a bone sample obtained for instance with μCT, a layer-by-layer physical reconstruction is obtained using as a material a photoreactive polymer. The three main advantages with respect to a direct mechanical test on bone are the possibility to reconstruct a bone model using a homogeneous material with well characterized mechanical properties, to perform multiple tests on samples with the same geometry and also to change some architectural features and to study the effects of those changes on the stiffness and strength. RP has also been used in cellular solids to study the influence of different cell geometries at equal apparent density [110].
In addition to experimental methods, the mechanical properties of trabecular bone have been evaluated also with analytical and computational tools. In the next three sections the two main computational tools and an analytical method are presented. A state of the art example of the application to trabecular bone is also given for each method.

4.3.1 Finite element method

Among all the computational methods for the assessment of trabecular bone mechanical performance, the most powerful and widely used is the finite element method (FEM). Again, the starting point can be a digital image of the trabecular bone. The architecture is discretised into elements, interconnected at points called nodes, (see Fig. 4.5) which in principle can all have different constitutive laws. Boundary conditions and external loads are then applied, the transmission of forces to all the elements in the architecture is calculated and, from the constitutive laws, deformations in each elements are derived. The FEM is an approximate method where the displacement of any points in the elements is interpolated from the displacement of the nodes. For the interpolation, linear or quadratic interpolation functions are normally used [111]. On the one hand, the FEM gives the possibility to model in great detail the trabecular geometry but, on the other hand, it is limited by the intensive computational time required. The FEM has been extensively used in the analysis of trabecular bone mechanics where in most cases isotropic material properties has been assumed.
An interesting study combined a high resolution imaging method (μCT), high resolution FEM and parallel supercomputing [113]. With these three techniques it was

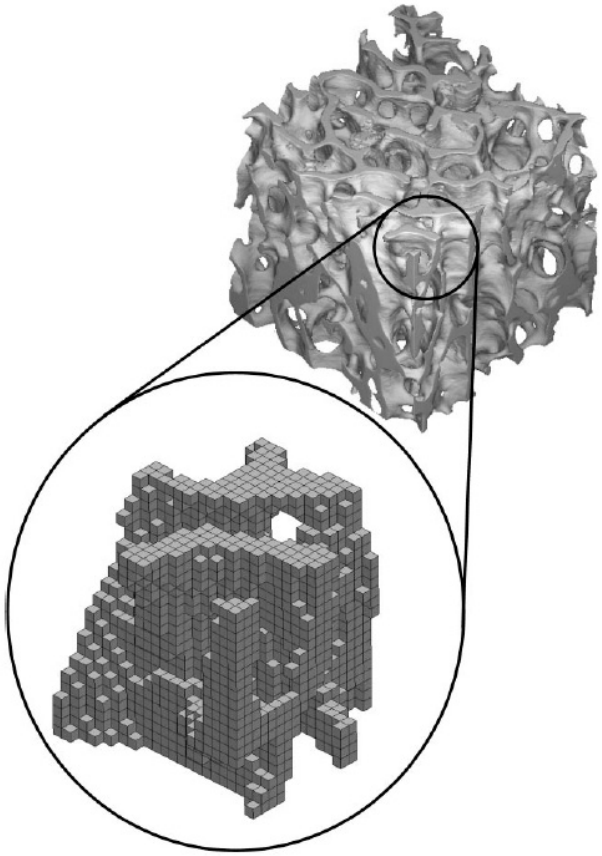

Figure 4.5: A cubic region of trabecular bone obtained with high resolution (20 μm) serial imaging and used as basis for a finite element model where each cubic element has a side of 60 μm (from [112]).

possible to compute the load distribution in an entire healthy and osteoporotic vertebral body under vertical load (the FEM employed linear elastic brick elements with a resolution of 65 μm and the computing time was roughly 20000 h CPU). The main finding of this study was that the number of highly loaded trabeculae was not higher in the osteoporotic vertebra, despite having 25% less material to carry the load than the healthy vertebra. Together with the observation that in the osteoporotic case the trabeculae were less in number, thinner, further apart, but more oriented in the axial direction, the reported simulations suggest that trabecular bone tries to compensate for the lower relative density with adapting its architecture.
An alternative to the precise but slow high resolution finite element method is given by the beam finite element models. Instead of being made up of hundreds different elements, a single trabecula is modeled with a single beam element which normally

include axial, bending and shear deformation. This "coarse grain" approach has been successfully used in combination with the possibility to reduce the complex trabecular architecture into its basic rod and plate elements (see Fig. 4.6) [114]. This approach was more than a thousand fold faster than the high resolution finite element method and the predicted elastic modulus of different trabecular bone samples was in a very good agreement with the result of the more detailed method.

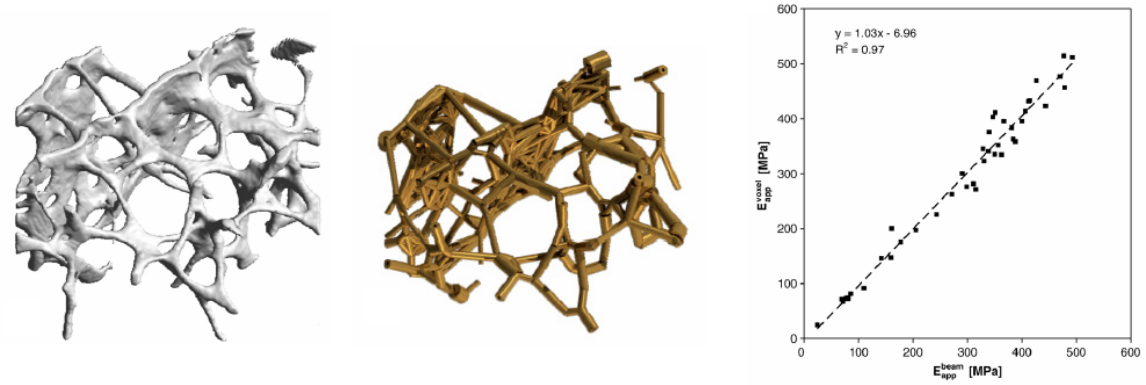

Figure 4.6: The micro-computed tomographical image (left) is reduced to its basic elements (middle): rods and plates. Each rod is modeled with a single beam element, whereas a plate with various interconnected beam elements. The correlations (right) between the apparent Young's modulus as assessed by the beam finite element models were in excellent agreement with the Young's modulus as assessed by voxel finite element models (from [114]).

4.3.2 Spring models

Another simple, fast and successful computational technique is to view the trabecular architecture as an elastic network where each trabecula is modeled with an elastic spring. The potential energy of such networks depends both on the change in length of the single springs, δr, and of the change in the bond angle between adjacent springs, $\delta\theta$. This last term takes into account that trabeculae are not freely pivoted and therefore changing angles between adjacent trabeculae requires energy. The total potential energy of such a network can be expressed as

$$U = \frac{1}{2}\sum_{struts} k\delta r^2 + \frac{1}{2}\sum_{angles} \kappa\delta\theta^2\,, \tag{4.3.1}$$

where k and κ are the stretching and the bond bending rigidity respectively. Trabecular failure can be also introduced by removing those springs whose strains exceeds a

given threshold. This is in agreement with the experimental findings that, in trabecular bone, breaking strains are almost constant independent of age [107]. Employing such a model, the relationship between strength and density for trabecular bone was investigated, in particular the reduction in strength causes by the isotropic removal of trabeculae. Gunaratne et al. [115] used two dimensional square networks of springs to study the differences in the ability to transmit the load of a model for healthy and osteoporotic trabecular bone. Starting from a network which represents a healthy vertebra, an osteoporotic scenario was simulated by removing a fraction of springs inside the network. The resulting "stress backbone", i.e. the collection of springs that are experiencing high stresses, for both cases was investigated. In the "healthy" network the majority of the springs are active in the transmission of the load and the springs experiencing high stress are evenly distributed. Conversely in the "osteoporotic" network only a small fraction of the springs carry the load which is transmitted along a few coherent pathways. On the basis of these observations an expression to relate breaking stress and density in trabecular bone different to a simple power law, like Eq. 4.3.2, was proposed [115, 116].

4.3.3 Analytical methods

Analytical approach for characterizing the mechanical response of cellular solids was pioneered by Gibson and Ashby using classical beam theory [84]. They described cellular solids with simple periodic microstructures - like honeycombs in 2 dimensions and cubic cells in 3 dimensions (Fig. 4.7) - which, under given loading conditions, can be characterized by a prevalent mode of deformation.

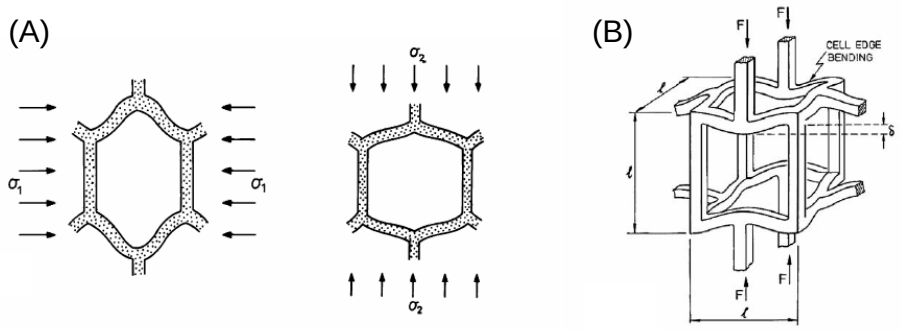

Figure 4.7: (A) honeycomb model for two dimensional materials. The deformation mechanism responsible for the macroscopic properties is cell wall bending. (B) cubic model for 3 dimensional open cell foams. Again the cell edges bend during linear elastic deformation (from [84]).

Introducing also a material failure mode (e.g., elastic bucking, plastic hinges or brittle

failure), the model predicts a power law dependence of the cellular solid stiffness, E^*, and strength, σ^*, on relative density, ρ_{rel}, which is defined as the ratio of the density of the cellular solid, ρ^*, to the density of the material, ρ_s,

$$\frac{E^*}{E_s} = C_E \left(\rho_{rel}\right)^{\alpha_E} \quad \text{and} \quad \frac{\sigma^*}{\sigma_s} = C_\sigma \left(\rho_{rel}\right)^{\alpha_\sigma} \ . \tag{4.3.2}$$

E_s and σ_s are material properties. The value of the density exponents α_E and α_σ depends on the governing deformation mechanism and failure mode. For structures and loading directions where the microscopic deformation is stretching or compressing, the Young's modulus changes linearly with the density. The maximum value for α_E is obtained in pure bending and is 3 in two-dimensions and 2 in three-dimensions. For three dimensional structures which fail by elastic buckling α_σ is 2, whereas if the failure is through the formation of plastic hinges or brittle crushing, α_σ=3/2. According to this model, more complex geometries only enter in the coefficients C_E and C_σ.

4.4 Architecture-mechanical properties connection

Only a few of the very different architectural descriptors of trabecular bone can be directly connected to mechanical properties. The connection with mechanics is easier within the cellular solid framework (trabeculae are idealized as cylinders) where both analytical methods as well as numerical simulations are generally employed to estimate the mechanical behavior. Despite their intrinsic strong idealization, cellular solid models have been used successfully to explain both qualitatively and quantitatively why the mechanics of trabecular bone should depend on architectural parameters like relative density, orientation, connectivity and trabecular geometry.

4.4.1 Relative density, stiffness and strength

The main predictor of the mechanical properties of trabecular bone and, more in general, of cellular materials is the volume fraction or relative density. When the power law model of Gibson and Ashby [84] is applied to trabecular bone (see Fig. 4.8), despite the substantial scatter, the Young's modulus scales approximately with an exponent from 2 to 3 and the strength with an exponent of 3. This suggests a deformation mode by bending and failure by buckling of the trabeculae.

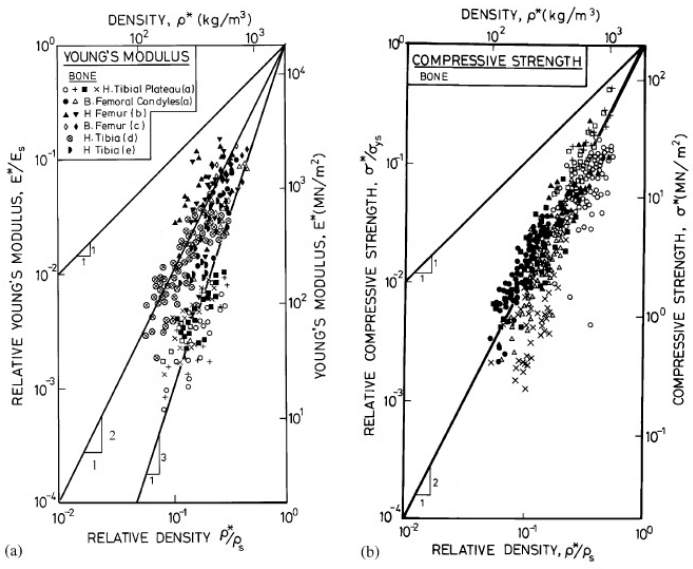

Figure 4.8: Trabecular bone stiffness against its relative density is plotted on the left. The resulting scaling law suggests that trabecular architecture deforms primarily by bending of the trabeculae. Compressive strength versus relative density plotted on the right (from [84]).

4.4.2 Fabric and and elastic coefficients

Continuum mechanics theory can be applied to trabecular bone when it is studied at the proper length scale. A representative volume element covering at least 5 trabecular spacings, i.e., about 5 mm, can be described with an equivalent continuum medium [117] which follows the general Hooke's law

$$\sigma_{ij} = C_{ijkl}\epsilon_{kl}\,, \tag{4.4.1}$$

where σ_{ij} are the components of the stress tensor, ϵ_{kl} are the components of the strain tensor and C_{ijkl} are the coefficients of the elastic matrix forming a 4-th order tensor. From the continuum elasticity point of view, it was found that trabecular bone possesses orthotropic symmetry [118], therefore its elastic matrix is characterized only by nine independent elastic coefficients. Cowin [119] was the first to introduce an algebraic procedure to relate the elasticity tensor to the fabric tensor under the assumption that the maximum mechanical anisotropy allowed is orthotropic. In Cowin's equations the stiffness properties are related to the eigenvalues of the fabric tensor (H_1, H_2 and H_3), the second invariant II of these eigenvalues ($II = H_1H_2 + H_2H_3 + H_1H_3$), and nine functions depending on the relative density ($k_1(\rho_{rel})$ $-$ $k_9(\rho_{rel})$) as follows [120]:

$$C_{iiii} = E_s\left(k_1 + 2k_6 + (k_2 + 2k_7)\,II + 2\,(k_3 + 2k_8)\,H_i + (2k_4 + k_5 + 4k_9)\,H_i^2\right) \tag{4.4.2}$$

$$C_{iijj} = E_s\left(k_1 + k_2 II + k_3\,(H_i + H_j) + k_4\left(H_i^2 + H_j^2\right) + k_5 H_i H_j\right) \tag{4.4.3}$$

$$C_{ijij} = E_s\left(k_6 + k_7 II + k_8\,(H_i + H_j) + k_9\left(H_i^2 + H_j^2\right)\right)\,, \tag{4.4.4}$$

where

$$k_i = k_{ia} + k_{ib}\,(\rho_{rel})^p\,. \tag{4.4.5}$$

In these relationships eighteen constants, k_{ij}, $i = 1, ..., 9$, $j = a, b$, which do not have any clear physical meaning, must be determined by a fit with the mechanical parameters. Making use of the Fourier expansion of the orientation distribution function that characterizes the trabecular microstructure, Zysset and Curnier [121] developed an alternative model reducing the number of free parameters to five.
The fabric-elasticity framework has been successfully applied to trabecular bone. In two separated studies Kabel et al. [122] and Zysset et al. [123] showed that the predicted values of the elastic coefficients using relative density and fabric tensor are in good agreement with results from finite element computations. Homminga et al. [120] extended the method to the analysis of osteoporotic trabecular bone and showed that the relations (in terms of the fit parameters) for normal bone are valid for osteoporotic bone as well.

4.4.3 Connectivity and deformation mechanism

The influence of connectivity on the mechanical performance of trabecular bone is still controversial. The lack of correlations between the results form high resolution finite element simulations with measurements of connectivity (computed from the Euler number) suggests that connectivity has basically no influence on the linear elastic properties of trabecular bone [124, 125]. Conversely, cellular solids theory predicts that the mode of deformation, and therefore the mechanical performance of periodic cellular structures is dependent on the node connectivity, i.e., the number of struts joined at a node. Periodic lattices have stiff stretching-dominated architectures (meaning that each beam of the lattice deforms only by tension/compression) for all loading states if the node connectivity is at least 6 in 2 dimensions and 12 in 3 dimensions. For smaller connectivities, less mechanically efficient bending-dominated architectures are attained [126]. In trabecular bone, however, such high node connectivity values are never observed.
The impact of connectivity is also evident when studying the effects of thinning versus removal of struts in two and three dimensional cellular solid models as well as in disordered cubic networks. Silva et al. [90] and Vajjhala et al. [43] found that stiffness and strength are reduced more dramatically when the relative density of a cellular material is decreased by a random removal of struts than by a uniform thinning. Random removal of struts reduces both the trabecular number and the connectivity of the network. Similar results were obtained by Gunaratne et al. [115] where the trabecular architecture was mapped into a network of elastic springs with stretching and bond-bending potentials. Again the breaking stress of the network was strongly influenced by removing those springs rather than by softening them.
In the next chapter we present our own attempt to define a local predictor based on trabecular architecture and on cellular solid theory.

Chapter 5

Mechanical analysis based on node properties

In the second part of this thesis, the possibility to define a more "local" and "mechanical - motivated" descriptor of the trabecular architecture will be investigated. The idea is to look at how the behavior of local "nodes" in the trabecular structure influences the mechanics of the trabecular network. A node is defined by a certain number of trabeculae which come together to a junction point (see Fig. 5.1). Assuming constant material properties, the mechanical performance of such nodes depends locally on the number and thickness of the trabeculae (node relative density), on the spatial directions of the trabeculae (node geometry) and on the type of load coming to the node which is dictated by the surrounding environment. The aim of the analysis is to characterize nodes as weak, meaning they could act as starting points for failure and the failure bands could pass through those points. A trabecular structure with a lot of weak nodes possibly concentrated in a small region should be more prone to fracture than a structure with fewer more isolated weak nodes.

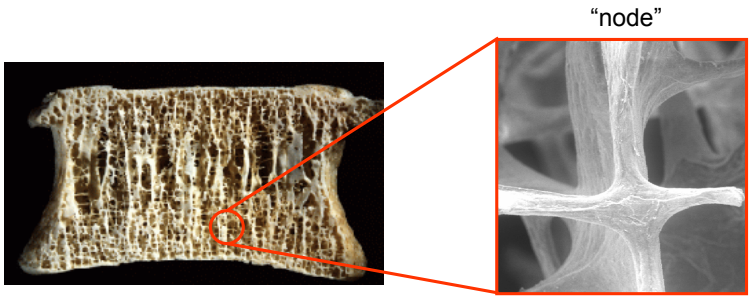

Figure 5.1: An example of trabecular architecture inside a vertebra. The zoom shows a typical "node" which is the local mechanically-motivated "basic building block" that will be investigated in this thesis.

Due to the rather complex architecture of trabecular bone it is easier to develop this new method with the analysis of a 2-dimensional cellular solids. Even if those model systems are a strong idealization of the trabecular microstructure, they can provide useful insights in the mechanical behavior of more intricate materials.
In the cellular solid framework a node is defined by a junction point and by the set of beams connected to this point. In their pioneer analysis of cellular materials Gibson and Ashby [84] mainly looked at single beams. Focusing on nodes could be the "next step" of that approach in the sense of a "cluster expansion" as performed in other fields of physics. Only nodes with a coordination number of 3 - which results in honeycomb structures - will be considered since they are easier to characterize and standard Cauchy elasticity can still be used [127, 128].

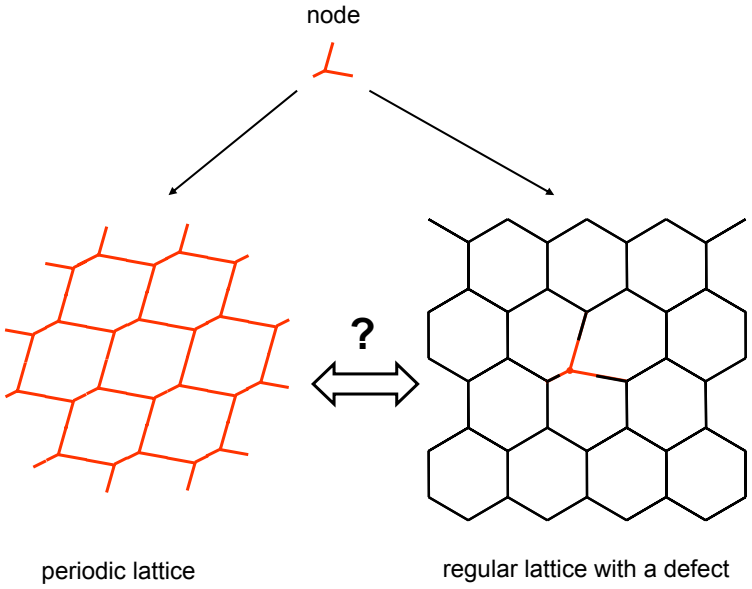

Figure 5.2: Starting with a given node (top), a periodic lattice can be build by tiling the space with infinite copies of the same node (left). The node can be introduced in a regular lattice where it acts as a defect being different from all the other nodes of the lattice. The question is how much of the behavior that a node has in the periodic lattice will be "inherited" when the node is place inside the regular lattice.

In principle the mechanical behavior of a node depends on its geometry and on the surrounding environment. To understand the relative contributions of those two quantities the following procedure is introduced (see Fig. 5.2). First a node, characterized by a given geometry, is chosen. The second step is to build a periodic lattice by tiling space by periodically repeating the node (Fig. 5.2, left) . In this situation, since the lattice is made up of infinite copies of the same node, the geometry of this single node is sufficient to determine the "global" mechanical performance of the lattice which

coincides with the "local" performance of each constituent node. The last step is to place the same node, which has been characterized in a periodic lattice, in a different environment. A natural choice is to locate the node as a defect inside a regular hexagonal lattice where all the other nodes are identical (Fig.5.2, right).
In this work the following question will be investigated: How much can we learn from a node in its own periodic environment, to understand its mechanical behavior when it acts as a defect in a regular lattice. In particular when a given node is "globally" weak, i.e., in the periodic lattice, does it also behave "locally" weak, i.e., when it is placed as a defect inside a regular lattice?
If the local node geometry is sufficient to define (or at least to suggest) the local node behavior, the application to trabecular bones follows in a natural way. Ideally one could scan the trabecular architecture, identify local weak regions and, without performing a direct mechanical test, estimate the strength of the structure.

5.1 Choosing the nodes

To assess the importance of nodes on the mechanical properties of lattice structures, the first step is to select the different node geometries that will be investigated. A node with a coordination number of three (i.e., three beams joined at a junction point) is characterized by 11 parameters: 3 lengths, 3 thicknesses, 2 angles and 3 different elastic moduli. A significant reduction of the parameters space is obtained when the characterization is restricted to nodes that can - geometrically speaking - act as defects inside a regular lattice. A regular lattice is made up of regular hexagonal cells, all having equal edge length a. Different defects in the regular lattice are generated following the scheme in Fig. 5.3.

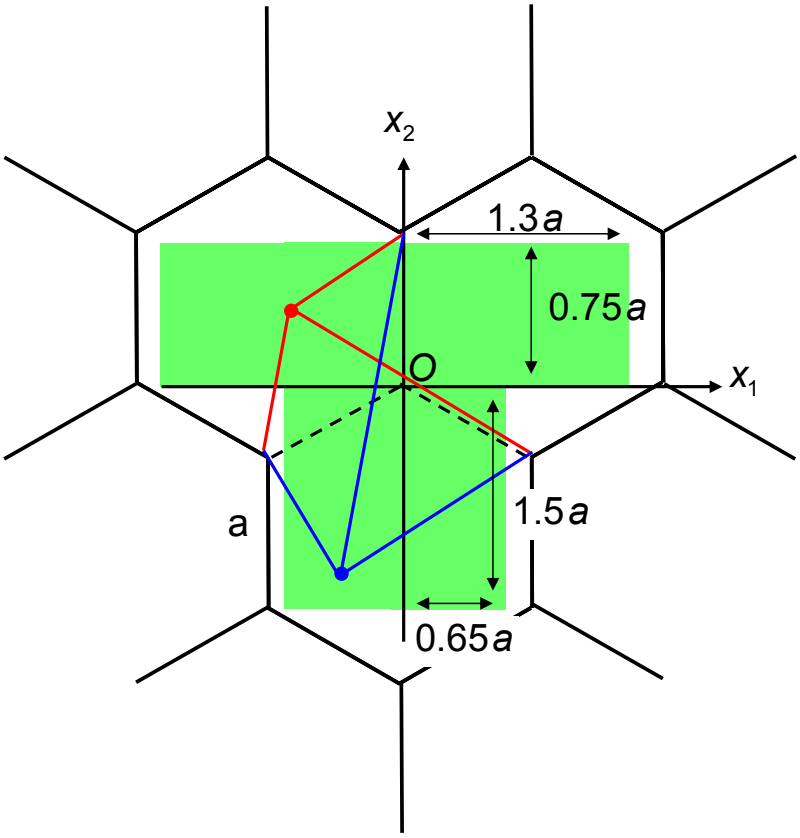

Figure 5.3: Close up of a regular hexagonal lattice where a single node can be perturbed by shifting the position of its junction point O inside a given region (green area). The size of this region is given in terms of the lattice dimension a. The rectangular shape of this region is chosen for convenience.

Starting from a node in the regular lattice which has its junction point O in the origin of the coordinate system (X_1, X_2), a new node is obtained simply by shifting this junction point to a new position within the predefined green area. Examples are the red and blue nodes in Fig. 5.3, obtained first by positioning the junction point and then by attaching this junction point at the fixed frame of the regular lattice. Defining a new junction point position is therefore equivalent to defining a new node. It is then convenient to choose a specific region, inside which the new junction points (and therefore the nodes) are generated. The size and shape of this area are given in Fig. 5.3. After generating a node, a periodic lattice made up of infinite copies of that node is build and its elastic properties are solved analytically (section 5.2). The same node is then considered as a defect in a regular lattice (like in Fig. 5.3 for the red or blue nodes) and its behavior as well as the behavior of its neighborhood is computed numerically (section 5.3).
A comparison is then performed between what the node is doing in a periodic lattice and what it is doing when inserted as a defect in a regular lattice. The aim is to check how much of the node behavior can be understood in terms of only local node geometry. For computational reasons, the comparison is restricted only to symmetric defects, i.e., only at nodes that are obtained by shifting their junction points along the vertical X_2 direction of the coordinate system shown in Fig. 5.3.

5.2 Node in a periodic lattice - analytical solution

When a given node is surrounded by infinite copies of itself it defines a periodic lattice. The mechanical behavior of the lattice can be derived analytically by looking only at a single node. Under the assumption that each beam of the node is described with standard beam theory with axial and bending deformations (no shear is considered), the full elastic matrix of the periodic lattice can be derived as a function of the node geometry and material properties [127].

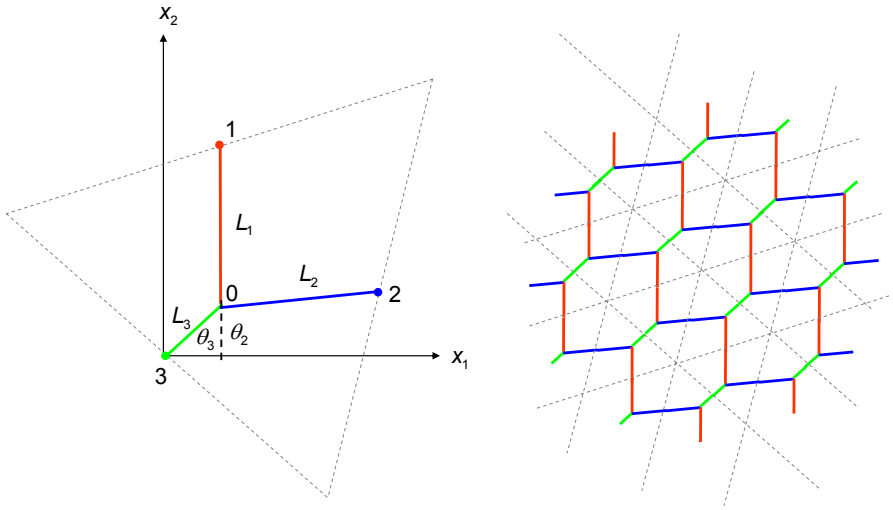

Figure 5.4: The node on the left is the basic building block of the periodic lattice on the right (not in scale). The node is defined by three beam lengths (L_1, L_2 and L_3) and two angles (θ_2 and θ_3) which meet at a junction point O.

Fig. 5.4 shows, on the left, a node with its geometrical properties and, on the right, the resulting periodic lattice obtaining by reflecting and inverting this node. In general each of the beams belonging to a node could have different geometries (length, cross section and orientation) and different material properties (Young's modulus). This is visualized using different colors in Fig. 5.4. The dashed triangle between points 1, 2, and 3 identifies the area corresponding to the node which is defined by the intersection of the lines connecting all the midpoints of the same periodically repeating beams (beams with the same color in Fig. 5.4).
The mechanical formulation to obtain the elastic matrix of the periodic lattice is based on the fact that the deformation of the node is completely defined by the displacement of two beam midpoints (e.g., point 1 and 2 in Fig. 5.4) relative to a reference point (e.g., point 3 in Fig. 5.4) and by the relative displacement and rotation of the junction

point (point O in Fig. 5.4). The rotations of the beam midpoints are not independent variables since the moments there are zero due to symmetry conditions, therefore these rotations do not have to be taken into account explicitly. This last observation motivated the choice to study structures with a coordination number $Z = 3$ which can still be described as an equivalent Cauchy continuum. For coordination number $Z > 3$ the rotations at the unit cell midpoints become independent variables and therefore the node is equivalent to a Cosserat or micropolar medium [128]. Following the method suggested by Overaker et al. [127], the periodic lattice can be described by an equivalent continuum material with a general constitutive relation expressed (in Voigt notation) as

$$\begin{bmatrix} \sigma_{11} \\ \sigma_{22} \\ \sigma_{12} \end{bmatrix} = \begin{bmatrix} C_{11} & C_{12} & C_{13} \\ C_{12} & C_{22} & C_{23} \\ C_{13} & C_{23} & C_{33} \end{bmatrix} \begin{bmatrix} \epsilon_{11} \\ \epsilon_{22} \\ 2\epsilon_{12} \end{bmatrix} \tag{5.2.1}$$

where, in general, each term of the stiffness matrix is a function of 11 parameters which characterized the node

$$C_{ij} = f(r_1, r_2, r_3, L_1, L_2, L_3, \theta_2, \theta_3, E_{s1}, E_{s2}, E_{s3})\,. \tag{5.2.2}$$

An important case which will be considered as a "reference" situation when studying the influence of different node geometries, is the regular node where all the beams have equal lengths ($L_1 = L_2 = L_3 = L$), cross sections ($r_1 = r_2 = r_3 = r$), orientations ($\theta_2 = \theta_3 = \pi/3$) and material properties ($E_{s1} = E_{s2} = E_{s3} = E_s$). The resulting lattice, called regular lattice, is mechanically isotropic and its stiffness matrix can be given in a quite simple form

$$C = \begin{bmatrix} \frac{\sqrt{3}(N+3M)}{12M(N+M)} & \frac{\sqrt{3}(N-M)}{12M(N+M)} & 0 \\ \frac{\sqrt{3}(N-M)}{12M(N+M)} & \frac{\sqrt{3}(N+3M)}{12M(N+M)} & 0 \\ 0 & 0 & \frac{\sqrt{3}}{6M(N+M)} \end{bmatrix}, \tag{5.2.3}$$

where M and N are the axial and bending compliances. When the beam cross section is circular, they read as

$$\begin{aligned} M &= \frac{L}{AE_s} = \frac{L}{\pi r^2 E_s} \\ N &= \frac{L^3}{3E_s I} = \frac{4L^3}{3\pi r^4 E_s}\,. \end{aligned} \tag{5.2.4}$$

For the general case the expressions of the stiffness coefficients as a function of the node geometry are extremely long. They have been computed using a symbolic mathematic software.

5.3 Node as a defect in a regular lattice - numerical solution

In our context a regular lattice is defined as a mechanically isotropic lattice and its basic building block is the regular node. When a node inside the regular lattice is perturbed, as described in section 5.1, a defect is created. The mechanical behavior of this node as well as the behavior of the resulting lattice cannot be solved analytically. To investigate this situation one has to use numerical simulations and the finite element method (FEM) is probably the most suitable and precise tool available to solve such mechanical problems. In this thesis the finite element calculations are performed with the commercial package ABAQUS. Each beam of the lattice in the finite element approach is modeled with 4 Timoshenko beam elements with quadratic interpolation functions. They allow for axial, bending and transverse shear deformations. The resulting mesh is accurate enough to model linear elastic properties [129]. Each beam has the same material properties (Young's modulus of 1 MPa and Poisson ratio of 0.3) and equal circular cross section. The slenderness ratio of the beams, i.e., the length divided by the thickness, is 0.001. This low value was chosen for two reasons. First to have a low relative density (ca. 1.1% for the regular lattice) that allows the analytical solution to be very precise. Second, to reduce the influence of transverse shear deformations, which are not included in the analytical model presented in section 5.2 and therefore to allow a better comparison between the obtained results.
When simulating finite structures, in order to avoid end effects in term of localization of deformation at the boundaries [130], periodic boundary conditions (PBC) have to be used. In the present work, PBC for the displacement field have been implemented. Those conditions are attained by coupling opposite faces and linking the corresponding degrees of freedom. Each boundary point has 3 degrees of freedom, two translational and one rotational. The PBC requires that

$$u_a^J - u_a^I = \epsilon_{\alpha\beta}\left(x_\beta^J - x_\beta^I\right),\ \theta^J - \theta^I = 0 \tag{5.3.1}$$

where $\epsilon_{\alpha\beta}$ is the average macroscopic strain, u_α^J, θ_α^J and x_β^J are respectively the displacement, the rotation and the coordinates of two representative point J and I at the edge of the macroscopic structure [131].
To choose the proper size of the lattice for the simulations, one needs to reach a compromise between two different requirements. First, since PBC are used, the lattice must be big enough to ensure that a defect located in the center of the lattice does not see its periodic images. The second requirement is to keep the lattice rather small to guarantee a reasonable computational time. In this work the lattices have 61 unit cells in the horizontal direction and 69 unit cells in the vertical direction, which results in square-shaped system with a side length of approximately $105a$.

5.4 Mechanical scenarios investigated

The lattices have been studied under three different loading conditions, which correspond to uniaxial stress along the X_1 direction, uniaxial stress along X_2 and hydrostatic stress.
For periodic lattices, where the analytical solution is available, the characterization is done for all the node inside a given area (see Fig. 5.3). The numerical simulations, computationally more expensive, are restricted to lattices with symmetric defects. In addition, a case where the defect is not geometrical but comes from reducing the radius of all the three beams belonging to a node by 1/5, is studied. The types of defects introduced in the regular lattice are shown in Fig. 5.5.

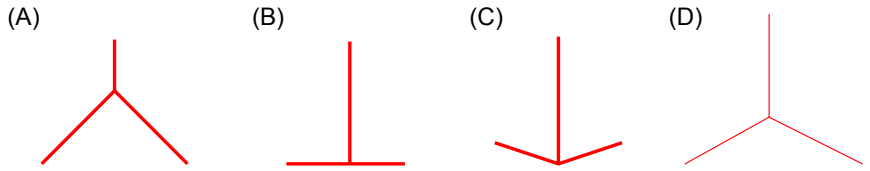

Figure 5.5: (A) defect obtained by displacing the junction point along the positive vertical direction X_2 by $0.5a$. (B) T-shaped defect resulting when shifting along X_2 the junction point by -0.5a. (C) arrow-shaped defect with the junction point at -0.75a. (D) regular node with thinner beams; the thickness is reduced by 1/5.

In the following section all the local mechanical quantities are always referred to the nodes. Further the quantities are normalized to the corresponding value of the regular node to see the amount of improvement or degradation in the mechanical performance with respect to the isotropic regular lattice. In the analytical case the deformations of the nodes are computed by the compliance matrix of the nodes multiplied by the applied stress. When numerical simulations are used the node deformations are derived on the basis of the three displacements at the node boundaries [127]. The strain energy density is derived analytically according to

$$SED = \frac{1}{2}\frac{\mathbf{C}\epsilon^2}{A_{node}} \tag{5.4.1}$$

where $\mathbf{C}$ is the elastic matrix, ϵ the strain tensor and A_{node} the area corresponding to the node. Numerically it is obtained first by summing the strain energy in the three beams coming together at the junction point and then dividing by the node area. In order to visualize the strain energy density distribution inside the lattice (e.g., Fig. 5.8) a rectangular patch is drawn at the center of each junction point and the strain energy density of the node containing the junction point is used as an index to determine the color of the patch.

5.5 Results and discussion

The mechanical behavior of a node depends on its morphology, relative density and orientation with respect to the loading direction. The environment in which the node is placed is also fundamental in translating the global far-field stresses or strains in local mechanical actions. In the framework of 2-dimensional cellular solids, when a node is placed in a periodic lattice, its mechanical behavior, corresponding to the performance of the entire lattice, can be derived analytically in terms of the node geometry. Conversely, numerical simulations are needed to solve the behavior of a node acting as a defect inside a regular lattice. In the following, the behaviors of periodic lattices and regular lattices with different defects are investigated and compared. The aim is to see by which extent the behavior of a node in a periodic lattice can explain what the same node is doing as a defect inside a regular lattice.

5.5.1 Periodic lattices

The linear elastic analysis of periodic lattices is fast to perform since the elastic and compliance matrices of those structures are known as a function of the their geometry. Fig. 5.6 shows the maximum strain and strain energy density for the different periodic lattices constructed (section 5.1). The maximum strains in the lattice are evaluated on the basis of the eigenvalues of the strain tensor. When a given lattice is compressed along the horizontal X_1 direction, the minimum deformation is obtained when the junction point (from which the node and therefore the lattice is derived) belong to a line parallel to the X_1 axis. This occurs for a junction point with the coordinates (0, -0.5a) (see Fig. 5.6A). In this situation, the beams L_2 and L_3 are aligned with the loading direction which results in extremely stiff lattices since the underling deformation mechanism is only beam-compression. In this case the strain energy adsorbed is approximately four order of magnitude less then the strain energy stored in the regular lattice (Fig. 5.6D). Moving the junction point along the vertical X_2 direction (which is perpendicular to the loading condition) results in lattices which have bigger strains and strain energy variations than when the junction point is shifted along horizontal paths.

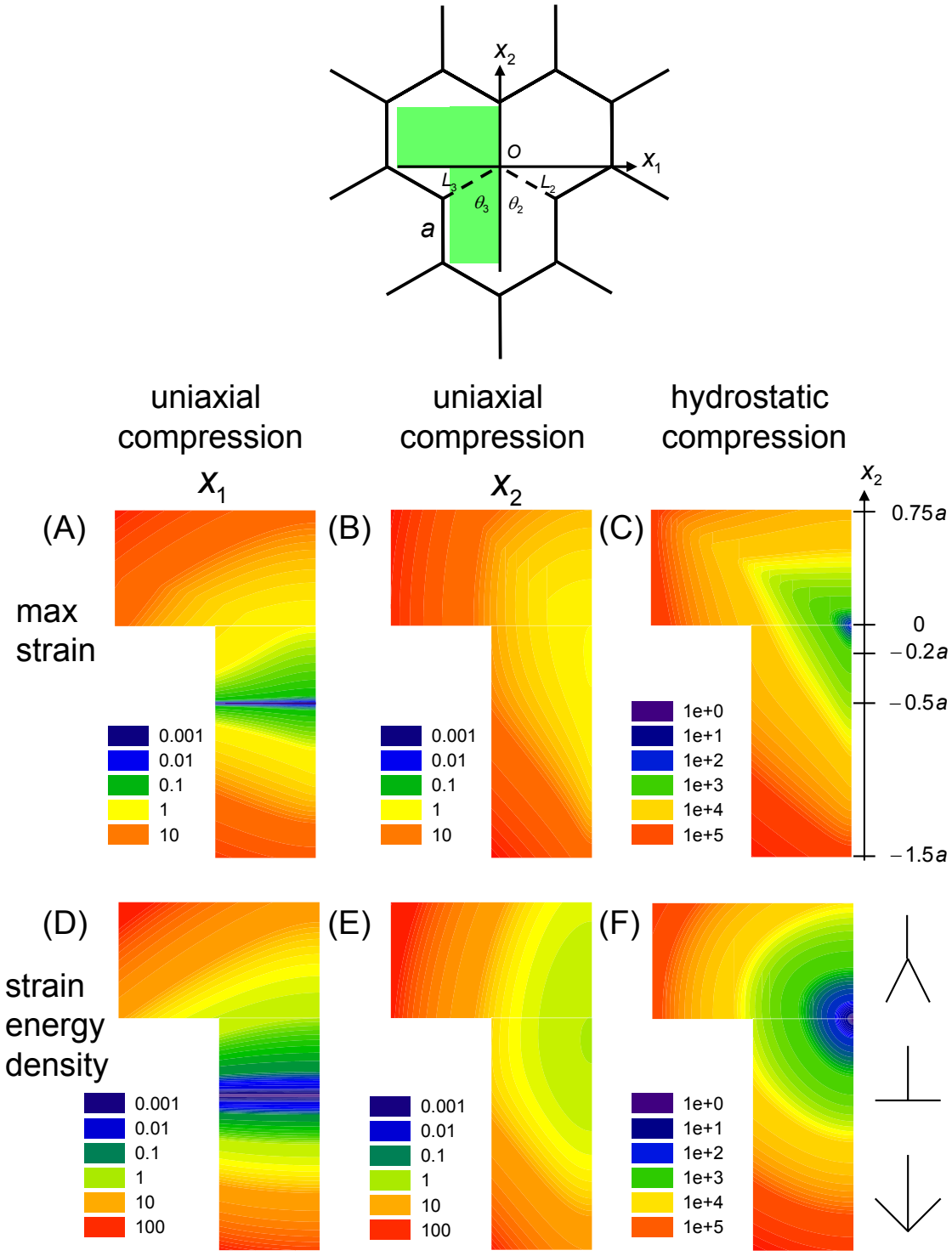

Figure 5.6: Contour plots of the maximum strain and strain energy density for different loading conditions and for constant relative density of the different periodic lattices.

For a compressive load in the vertical X_2 direction the stiffest lattice is not the regular isotropic one but a lattice which is obtained when the junction point is moved along the vertical X_2 direction of about -0.2a (Fig. 5.6B, E). This can be understood in terms of simple beam bending. The bending moment acting on the beam L_2 (or equivalently L_3) is proportional to $L_2\, sin(\theta_2)$. As the junction point is moved in the negative X_2 direction, L_2 decreases and θ_2 increases. There is a minimum in $L_2\, sin(\theta_2)$ which occurs approximately in -0.2a.
Hydrostatic compression results in much stronger variations in maximum strain and strain energy density with respect to the regular lattice (Fig. 5.6C, F). Interestingly the hydrostatic load of the regular lattice is characterized by pure axial deformations. This is an optimal condition for light load bearing materials, since the elastic properties scales only linearly with the relative density [84] which can therefore be quite low without a strong degradation in the mechanical performance. Small deviations from the regular geometry leads to bending and therefore to a strong increase in the amount of energy absorbed.
In general, different periodic lattices, obtained by varying the junction point positions as sketched in Fig. 5.3, not only have different geometries but also different relative densities. To weight this effect on the mechanical properties, the Young's moduli and Poisson ratios of constant versus variable relative densities structures are compared. To keep a constant relative density which correspond to the relative density of the regular lattice, the beam lengths are uniformly rescaled. The plots in Fig. 5.7 show the normalized apparent stiffness along the global X_1 and X_2 directions and the Poisson ratios for periodic lattices. Those structures are generated by varying continuously along the vertical X_2 direction the position of the node's junction point. The Young's moduli are normalized by the Young's modulus of the regular lattice. The dramatic decrease in the strain energy for uniaxial compression along X_1 direction observed in Fig. 5.6D when the junction point is at $-0.5a$, corresponds here to a huge increase in the stiffness: E_1 is in this case more than three orders of magnitude bigger than E_{1-0} as can be seen in the semi-logarithmic plot in Fig. 5.7A. Interestingly the normalized Young's modulus in the X_2 direction (Fig. 5.7B) both for constant and for variable relative density displays a maximum not when the junction point is at position zero (regular lattice) but for a somewhat negative displacement of the junction point. This reflects the minimum in the strain energy observed in Fig. 5.6E and again is understood by considering that the uniaxial deformation mainly involved beam bending which in turn is governed by the length L_2 and the angle θ_2. In the case of variable relative density, what intuitively seems to be the weaker lattice (T-shaped node), turned out to be the stiffer one due to the particular combination of strut lengths and angles. However, in both cases the stiffening effect is quite small (maximum increase in E_2 is about 15%) compared to the degradation of the elastic properties obtained when the junction point has other positions along X_2. The Poisson ratios ν_{12} and ν_{21},

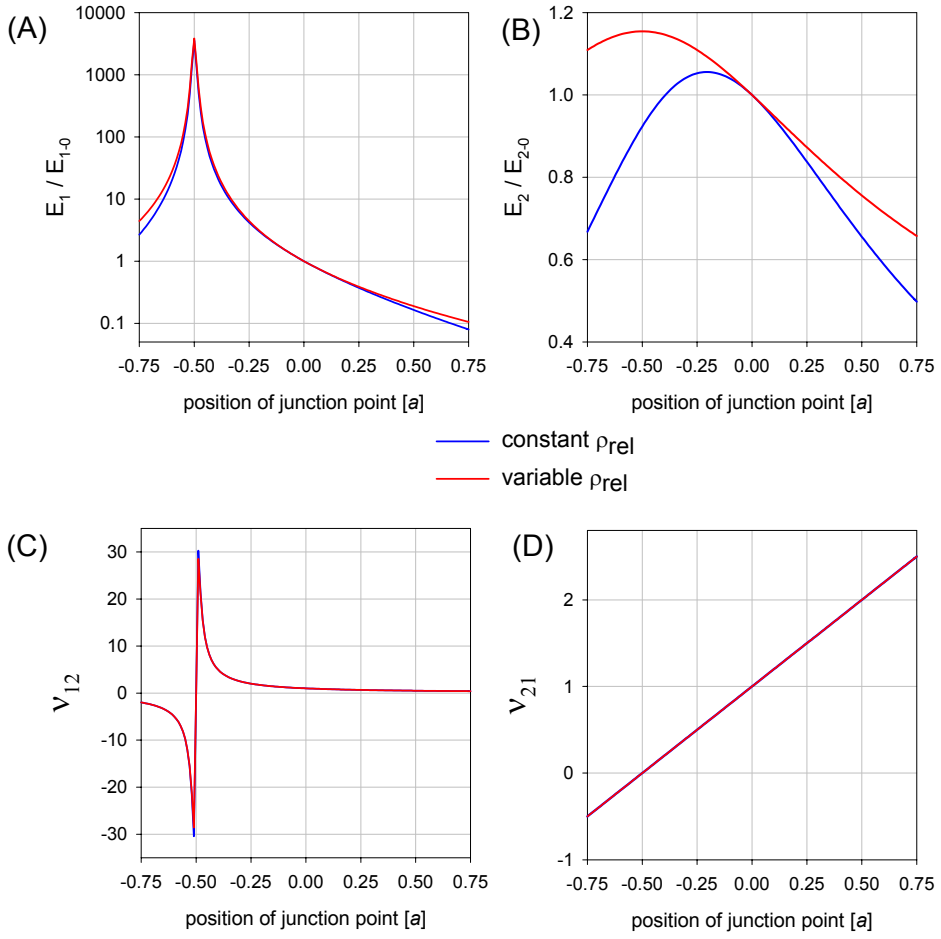

Figure 5.7: Elastic properties of periodic lattices obtained by shifting the node junction points along the vertical X_2 direction.

which relate deformations perpendicular to the loading direction with deformations in the same direction of the load, show a behavior independent of the relative density and basically dictated by the angle θ_2 (and equivalently θ_3). When $\theta_2 < 90$ (junction point positions $> -0.5a$) the orientation of the tilted beams is such that, under uniaxial compression, they will tend to rotate "outward" hence producing compression forces on the adjacent nodes and therefore a positive Poisson ratio effect. Conversely, when $\theta_2 > 90$ (junction point position $< -0.5a$) the beams in the node will try to rotate "inward", yielding tensile stress in the lateral direction and thus a negative Poisson ratio effect. The transition from positive to negative Poisson ratio occurs at the junction point position of $-0.5a$ where the X_1 and X_2 directions are decoupled.

5.5.2 Defect in regular lattice

In general a node within a lattice responds to an external mechanical load not only as a function of its geometry but also depending on the neighboring environment. A symmetric type of defect was introduced inside a regular lattice (as described in section 5.1) and the mechanical behavior of the imperfection as well as of the entire lattice is investigated. The focus is on the spatial distribution of the strain energy density (SED), a scalar quantity which summarizes the complex tensorial nature of the stress and strain fields. In a regular lattice each node absorbs the same amount of energy during the linear deformation process and obviously the SED is uniformly distributed. When a defect is introduced, a redistribution of the SED occurs with the possibility of SED localization somewhere in the lattice. Those regions may be weak zones in the structure since they could act as sites of failure initiation.
In the following plots the SED has been normalized by SED_0 which is the amount of energy adsorbed by a node in a regular lattice (defect free) and which corresponds (approximately) to the SED of nodes far from the defect. For clarity, only a subregion of the simulated lattice with the size of 16 times 15 unit cells, and containing approximately 960 nodes, i.e., approximately 1/40 of the lattice, is plotted. Already a first look at Fig. 5.8, which corresponds to uniaxial compression along X_1, reveals the intricate effect of perturbations. In Fig. 5.8A a node of the regular lattice has been perturbed by displacing its junction point in the positive X_2 direction of an amount equal to $0.5a$. The SED shows a pronounced anisotropic behavior with a horizontal band, where the absorption of strain energy is reduced. The band involves a number of nodes on both sides of the defect. Fig. 5.8B shows the behavior of a T-shaped node. Intuitively and according to the analytical study of section 5.2, this node is as stiff as possible in X_1 direction since its beams are align with the loading. Another characteristic, still in the periodic lattice, is that its Poisson ratio equals zero meaning that horizontal and vertical deformations are decoupled. Placed inside a regular lattice, this node has a very low SED adsorption (90% less than the nodes located far away from the defect), and in turn produces a strain energy density increase (almost 100%) in its neighboring node placed just above it. When the defect is arrow shaped (Fig. 5.8C), which corresponds to a very weak mechanical behavior according to the periodic lattice point of view, the SED increases more than 150%. The node that feels this SED concentration once again is not the perturbed one, but the nearest neighbor located just above the defect. Even more surprising is the complex pattern obtained when the node has similar morphology but different beam thickness (Fig. 5.8D). The beam thicknesses of the node are reduced to 1/5 of the thickness of all the other beams, therefore increasing the axial and bending compliances (see Eq. 5.2.4) by 25 and 625 times, respectively. This extremely weak node give rise to a 75% SED increase which, also does not occur at the location of the weak node itself but in the third neighbors.

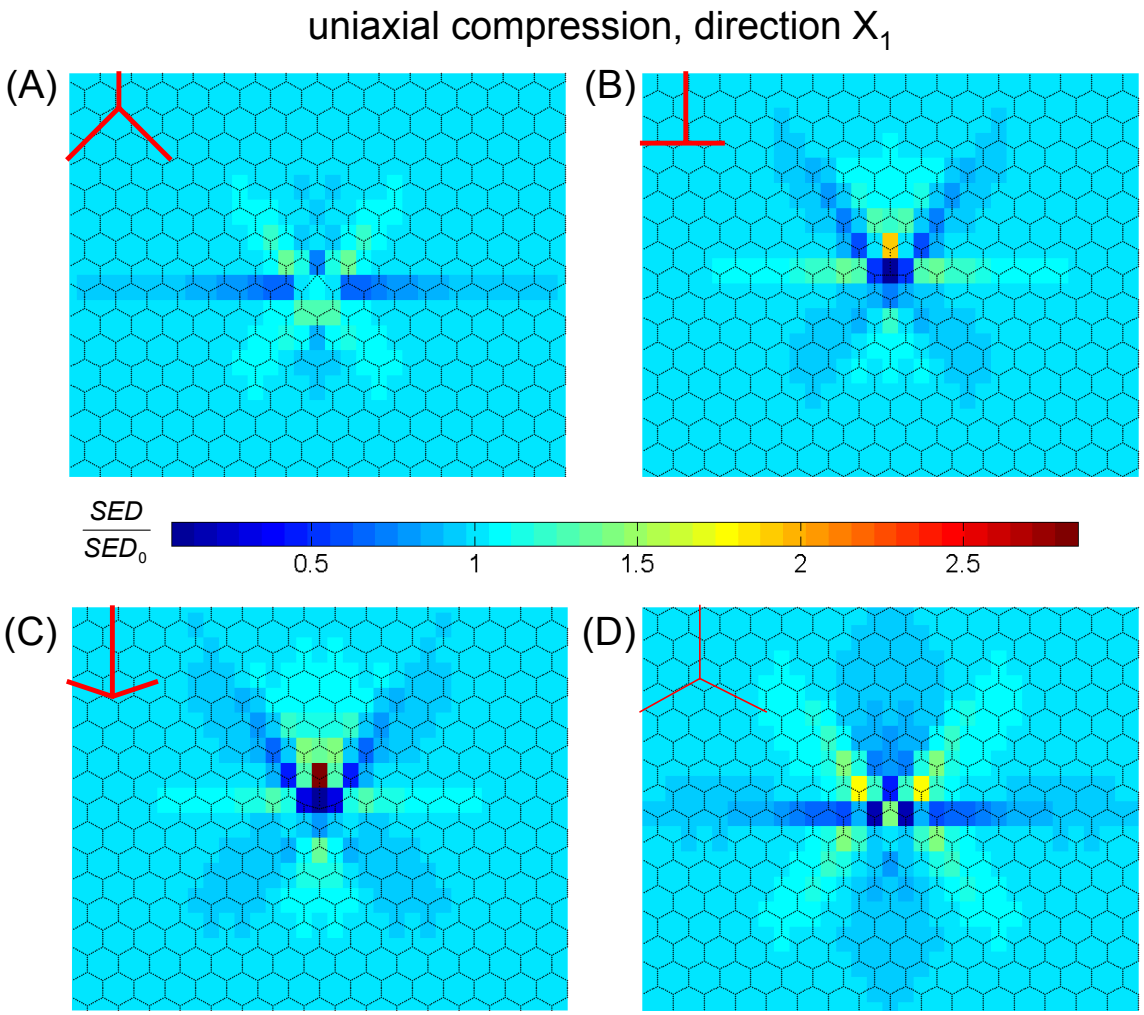

Figure 5.8: Compression in X_1 direction and strain energy density (SED) normalized by the strain energy density of the regular lattice without defects (SED_0). In (A) the node is obtained by a positive displacement of the junction point. (B) shows a T-shaped node and (C) an arrow-shaped defect. Case (D) instead illustrates the effect of a reduced cross-section keeping the same morphology. The red nodes on the upper left corner represents the type of defect introduced in the middle of the regular lattice.

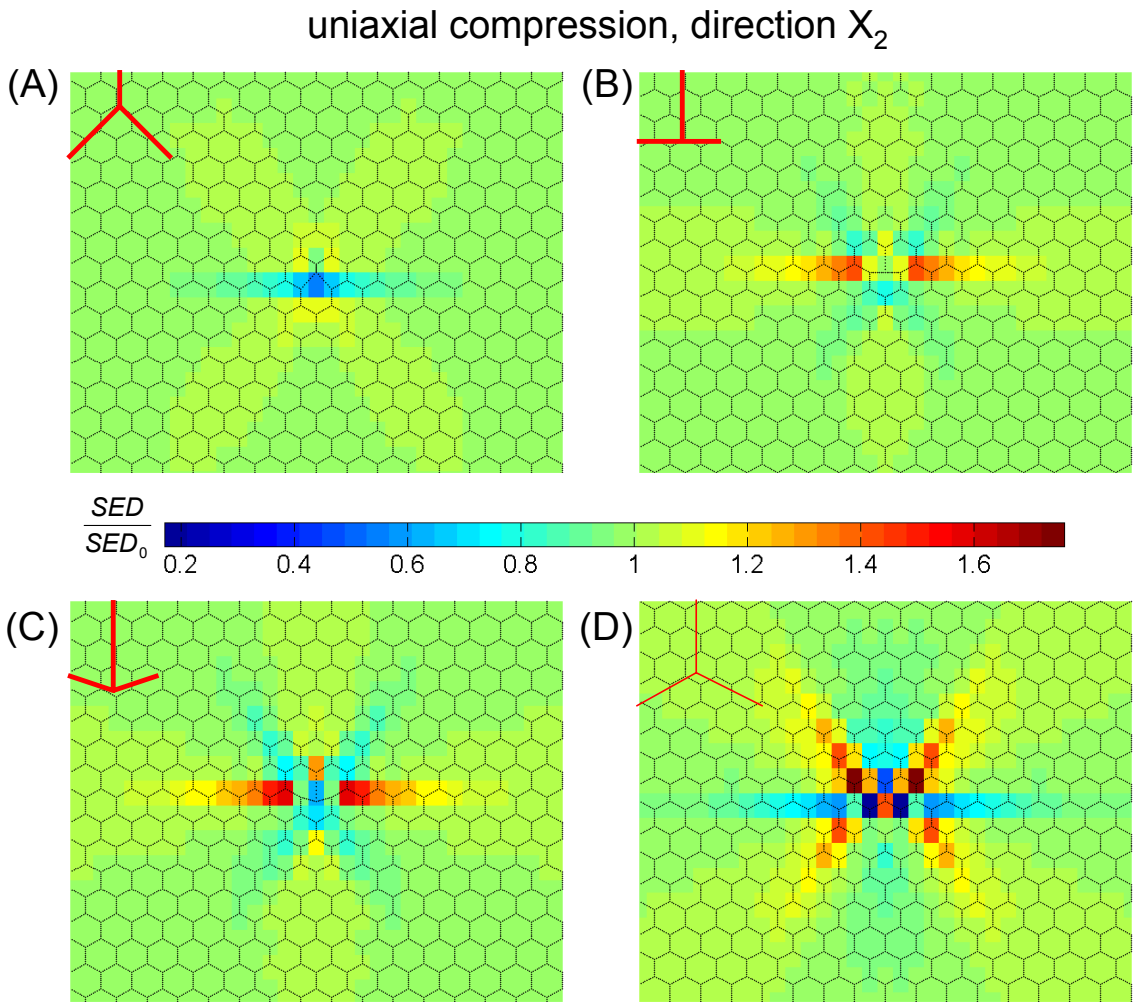

Figure 5.9: Compression in X_2 direction and strain energy density (SED) normalized by the strain energy density of the regular lattice without defects (SED_0). Note the different "background" color with respect to Fig. 5.8, which is due to a slightly different scaling of the colorbar to account for different extreme values of the SED. In (A) the node is obtained by a positive displacement of the junction point. (B) shows a T-shaped node and (C) an arrow-shaped defect. Case (D) instead illustrates the effect of a reduced cross-section keeping the same morphology. The red nodes on the upper left corner represents the type of defect introduced in the middle of the regular lattice.

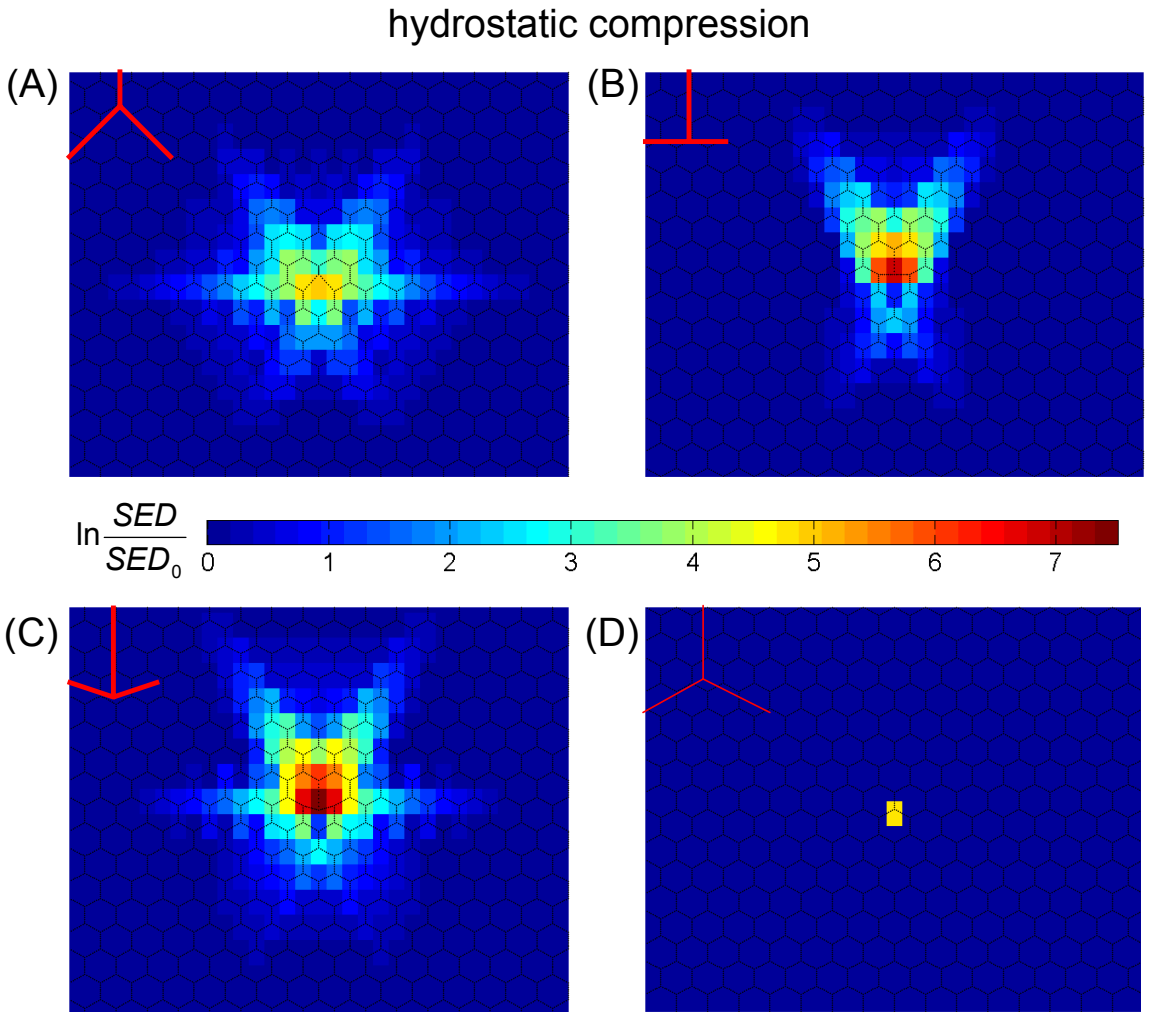

Figure 5.10: Hydrostatic compression and strain energy density (SED) normalized by the strain energy density of the regular lattice without defects (SED_0). Here the scale is logarithmic to better visualize the higher strain energy localization. In (A) the node is obtained by a positive displacement of the junction point. (B) shows a T-shaped node and (C) an arrow-shaped defect. Case (D) instead illustrates the effect of a reduced cross-section keeping the same morphology. The red nodes on the upper left corner represents the type of defect introduced in the middle of the regular lattice.

The above observations are qualitatively valid also when the lattice is compressed along the vertical X_2 direction (Fig. 5.9). Here the "background" color, corresponding to the far field SED, is slightly different from the one of Fig. 5.8 because the maximum and minimum SED observed in the lattice under different loading directions are different and the colorbars are accordingly rescaled. Again in the cases (A), (B) and (C) the perturbed node is the one that adsorbed less energy during deformation. In addition, it creates elaborate and anisotropic SED distributions with the common characteristics that the maximum SED is always occurring at the second neighbor. It should be pointed out that this is the location of the first regular node, since the first neighbor of the defected node is geometrically slightly different from the regular node.
A different behavior is attained when the lattice is compressed hydrostatically (Fig. 5.10). Now, the node which has been perturbed, is indeed the one subjected to the higher SED. Another difference with the uniaxial compression is the dramatic SED concentration caused by the defect. In (C) for instance the SED increases more than 3 orders of magnitude (note the logarithmic scale) with respect to the far field value. This is understood in terms of micro-mechanical behavior. In hydrostatic compression of the regular lattice, no beam bending is taking place and the only deformation mechanisms is axial compression. Introducing a single defect, locally modified the deformation mechanism from stretching to bending which in turn increases the energy adsorption in the node. Although not well presented by the logarithmic scaling, the SED returns very rapidly to SED_0, when moving away from the defect. For the case of the thinned regular node (Fig. 5.10D), it is interesting to notice how the localization only occurs at the weak node, thus leaving the remaining region of the regular lattice unaffected.

In summary, the SED patterns present three prominent characteristics. First, they are all symmetric, which simply reflects the symmetry of the defects. Second, the SED pattern display strong anisotropy, which result in strain energy "localization" along specific directions. Third, for the uniaxial cases, the defect causes a significant change in the SED of the neighbors also far away from its position.

5.5.3 Strain energy density comparison

In order to test whether the "global" behavior of a node, i.e., extended to a periodic lattice, could help to understand its "local" behavior, i.e., inserted as a defect in a regular lattice, the normalized SED in those two situations are compared. For computational reasons the evaluation is restricted to symmetric defects.
The three plots of Fig. 5.11 show the SED for periodic lattices -both for constant (black) and variable (red) relative density-, the SED for symmetric defects (blue) and the maximum SED of a node observed inside the regular lattice with a defect (green). All the SED are normalized by SED_0 of the regular node.
For uniaxial compression along the X_1 direction (Fig. 5.11A) the behavior of the node which acts as a defect inside a regular lattice, is partly similar to the behavior of the same node inside a periodic lattice. When the node is obtained starting with a junction point which is moved along the negative X_2 direction, both the SED in the periodic and in the regular lattice decreases substantially. A proportional corresponding increase in the SED is seen in the neighborhood of the defect (Fig. 5.11A, green). For positive displacements of the junction point, the node behavior in the periodic and the regular lattice is quite different.
When the compression occurs along the X_2 direction (Fig. 5.11B) the perturbed node in the regular lattice shows the opposite behavior of that calculated from the periodic lattice. Nodes which are defined as globally weak, (displaying a high SED in the periodic lattice) show in the regular lattice a low SED, as can be seen by the different curvature of the black and blue lines.
When the compressive load is hydrostatic, the perturbed node is the weakest point in the regular lattice (see Fig. 5.11C). Therefore what the node is doing globally, as part of the periodic lattice, corresponds to what it does locally, acting as a defect. This is only true in a qualitative way since quantitatively the SED still differ considerably. For example the SED for the T-shaped node is almost three times bigger in the periodic lattice than in the regular one.

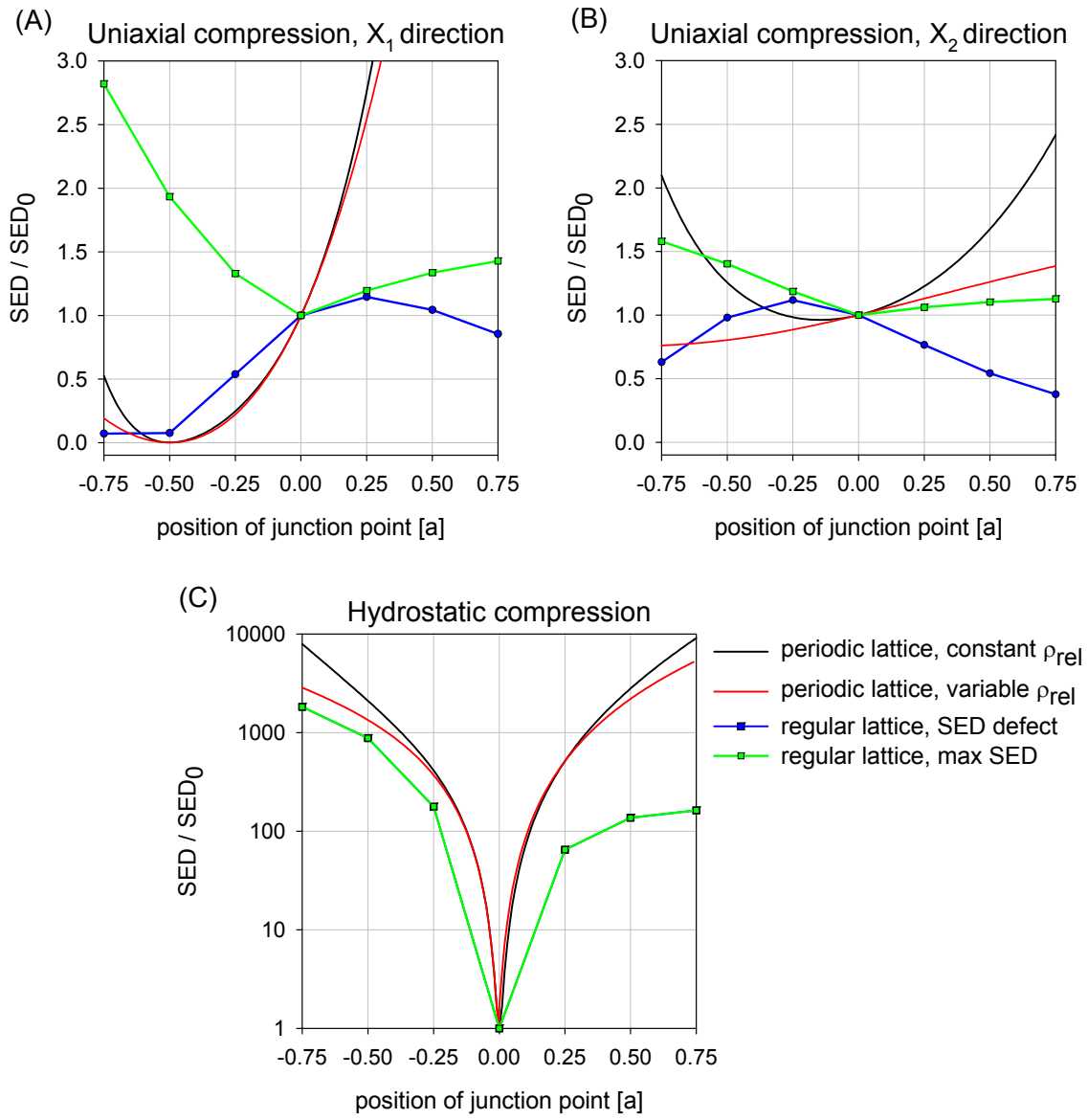

Figure 5.11: The SED/SED_0 calculated for the periodic lattices, for constant and variable relative density, is compared with the values predicted by the finite element analysis for the regular lattices with a defect. The maximum strain energy density in the finite element lattice is also shown.

5.6 Conclusions and outlook

Our simulations demonstrated that, at least for the uniaxial cases, when a node differs too much from its environment, it is "protected" instead of being locally subject to concentrated mechanical actions. The inability of the regular lattice to load its defect could be interpreted looking at the serial/parallel arrangement of a two phase composite material, imaging that the regular lattice is like a matrix (black in Fig. 5.12) and the symmetric defect acts like a weak inclusion (red stripe in Fig. 5.12).

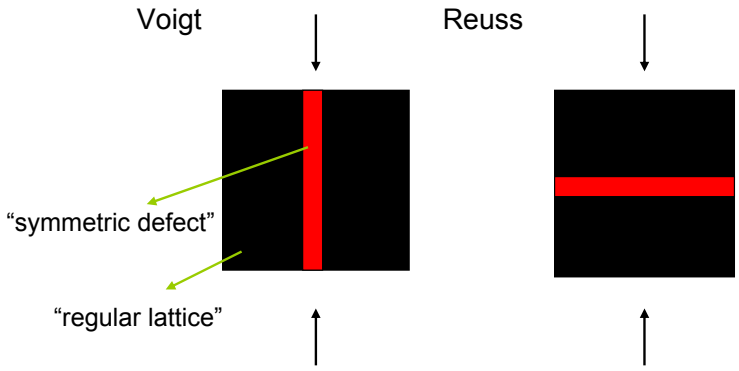

Figure 5.12: Voigt and Reuss mechanical arrangement of the regular lattice with a symmetric defect.

In the serial arrangement (Reuss) both the matrix and the inclusion feels the same stress, therefore the weak inclusion is fully loaded and its global behavior will be sufficient to explain the local one. Conversely, in the parallel arrangement (Voigt), the two phases are subject to the same deformation. Now this stiff matrix protects the soft inclusion by being loaded.
The situation in the regular lattice with a symmetric defect is surely more complex than this simple Voigt/Reuss arrangement. Nevertheless the SED redistribution and the comparison with the global node behavior seems to suggest that under uniaxial loading all the nodes have a more "parallel" behavior whereas under hydrostatic compression, from a mechanical view point, they are "arranged in series".
The main conclusions of the node analysis is that the "globally" weak nodes are not necessary "locally" weak. This is due to the fact that beside node geometry, the interaction with the environment, seems to be important as the node geometry itself in defining the node behavior. Nevertheless, nodes with a mechanically disadvantageous geometry contribute to a weakening of the lattice by concentrating the strain energy on their neighbors. The simulations have been performed on hexagonal lattices with coordination number three. An important next step is to test whether our results

transfer also to square-like lattices which are closer to the architecture of trabecular bone. The observation that weak elements in the structure are shielded by the neighborhood deserves attention also when thinking about bone remodeling. Inside a honeycomb-like architecture, thinner or weaker trabeculae are not necessary highly loaded. Algorithms for bone remodeling are based on the paradigm that thinner structures obtain a higher local SED and therefore thicken following the Wolff-Roux law [33, 132]. In honeycomb structures, since weaker nodes do not seem to concentrate the SED, instead of being reinforced by adding new material they seem to be even more prone for resorption. Therefore it may not be possible to mechanically control a remodeling of such type of architectures. One could speculate that this may be the reason why only a small fraction of lattice geometries are realized in nature.

Appendix A

Finite volume method

The explicit numerical integration scheme for solving equation 3.1.6 is based on the finite volume method presented in section 3.1.4. As already mentioned, Eq. 3.1.6 is first subdivided into two subproblems and only problem (A) needs to be solved with the finite volume method.
An explicit time marching algorithm, which accounts also for variable velocities, has the following form

$$\rho_i^{n+1} = \rho_i^n - \frac{\Delta t}{\Delta c}\left(v_i\rho_i^n - v_{i-1}\rho_{i-1}^n\right) - \frac{\Delta t}{\Delta c}\left(\tilde{F}_{i+1/2} - \tilde{F}_{i-1/2}\right) , \tag{A.0.1}$$

where $\tilde{F}_{i+1/2}$ and $\tilde{F}_{i-1/2}$ are suitable numerical fluxes, obtained by controlling the form of the solution, ρ_i^n, to avoid instabilities.
Here, only the expression for the flux at the left boundary of a grid cell is reported. The flux at the right boundary is derived in a similar way. Within the finite volume framework, $\tilde{F}_{i-1/2}$ reads as

$$\tilde{F}_{i-1/2} = \frac{1}{2}\rho_i^n\left(1 - \frac{\Delta t}{\Delta c}\rho_i^n\right)\phi\left(\theta_{i-1/2}^n\right)\Delta\rho_{i-1/2}^n , \tag{A.0.2}$$

where $\phi(\theta_{i-1/2}^n)$ is a flux limiter function. One choice for the limiter can be the monotonized central-difference limiter (MC limiter) which has the following expression [80]

$$\phi(\theta_{i-1/2}^n) = max\left[0, min\left(\frac{1+\theta_{i-1/2}^n}{2}, 2, 2\theta_{i-1/2}^n\right)\right] , \tag{A.0.3}$$

where $\theta_{i-1/2}^n$ is defined as

$$\theta_{i-1/2}^n = \frac{\Delta\rho_{i-1-1/2}^n}{\Delta\rho_{i-1/2}^n} = \frac{\rho_{i-1}^n - \rho_{i-1-1/2}^n}{\rho_i^n - \rho_{i-1/2}^n} \tag{A.0.4}$$

and $\rho_{i-1-1/2}^n = v_{i-2}\rho_{i-2}^n/v_{i-1}$, $\rho_{i-1/2}^n = v_{i-1}\rho_{i-1}^n/v_i$. Good results were obtained with this choice of the limiter.

Appendix B

Publications

1. D. Ruffoni, P. Fratzl, P. Roschger, K. Klaushofer and R. Weinkamer.
   The bone mineralization density distribution as a fingerprint of the mineralization process.
   Bone 40, 2007: 1308-1319

2. D. Ruffoni, P. Fratzl, P. Roschger, K. Klaushofer and R. Weinkamer.
   Simulations of changes in the BMDD after increase/decrease in turnover rate.
   Manuscript prepared for submission.

3. D. Ruffoni, J.W.C. Dunlop, P. Fratzl and R. Weinkamer.
   A simple mechanical model to evaluate the effect of defects in honeycomb lattices.
   In preparation.

ELSEVIER

Bone 40 (2007) 1308–1319

BONE

www.elsevier.com/locate/bone

The bone mineralization density distribution as a fingerprint of the mineralization process

D. Ruffoni [a], P. Fratzl [a], P. Roschger [b], K. Klaushofer [b], R. Weinkamer [a,*]

[a] *Max Planck Institute of Colloids and Interfaces, Department of Biomaterials, 14424 Potsdam, Germany*

[b] *Ludwig Boltzmann Institute of Osteology at the Hanusch Hospital of WGKK and AUVA Trauma Centre Meidling, 4th Med. Department Hanusch Hospital, A-1140 Vienna, Austria*

Received 16 May 2006; revised 22 December 2006; accepted 19 January 2007
Available online 25 January 2007

Abstract

The inhomogeneous mineral content and its topographical distribution on a microscopic scale are major determinants of the mechanical quality of trabecular bone. The kinetics of bone tissue deposition and resorption together with the kinetics of the mineralization process determine the distribution of mineral in the tissue. The heterogeneity of the mineral content is described by the well-established bone mineralization density distribution (BMDD), which is experimentally accessible, e.g., using quantitative electron backscattering imaging (qBEI). In the present work, we demonstrate that the shape of the BMDD histogram of trabecular bone reflects directly the mineralization kinetics. Based on the experimental BMDD data of trabecular bone from healthy human adults and using a mathematical model for the remodeling and the mineralization process, the following main results were obtained. The peaked BMDD reflects necessarily a two-phase mineralization process with a fast primary phase and a slow secondary phase where the corresponding time constants differ three orders of magnitude. The obtained mineralization law, which describes the increase in the mineral content in a bone packet as a function of time, provides information not only about the initial mineralization surge, but also about the slow increase afterwards on the time scale of years. In addition to the mineralization kinetics the turnover rate of the remodeling process has a strong influence on the peak position and the shape of the BMDD. The described theoretical framework opens new possibilities for an analysis of experimentally measured BMDDs with respect to changes caused by diseases or treatments. It allows addressing whether changes in the BMDD have to be attributed to a variation in the turnover rate which consequently affects the density distribution or to a primary disorder in the mineralization process most likely reflecting alterations of the organic matrix. This is of important clinical interest because it helps to find therapeutic approaches directly targeting the primary etiological defects to correct the patients' BMDD towards normal BMDD.

Keywords: Bone mineralization density distribution; Theoretical model; Mineralization kinetics; Remodeling; Turnover

Introduction

The mean mineral content of the bone matrix and the heterogeneity of the mineralization, together with its spatial distribution are all fundamental factors for bone material quality since they affect the basic mechanical properties of bone tissue: the stiffness, the strength and the toughness [1–6]. The non-uniform mineralization in terms of bone packets of different mineral content is the result of (i) the bone remodeling process [7] and (ii) the kinetics of mineralization in the newly deposited bone packet [8,9]. Once mineralization has started in the unmineralized bone matrix (osteoid) deposited by the osteoblasts, a continuous increase in its mineral content occurs. The *mineralization law* describes this change as a function of time. It has been reported that the mineralization process initially results in a rapid increase in the mineral content during the first few days up to 70% of the final value, a phase typically referred to as *primary mineralization*, followed by a slow and gradual maturation of the mineral component, called *secondary mineralization* [9–14]. The kinetics corresponds to a mineralization law with a steep slope in the beginning and a significant reduction of the slope afterwards [15]. However, a

* Corresponding author. Fax: +49 331 567 9402.
E-mail address: richard.weinkamer@mpikg.mpg.de (R. Weinkamer).

8756-3282/$ - see front matter © 2007 Elsevier Inc. All rights reserved.
doi:10.1016/j.bone.2007.01.012

more detailed mathematical formulation of the mineralization law, especially its development beyond the first weeks, is still missing.

The non-uniform distribution of the mineral content in trabecular bone can be measured by a variety of experimental techniques: quantitative microradiography (qMR) [16], quantitative backscattered electron imaging (qBEI) [17–20] and synchrotron radiation microtomography (SR μCT) [21]. The results of these measurements are often summarized in the so-called bone mineralization density distribution (BMDD), which is a frequency distribution of the calcium (Ca) content found in the bone sample. qMR is based on unidirectional X-ray projection and absorption within 100 μm thick bone sections. The BMDD is derived from the contact microradiograph by pixel analysis (2-dimensional bone image elements). However, this technique is flawed due to projection effect errors [22]. qBEI makes use of the fact that the intensity of electrons backscattered from the surface (surface-layer smaller than 1 μm in thickness) of a sectioned bone area is proportional to the concentration of bone mineral (calcium). Darker areas represent lower levels of mineralization (younger bone tissue) and lighter areas higher levels of mineralization (older bone tissue) (Fig. 1A). The BMDD is derived from the qBEI images on a pixel basis. The method is well established and validated, it achieves a technical precision of 0.3% and a histogram resolution in Ca content values in steps of 0.17 weight percent (wt%). SR μCT method is based on multidirectional projection and absorption of a focused, monochromatic X-ray beam by blocks of bone. The information obtained from the three-dimensional measuring technique is combined with an image processing method that derives BMDD from analysis of voxels (three-dimensional bone image elements). This method is rather new and still in development.

Measurements with qBEI showed that the BMDD of trabecular bone from healthy adults is almost constant independent of age, sex, ethnicity and skeletal site [18,23]. This BMDD is bell shaped, with a peak at about 23 wt% Ca content and a slight asymmetry towards lower Ca concentrations (Fig. 1B). This mineral distribution will be referred to as *reference BMDD* in the following. Metabolic bone diseases or drug therapies, however, result in significant deviations from this healthy BMDD [23]. For instance, in the case of osteoporotic patients the peak of the BMDD is shifted towards lower values of the Ca content with an increased heterogeneity of the mineral content [24]. In contrast, an antiresorptive treatment over a period of 2 to 3 years leads to a shift to higher calcium contents and to a narrowing of the BMDD peak, i.e., the mineralization is more homogeneous [25–27]. At a longer period of treatment (>5 years), the BMDD peak becomes wider again [28,29]. When osteoporotic patients get anabolic treatment by intermittent PTH administration, the BMDD shifts towards lower mineralization density accompanied with an increase in peak width [9].

The main purpose of this paper is to demonstrate that the BMDD includes valuable information about the mineralization kinetics. To show this, we introduce a model that relates changes

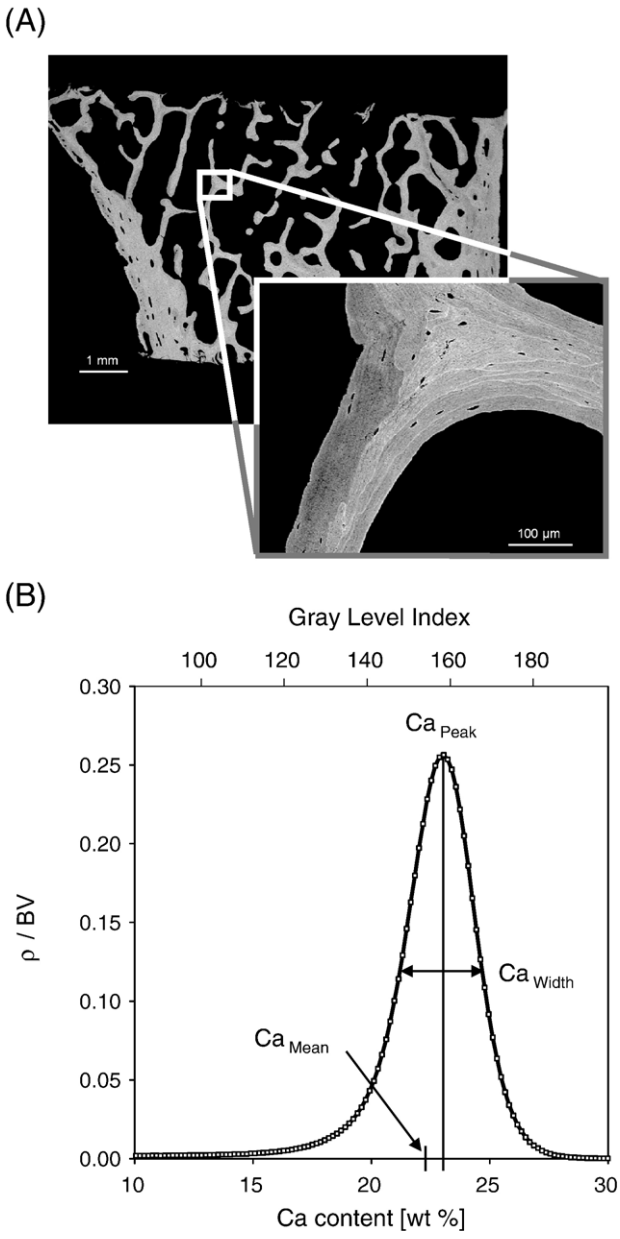

Fig. 1. (A) Backscattered electron image of transiliac bone biopsy (healthy female, 35 years), the soft tissue or embedding medium is black while the mineralized bone tissue is gray. The entire sectioned trabecular bone tissue area is analyzed by the qBEI method to determine the BMDD. By zooming in, individual bone packets of different degree of mineralization that composed the trabecular bone can be seen. Dark gray means low mineral content, light gray high mineral content. (B) Corresponding BMDD histogram with the definitions of the most frequent calcium content (Ca_{Peak}), mean calcium content (Ca_{Mean}) and full-width at half maximum of the peak (Ca_{Width}).

in the BMDD with the remodeling and the mineralization process. Based on the experimental evidence that the reference BMDD remains virtually unchanged with time [23], the model allows a prediction of

(i) the mineralization law for healthy trabecular bone, and
(ii) how changes in the turnover rate are reflected in changes of the mineralization distribution.

The model

We present here a description of the model and a listing of all the model assumptions without using mathematical expressions. These ideas formulated in the language of mathematics can be found in the Appendix A together with the equations used for the quantitative predictions. The terminology of the model is summarized in Table 1.

Trabecular bone at a certain point in time is composed of many bone packets, which were deposited at different times and therefore differ from each other in their age. A difference in age corresponds to a difference in the mineral content of the bone packet. The connection between age and mineral content is given by the mineralization law (Fig. 2A). The well-known result that the mineral content in each individual bone packet increases with time due to the mineralization process is reflected by the mineralization law being an increasing function. From a "static" snapshot of trabecular bone, the BMDD is determined by looking how frequent a specific mineral content occurs in the patchwork formed by the bone packets.

The decisive step is now to go beyond this static description of trabecular bone by including the dynamical processes of mineralization and remodeling. As time elapses, the age of each individual bone packet increases. The increase of the mineral content due to the mineralization process is again given by the mineralization law (Fig. 2A). The effect of the increasing mineral content in the corresponding BMDD representation (Fig. 2B) is a shift of a bar in the diagram corresponding to a specific mineral content (which can, for simplicity, be thought as representing a bone packet with this mineral content) to the right towards higher values of the mineral content. The velocity with which the bar moves in the BMDD diagram – we use the term mineralization velocity – is given by the slope of the mineralization law for the corresponding mineral content. For a non-linear mineralization law, the slope can vary significantly with mineral content. This means that the mineralization velocity of a given bone packet will not be constant resulting in a change in the shape of the BMDD. The overall effect of the mineralization process on the BMDD is therefore a shift of the BMDD to higher values of the mineral content with a concurrent shape change caused by the non-linearity of the mineralization law.

The effect of the remodeling process on the BMDD is easier to imagine. The removal of bone of a specific mineral content by the osteoclasts reduces the frequency of finding bone with this mineral content. Consequently, the resorption of bone lowers the BMDD curve (gray area in Fig. 2B). The osteoid deposited by the osteoblasts is unmineralized and therefore appears at the very left of the BMDD diagram, i.e., at zero mineral content (symbolic hatched gray bar in Fig. 2B).

Summarizing, the changes of the BMDD due to the mineralization can be seen as a "flow" from low to high values of the mineral content with an unchanged area under the curve corresponding to a constant bone volume. The effect of remodeling on the BMDD is that while flowing to the right towards higher Ca values, some bone volume is lost due to some "leakage" to the flow (osteoclast action). Additionally the flow is fed from the very left (osteoblast action). Such "flow problems" are common in physics and can be mathematically described by a continuity equation [30,31]. The derivation of the corresponding partial differential equation (Eqs. (A4) and (A5)) can be found in the Appendix A, here we prefer the following symbolic notation:

$$\begin{aligned}&\{\text{total temporal change of the BMDD}\}\\&\quad=\left\{\begin{array}{l}\text{increase in the mineral content}\\ \text{according to mineralization law}\end{array}\right\}\\&\qquad-\{\text{OC action : lowering of the BMDD}\}\\&\qquad+\{\text{OB action : adding at zero mineral content}\}.\end{aligned}$$

To predict the time evolution of the BMDD, only three quantities have to be known. First the mineralization law, which may have a different form for healthy or diseased individuals. For instance, osteomalacia is characterized by both mineralization defects and hypomineralization, while osteogenesis imperfecta is connected to hypermineralization [32,33]. Although we investigate the effect of different mineralization laws, we assume for simplicity that once a mineralization law was chosen it remains fixed and does not change during lifetime. Second, the bone deposition rate characterizing the

Table 1
Description of important quantities of the model together with their units and symbols

Symbol	Quantity	Description	Unit
t	Time	Independent variable	[days] or [years]
τ	Time in units of the turnover time t_{TO}	Independent variable	Dimensionless
c	Mineral content, Ca content	Independent variable	[wt% Ca]
c_{max}	Maximal mineral content	Fixed value $c_{max} \approx 56$ vol% Ca ≈ 30 wt% Ca	[wt% Ca]
BV(t)	Bone volume	Function of time, can be derived from osteoblast and osteoclast actions	[μm^3]
$\rho(c,t)$	Bone mineralization density distribution (BMDD)	Describes the frequency of finding bone with a specified mineral content at a given time—function of mineral content and time	[μm^3/wt% Ca]
$\rho(c)$	Steady-state BMDD	Solution of the time-independent equation (B1)—function of the mineral content only	[μm^3/wt% Ca]
$c(t)$	Mineralization law	Describes how the mineral content in a newly deposited bone matrix changes as a function of time	[wt% Ca]
$v(c) \equiv \frac{dc}{dt}$	Mineralization velocity	Derived differentiating the mineralization law	[wt% Ca/day]
$j_{OB}(t)$	Bone deposition rate	Describes osteoblast action—only a function of time	[μm^3/day]
$\omega_{OC}(c,t)$	Bone resorption preference rate	Describes osteoclast action—function of both mineral content and time	[1/day]

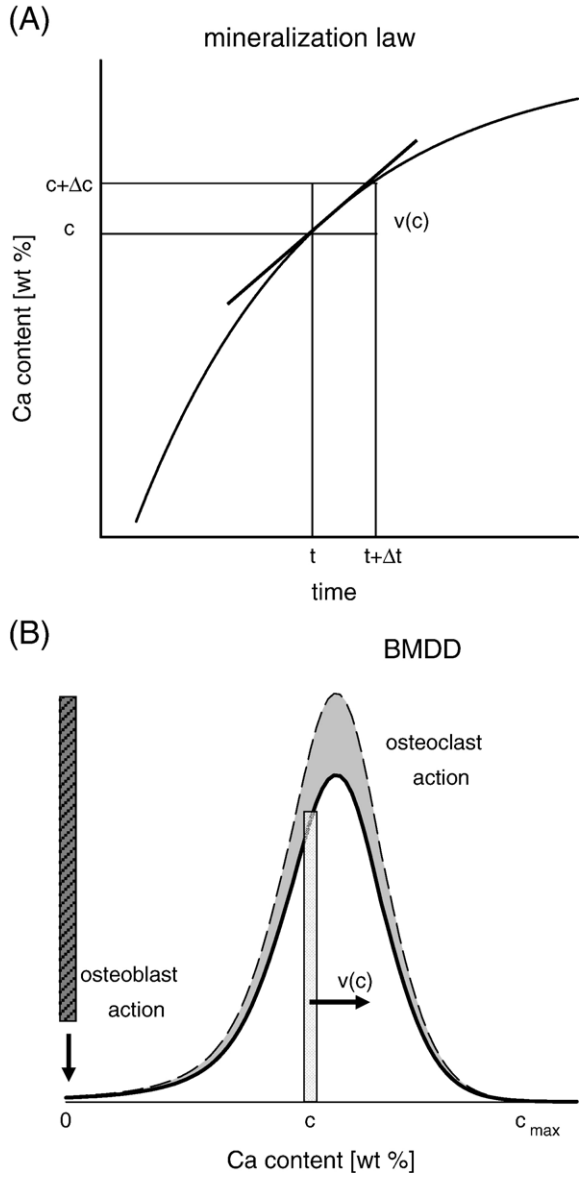

Fig. 2. (A) The mineralization law connects the age of a bone packet with its mineral content and describes how the mineral content changes with time according to the mineralization velocity, defined as the slope of the mineralization law for the corresponding mineral content. (B) Effect of remodeling and mineralization on the BMDD curve. By resorbing bone, the osteoclasts lower the curve (removed gray area) whereas the osteoblasts deposit unmineralized bone matrix (symbolized by the hatched gray bar at the very left of the diagram). Mineralization causes each bar in the BMDD histogram to move with a different mineralization velocity v dependent on the mineral content (see A). This results in a general shift of the BMDD from lower to higher mineral content. In doing so the shape of the curve may change, but the area under the curve remains constant.

osteoblast action. In general the deposition rate depends on time, since it can increase, for example, after administration of PTH [9]. Third, the bone resorption preference rate characterizing the osteoclast action. It was argued that osteoclasts could resorb preferentially mechanically damaged bone [34,35], which should be on average older and therefore be more highly mineralized. Likewise, it can be argued that osteoclasts resorb preferentially younger bone since they are more likely to encounter younger bone at the bone/marrow interface. To take into account this possible preference of resorption, the bone resorption preference rate depends on both time and mineral content. These two model parameters characterizing the remodeling process are directly related to measurable quantities of bone histomorphometry, bone formation rate (BFR/BV) and bone resorption rate (BRs.R/BV) (see Appendix A). The bone volume can be derived from the deposition and resorption rates of the bone cells and is therefore not an independent model parameter.

The computed BMDD is a function which depends on both independent variables, mineral content and time. The value of the mineral content can vary between 0 – corresponding to unmineralized bone (osteoid) – and a maximum value, which can be estimated based on the available volume to be about 56 vol % [1], i.e., close to 30 wt%. The total area under the computed BMDD curve corresponds to the bone volume. Following the definitions in [23], the shape of the BMDD is characterized by three quantities (Fig. 1B). The most frequent Ca content, i.e., the position of the peak, is denoted by Ca_{Peak}. The mean Ca content, Ca_{Mean}, is defined as first moment of the BMDD, i.e., the "center of gravity" of the curve. Beside the bone volume, it is the main contributor to the bone mineral density (BMD) as obtained by DXA measurements. The peak width of the BMDD, Ca_{Width}, is defined as full-width at half maximum (FWHM).

Experimental evidence for an almost constant BMDD and the steady-state assumption

For healthy adult individuals, it was shown that the BMDD is almost independent of sex, ethnicity, skeletal site and in particular of age, therefore defining a reference BMDD [18,23]. In the framework of our model this means that despite the ongoing mineralization and remodeling process, this reference BMDD remains unchanged. This experimental observation can be exploited to simplify the mathematical Eqs. (A4) and (A5) (Appendix A) for the time evolution of the BMDD. Under the assumption that the solution for the BMDD should not change with time (steady-state assumption), Eq. (A4) can be solved analytically. The result consists of two transformation formulas (Eqs. (B3) and (B5), Appendix B), which connect the mineralization law with the steady-state BMDD, which is now a function of the mineral content alone. The steady-state assumption implies that the bone volume also remains constant with time. The results that we present later on, nevertheless, remain valid as long as the change in bone mass occurs on a longer time scale than shape changes in the BMDD. This allows the discussion of the shape of the BMDD also in cases of age-related loss in bone mass. The transformation formulas connecting the mineralization law and the BMDD (Eqs. (B3) and (B5), Appendix B) further simplify under the assumption that the osteoclasts resorb bone independent of its mineral content (Eqs. (B6) and (B7), Appendix B). The steady-state assumption leads further to a reduction of the number of quantities that have to be known to predict the BMDD. Instead of the bone deposition rate and the bone resorption preference rate,

a single parameter, namely the turnover time, t_{TO}, is sufficient to characterize the remodeling process. The turnover time is defined as the time it takes to remodel an amount of bone equal to the actual bone volume. A high turnover situation corresponds to a short turnover time, while low turnover is characterized by a long turnover time. With measuring time in units of the turnover time, i.e., introducing the time variable $\tau \equiv t/t_{TO}$, the simulation results can be presented in a form independent of the remodeling process. Where it is of interest to transform simulation time in real physical time, we chose $t_{TO}=5$ years, a value reported for healthy adult humans [36].

Results

The relationship between the mineralization law and the BMDD, which is mathematically summarized in Eqs. (B6) and (B7) (Appendix B), will be exploited demonstrating the importance of the BMDD as a fingerprint of the mineralization kinetics. We start by demonstrating how different mineralization laws influence the shape of the resulting steady-state BMDD. In the next step we solve the "inverse" problem, i.e., starting from the experimental data of the reference BMDD we derive the underlying mineralization law for healthy humans. Eventually, using this mineralization law for healthy humans, we can predict the influence of different turnover rates on the BMDD.

Effect of mineralization law

Due to experimental difficulties in determining the increase of the mineral content in a bone packet as a function of time, no mineralization law has been quantitatively proposed in the bone literature both for healthy humans and for patients with disorders in the mineralization process. To gain a better understanding of the effect of the mineralization law on the resulting shape of the BMDD, we chose simple, hypothetical mineralization laws and then calculated the corresponding BMDDs using Eq. (B6) (Appendix B). In Table 2, the results are summarized in mathematical and graphical form, where Fig. 3 allows a quantitative comparison between the predicted BMDDs and the measured peak-shaped reference BMDD.

Since mineralization is described as a continuing increase in the mineral content leveling off at a maximum value of Ca content, a simple but instructive choice for the mineralization law is an exponential function. The exponential growth law is then characterized completely by the maximum Ca content attainable and by a single time constant, $\tau_{MI}=t_{MI}/t_{TO}$, which describes how fast the mineralization process proceed (Table 2 and Fig. 3A). With this choice of mineralization law the resulting BMDD is a power function (Table 2 and Fig. 3B). Depending on how the time constant which characterizes the mineralization process, t_{MI}, relates to the turnover time of the remodeling process, two different behaviors of the BMDD can be distinguished. In the case where remodeling is faster than the mineralization process ($t_{MI}>t_{TO}$, or equivalently, $\tau_{MI}>1$), the resulting BMDD is a monotonously decreasing function (light gray in Fig. 3B). The opposite case of a faster mineralization process than remodeling ($t_{MI}<t_{TO}$, or equivalently, $\tau_{MI}<1$) leads to a monotonously increasing BMDD (dark gray in Fig. 3B). The special case $\tau_{MI}=1$ corresponds to a constant BMDD, i.e., in this case bone is present with equal probability independent of the mineral content. It is important to note that for any choice of the time constant for the mineralization, the result is always a monotonous, and not a peak-shaped BMDD.

In bone literature the mineralization kinetics is qualitatively described as a two-step process with a fast primary and a much slower secondary phase. As proposed in the literature [15], we chose to model the mineralization law with two linear functions characterized by two slopes and an intersection point (Table 2 and Fig. 3A). The resulting BMDD is composed of two exponentially decaying functions (Table 2 and Fig. 3B) with a kink at a mineral content corresponding to the change in slopes in the mineralization law. Again, independent of the chosen parameters, the resulting BMDD does not display a peak like the measured reference BMDD.

Since a single exponential function with one time constant is insufficient in producing a peak-shaped BMDD, a natural refinement is to propose a mineralization law as a sum of two exponential functions with two different time constants. Assuming one time constant, τ_1, larger than 1 and the other, τ_2, smaller than 1, the resulting BMDD displays a peak (Fig. 3B, black dashed line). Trying to choose the time constants in such a way that the resulting BMDD fits the measured reference BMDD, however, is not feasible. Compared to the peak width of the reference BMDD, the width of the calculated BMDD is always smaller indicating a more homogeneous mineralization than found in real bone.

A reasonable agreement with the reference BMDD is obtained using a mineralization law consisting of a sum of two hyperbolic growth functions as defined in Table 2. The ratio between the two time constants obtained from the fit is larger than 1500. The resulting fit function (gray line in Fig. 4A) is almost over the whole range of mineral content within the uncertainty of the measurement of the reference BMDD, as defined by the standard deviation.

The mineralization law of healthy adult humans

Up to now we followed the more intuitive approach of choosing a mineralization law, calculating the resulting BMDD and then comparing the result with the measured reference BMDD (Fig. 3). Being interested in the mineralization law that results exactly in the reference BMDD, there is no need to proceed with guessing adequate mineralization laws. Instead Eq. (B6) (Appendix B) can be used which allows a back transformation of the BMDD to the underlying mineralization law. Since Eq. (B6) (Appendix B) defines a non-linear transformation, it is important to start from the raw data which was used to define the reference BMDD. The input data were the BMDDs of 52 samples, both autopsies and biopsies, of healthy adult humans having different age, sex, ethnicity and skeletal site analyzed in reference [23]. Each data set consisted of 174 equidistant data points within Ca content between 0 and 30 wt%.

Table 2
Four different hypothetical mineralization laws and the corresponding BMDD

Mineralization law		Resulting BMDD	
Exponential growth with one time constant τ_{MI}: $c(\tau) = c_{max}\,(1 - \exp(-\tau/\tau_{MI}))$	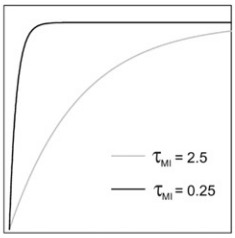	Power law function for the corresponding BMDD: $\frac{\rho(c)}{BV} = \frac{\tau_{MI}}{c_{max}}\left(1 - \frac{c}{c_{max}}\right)^{(\tau_{MI}-1)}$	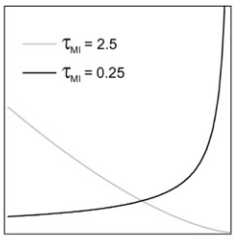
Double linear: $c(\tau) = \begin{cases} c_1\tau & \tau \le \overline{\tau} \\ c_2\tau + (c_1 - c_2)\,\overline{\tau} & \tau > \overline{\tau} \end{cases}$	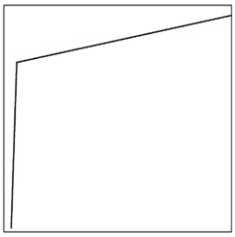	Double exponential decay function: $\frac{\rho(c)}{BV} = \begin{cases} \frac{1}{c_1}\exp(-c/c_1) & c \le c(\overline{\tau}) \\ \frac{1}{c_2}\exp(-\frac{c}{c_2} + \frac{c_1 - c_2}{c_2}\overline{\tau}) & c > c(\overline{\tau}) \end{cases}$	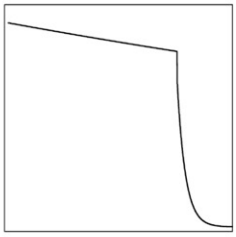
Sum of two exponentials with time constants τ_1 and τ_2 $c(\tau) = c_1(1 - \exp(-\tau/\tau_1)) + (c_{max} - c_1)(1 - \exp(-\tau/\tau_2))$	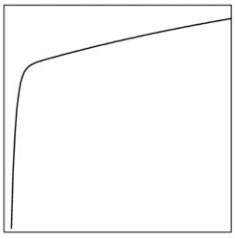	Analytical expression not available since the mineralization law $c(\tau)$ cannot be inverted into a function $\tau(c)$. The BMDD is therefore computed numerically.	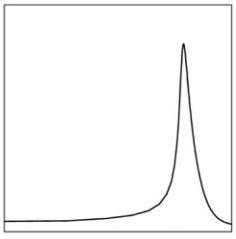
Sum of two hyperbolic growth functions with two time constants τ_1 and τ_2: $c(\tau) = c_1\frac{\tau/\tau_1}{1 + \tau/\tau_1} + c_2\frac{\tau/\tau_2}{1 + \tau/\tau_2}$	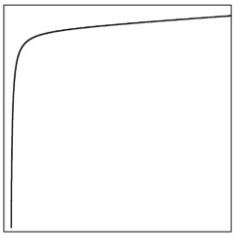	$\frac{\rho(c)}{BV} = \left[\frac{\Delta_2 - \Delta_3}{2\Delta_1^2} + \frac{(\Delta_2 - \Delta_3)(\tau_1 + \tau_2) - 2\tau_1\tau_2(\Delta_1 + c)}{2\Delta_1\Delta_3}\right] \exp\left[-\frac{\Delta_2 - \Delta_3}{2\Delta_1}\right]$ with: $\Delta_1 = c - c_1 + c_2$ $\Delta_2 = c(\tau_1 + \tau_2) - c_1\tau_2 + c_2\tau_1$ $\Delta_3 = \sqrt{\Delta_2^2 - 4c\Delta_1\tau_1\tau_2}$	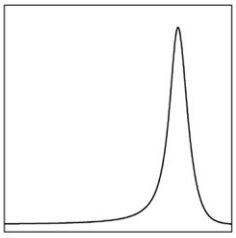

Fig. 4A shows the average BMDD of this data, which defines the reference BMDD for healthy adult humans, together with its standard deviation. Using Eq. (B6) (Appendix B) the mineralization law for each of the 52 BMDDs was calculated separately. The results were then averaged resulting in a mineralization law of healthy adult humans and its standard deviation describing the increase in the mineral content in a bone packet over several decades in time (Fig. 4B, note the logarithmic time scale of the insert). Since the input data are only numerical data, the resultant mineralization law is not an analytical mathematical function. In the previous section, however, it was shown that a sum of two hyperbolic functions gives a reasonable fit to the numerically calculated mineralization law. According to the obtained law, mineralization proceeds extremely fast up to a value of about 18 wt% Ca. After this initial mineralization surge, a smooth transition follows, which leads for later times to an approximately linear increase in the mineralization as a function of time. The slope in this regime is about three orders of magnitude smaller than for the initial part of the mineralization law.

Effect of turnover rate

The mineralization law obtained for healthy humans (Fig. 4B) was used to investigate the effect of changes in the remodeling process on the form of the BMDD. With the help of Eq. (B7) (Appendix B), the BMDD as a result of different values for the turnover rate can be predicted. The effect of a higher turnover rate is a shift of the peak to values of lower mineralization, while a reduced turnover results in a shift to

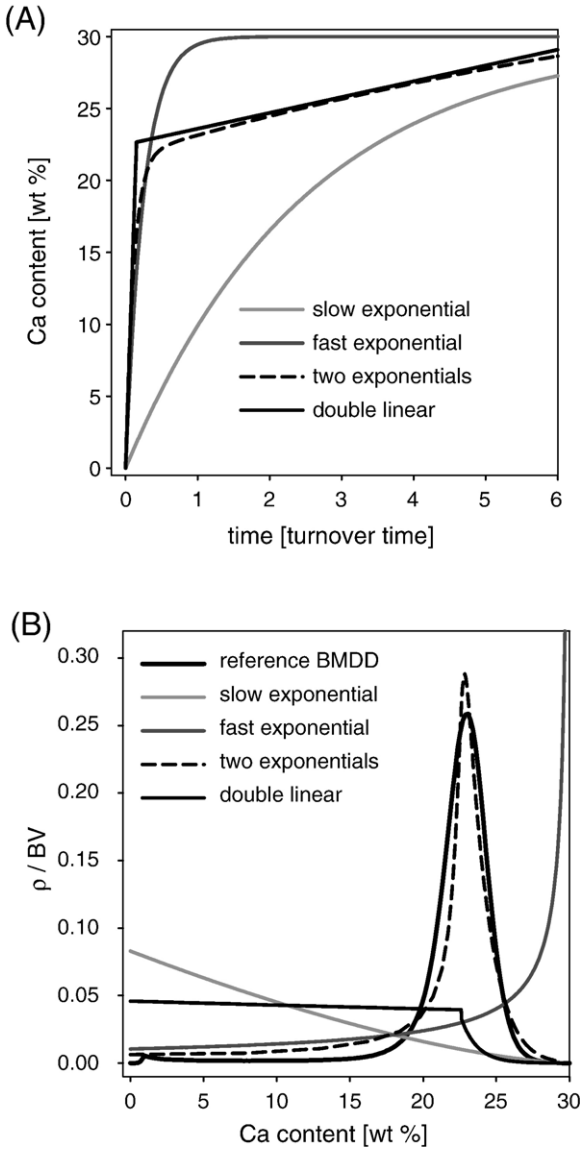

Fig. 3. (A) Different hypothetical functions to describe the mineralization law: Exponential growth with one slow time constant ($\tau_{MI}=5$) or one fast time constant ($\tau_{MI}=0.25$); double linear function and sum of two exponentials with two time constants ($\tau_1=9$ and $\tau_2=0.09$). (B) Comparison between the reference BMDD and the simulated BMDDs considering the mineralization laws defined in (A).

the right (dark and light gray line in Fig. 5, respectively). The shift of the peak position is also reflected in the monotonously increasing function of Ca_{Peak} plotted in Fig. 6. While in the considered interval of the turnover time with respect to the healthy turnover time between 0.1 and 4, Ca_{Peak} increases only by a factor of 1.19, the mean Ca content Ca_{Mean} increases by a factor 1.56. This discrepancy of the behavior of Ca_{Peak} and Ca_{Mean} is due to the change in the shape of the BMDD as characterized by the width of the peak, Ca_{Width}, and its asymmetry. The most homogeneous mineralization distribution, i.e., a minimum value for Ca_{Width}, is obtained when the turnover is sped up by a factor of about 4. Both a further increase and decrease of the turnover lead to a broadening of the BMDD. The asymmetry of the BMDD changes from a prevailing part at the left side of the peak for high turnover, to a leaning to the right in low turnover situations.

Discussion

The bone mineralization density distribution (BMDD) is a standard quantity to describe the heterogeneous mineral content of bone as a result of the remodeling and the mineralization process. In the present work, we developed a mathematical model to extract from the BMDD information about the

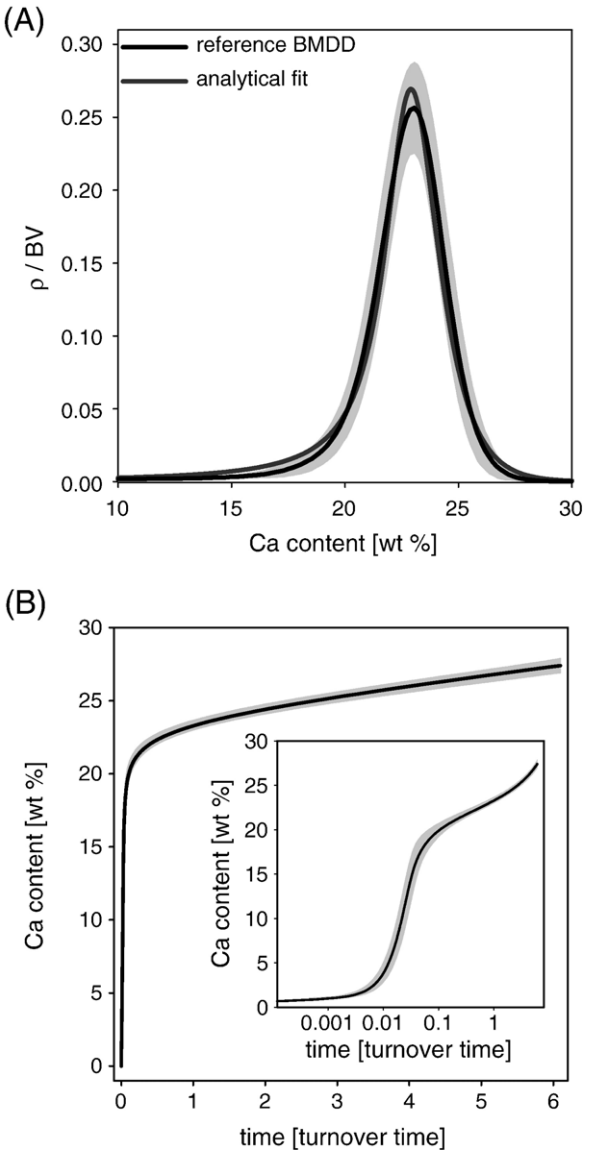

Fig. 4. (A) Measured reference BMDD: the black line shows the curve obtained averaging 52 BMDDs from healthy adult humans with the standard deviation boundaries (gray area). The gray line denotes the analytical fitting using a sum of two hyperbolic functions for the mineralization law (Table 2). (B) The corresponding calculated mineralization law: the black line shows the derived mineralization law together with its standard deviation. In a semi-logarithmic plot (insert) the biphasic nature of the mineralization law is evident.

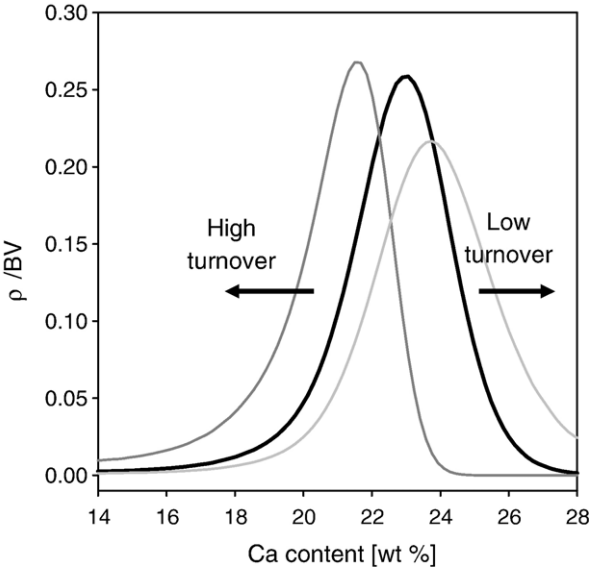

Fig. 5. Effect of different turnover times keeping the same mineralization law: the solid black line denotes the reference BMDD, the dark gray line presents a high turnover situation (4 times increased turnover with respect to the normal turnover time) and the light gray line is the result of a 2 times reduced turnover. In both cases a constant bone volume and a steady state condition for BMDD is assumed.

mineralization process in trabecular bone. Two main assumptions deserve a more detailed discussion.

Accuracy of the reference BMDD

The accuracy of the theoretical result is limited by the experimental accuracy determining the BMDD. The effects of counting statistics inherent in the stochastic process of electron emission, backscattering and detection cause a broadening of the true distribution [37]. Furthermore the frequency of appearance of bone in the concentration range below 10 wt% Ca and close to 30 wt% Ca is extremely small and therefore relative measurement errors are large. These regimes of very low and very high Ca content correspond to times in the mineralization process approximately less than 1 week and more than 30 years after the start of the process, respectively. The plots in this paper show results only in this limited interval of the Ca content. The cement lines separating bone packets are not excluded from the BMDD and will preferentially make additional contributions to the high Ca content range of the BMDD. In addition, the fast primary mineralization should give rise to a sharp gradient of the mineral content around the mineralization front of a forming bone packet. The spatial resolution of the qBEI measurements of 4 μm × 4 μm could lead to some averaging over this mineralization front. As a consequence the initial slope of the obtained mineralization law at very early times might underestimate the real slope.

Steady-state assumption

The relation between the mineralization law and the BMDD as described by Eqs. (B6) and (B7) (Appendix B) is only valid if the BMDD has reached its steady state configuration. Our reference BMDD for healthy adult trabecular bone based on previous qBEI measurements [18, 23] is very likely to fulfill this criterion because samples in the age range from 25 to 95 years did not show a significant change in the shape of the BMDD. Although there is no data of the bone volume available, it can be assumed that the bone volume is reduced corresponding to age-related bone loss. Since the area under the experimentally obtained BMDD is always normalized to 100%, changes in the bone volume are not reflected in the BMDD. This observation of an unchanged shape of the BMDD despite a loss of bone volume indicates that shape changes of the BMDD occur on a faster time scale than the bone loss so that the BMDD is always in "shape equilibrium". With this assumption our calculations are applicable also for scenarios where the bone volume is not constant but undergoes a slow decrease or increase. Nevertheless, the validity of the approach, e.g., the resulting mineralization law of healthy humans (Fig. 4B) is surely limited to time scales in the order of

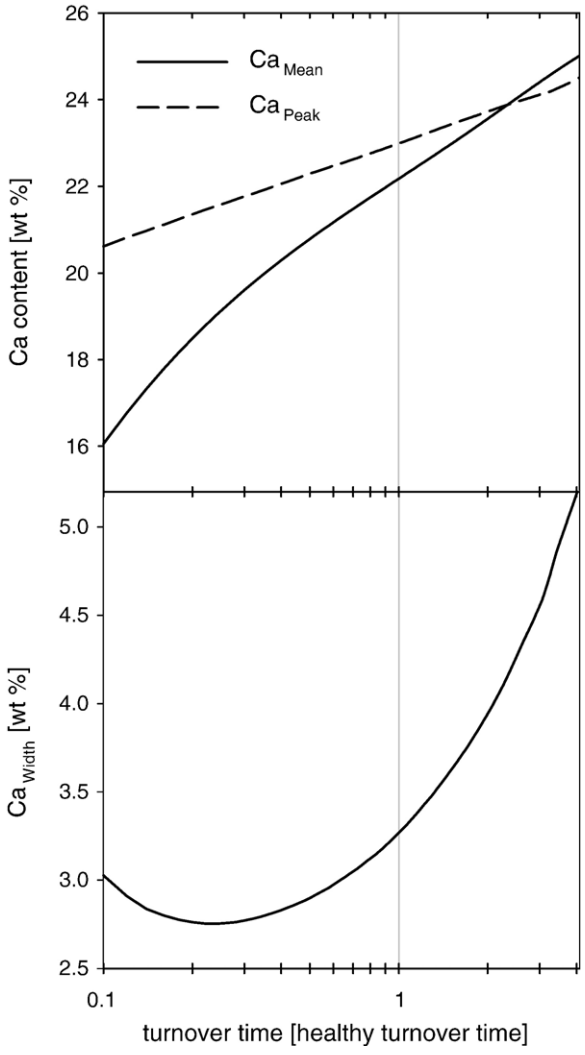

Fig. 6. Most frequent calcium content (Ca_{Peak}), mean calcium content (Ca_{Mean}) and full-width at half maximum of the peak (Ca_{Width}) plotted against different turnover times. The turnover times are normalized by the healthy turnover time, which corresponds to the turnover of the reference BMDD (i.e., 0.1 refers to a 10 times increased turnover).

about 30 years. This is further underlined by the increasing error bars with time.

Under these assumptions, the three main results are as follows:

(1) the peak-shaped BMDD reveals the biphasic nature of the mineralization law.

With our example of a hypothetical exponential mineralization law, which includes only a single time constant, we showed that the resulting BMDD is in obvious contradiction to the measured BMDD (Fig. 3B). The example demonstrates the "competition" between the mineralization and the remodeling process. In the case that remodeling proceeds faster than mineralization ($\tau_{MI}>1$), deposited bone packets do not have enough time to mineralize before they are remodeled again and the maximum value of the BMDD is therefore at zero mineral content. Conversely, in the case where mineralization is more efficient and the remodeling "lags behind" ($\tau_{MI}<1$) the majority of bone attains the maximum mineral content c_{max} and the BMDD is monotonously increasing. The peak-shaped form of the reference BMDD of healthy adults is consistent with the existence of more than one time regime in the mineralization process. In the first time regime, the mineralization process dominates, which leads to an increase in the amount of not yet fully mineralized bone. Conversely when the mineralization process slows down significantly and drops behind the remodeling process, the amount of higher mineralized bone starts to decrease due to bone resorption causing a peak in the BMDD. According to the viewpoint of Fig. 2, the mineralization process changes the BMDD since bone packets shift in the diagram from low to high mineral content. The velocity of this shift depends on the mineral content within each bone packet. Our mineralization law predicts a strong reduction in the mineralization velocity at about 18 wt% Ca. This reduction leads to a kind of "traffic jam" of the moving bone packets in the diagram, with the result that the different bone packets "pile up" giving rise to a peak in the BMDD. Following this line of argument, we conclude that the more rapid the reduction in the mineralization velocity, the sharper becomes the peak of the BMDD.

(2) Prediction of a mineralization law for healthy humans based on an experimentally obtained reference BMDD.

The mineralization law of healthy human adults that we obtained consists of a rapid primary phase that increases the mineral content up to about 18 wt% Ca and a much slower increase afterwards lasting years. This prediction agrees well with what was concluded by observations from standard tetracycline labeling technique combined with qBEI [12]. Nevertheless, systematic labeling experiments combined with Ca content measurements over a larger time range up to months and years are still lacking and will be interfered by the remodeling process. The prediction of the mineralization law of Fig. 4B describes the mineralization process over a time period of several years. Although it seems that a double linear mineralization law [15] gives a reasonable description of the mineralization process, our analysis demonstrates that the resulting BMDD is then far-off from the reference BMDD. The BMDD seems to be a much more sensitive instrument to learn about the mineralization kinetics than generally assumed.

(3) Quantitative prediction of the influence of changes in the turnover on the BMDD.

Beside a full prediction of the shape of the BMDD (Fig. 5), the most important result is the strong dependence of the mean Ca content on the bone turnover. The mineral content shifts to higher levels at reduced turnover and to lower levels at higher turnover (Fig. 6, top). Antiresorptive therapies using bisphosphonates are known to significantly reduce turnover [26, 27], while several bone diseases, most prominent osteoporosis, are associated with increased turnover [24]. Our simulation results are in good agreement with the experimentally measured BMDD in such patients, who show increased mean mineral content for antiresorptive treatment and decreased mean mineral content when turnover is increased [24,27–29,38]. This relation of bone turnover and mean Ca content has clinical relevance, when bone mineral density (BMD) as measured by DXA is used for diagnosis and evaluation of treatment efficacy in osteoporosis. The resulting BMD includes combined information about the bone volume as well as the mean mineral content (Ca_{Mean}). Our calculations show that a five-fold increase in the turnover would lead to a reduction of the BMD by 16.6% at constant bone volume. Thus, the interpretation of BMD in terms of bone loss or increase has to be done with caution.

Considering the peak width in a low turnover situation, our model predicts a broadening. At a first glance, this is in contradiction to measurements made after bisphosphonate treatment, which show a narrowing of the BMDD. However, experimental measurements and simulation consider different situations. While the changes in BMDD were measured already after 2 and 3 years of bisphosphonate administration, our model calculations predict the shape of the BMDD for a reduced turnover of constant value (steady state condition). An agreement can therefore be expected only for late times after a change in the turnover. Recently, measurements of the effect of risedronate showed a narrowing after 3 years, followed by a broadening and a return to normal peak width to baseline level after 5 years [28,29]. An example of a high turnover situation is anabolic treatment with intermittent PTH with increased peak width, Ca_{Width}, as measured by qBEI, which showed a strong positive correlation with the bone formation rate (BFR/BS) as determined histomorphometrically [9]. Again, it seems that this is not in agreement with the predictions of the model. However, it has to be taken into account that in this case the bone volume changes fast in time. Dynamic simulations solving Eqs. (A4) and (A5) (Appendix A) numerically would be necessary to allow a closer comparison between experimental measurements and simulations since they are able to predict the full-time evolution of the BMDD after changes in the remodeling or in the mineralization process.

In conclusion, the measured BMDD of human adult trabecular bone is approximately in a steady state condition and therefore reflects presumably an evolutionary optimum distribution with respect to material quality and bone strength. Hence, any deviations from this optimal distribution might deteriorate the mechanical performance of the bone. The described simulation of the BMDD gives us new insight in the mechanism how such a fingerprint of bone mineralization is

generated and how changes can be induced by diseases and treatments. New possibilities of analysis of BMDDs measured on various bone biopsies are opened and predictions can be made on the BMDD shape after certain treatments. This is of important clinical interest, especially when a patients' BMDD should be corrected towards normal BMDD. Answering the question whether changes in BMDD have to be attributed to a change in the turnover rate or are due to a disordered mineralization process will help to tailor treatment regimes of higher efficiency.

Acknowledgments

DR is supported by the EU Marie Curie EST Program on Biomimetic Systems, MEST-CT-2004-504465.

Appendix A. Time evolution equation for the BMDD $\rho(c,t)$

The bone volume having a mineral content between c_1 and c_2 at a particular time t is given by

$$\int_{c_1}^{c_2} \rho(c,t)\mathrm{d}c. \tag{A1}$$

After an infinitesimal time Δt this bone volume changes by $\Delta\rho$ due to the following contributions:

(1) As bone mineralizes, a volume element of bone with a mineral content initially below c_1 enters our observation interval $[c_1, c_2]$. Its volume is $\rho(c_1,t)v(c_1)\Delta t$ because $v(c_1)\Delta t$ corresponds to the change in the mineral content obtained in Δt.

(2) Similarly, the bone volume leaving our observation interval $[c_1, c_2]$ is $-\rho(c_2,t)v(c_2)\Delta t$.

(3) The resorbed bone volume by the osteoclasts in the interval $[c_1, c_2]$ of the mineral content is assumed to be proportional to the available bone volume (Eq. (A1)). To account for a possible preference of the osteoclasts to resorb, for instance, high mineralized bone, we introduce the bone resorption preference rate, so that the resorbed bone volume in $[c_1, c_2]$ amounts to

$$-\int_{c_1}^{c_2} \omega_{\mathrm{OC}}(c,t)\rho(c,t)\mathrm{d}c\Delta t. \tag{A2}$$

Therefore, the total change $\Delta\rho$ as the sum of these contributions equals

$$\Delta\rho = \rho(c_1,t)v(c_1)\Delta t - \rho(c_2,t)v(c_2)\Delta t - \int_{c_1}^{c_2} \omega_{\mathrm{OC}}(c,t)\rho(c,t)\mathrm{d}c\Delta t. \tag{A3}$$

Using $\rho(c_1,t)v(c_1) - \rho(c_2,t)v(c_2) = -\int_{c_1}^{c_2} \frac{\partial(\rho v)}{\partial c}\mathrm{d}c$ and dividing by Δt, in the limit $\Delta t \to 0$ with $\frac{\Delta\rho}{\Delta t} = \int_{c_1}^{c_2} \frac{\partial\rho}{\partial t}\mathrm{d}c$ leads to the following partial differential equation

$$\underbrace{\frac{\partial\rho}{\partial t}(c,t)}_{\text{total temporal change}} = \underbrace{-\frac{\partial}{\partial c}[\rho(c,t)v(c)]}_{\text{change due to mineralization process}} - \underbrace{\omega_{\mathrm{OC}}(c,t)\rho(c,t)}_{\text{bone resorption due to osteoclasts}}. \tag{A4}$$

(4) The deposition of unmineralized bone by the osteoblasts is modeled by the boundary condition at $c=0$. Since the bone deposition rate $j_{\mathrm{OB}}(t)$ is defined as bone volume deposited per time unit, the bone volume deposited during Δt equals $j_{\mathrm{OB}}(t)\Delta t$. Following the argument given in (1) results in a boundary condition for ρ at $c=0$:

$$\rho(c=0,t)v(c=0) = j_{\mathrm{OB}}(t). \tag{A5}$$

A different way to write the balance in bone volume between resorption and deposition is that the sum of the resorbed and the deposited bone volume has to be equal to the total change in bone volume, i.e.,

$$-\int_0^{c_{\max}} \omega_{\mathrm{OC}}(c,t)\rho(c,t)\mathrm{d}c + j_{\mathrm{OB}} = \frac{\mathrm{dBV}}{\mathrm{d}t}. \tag{A6}$$

Standard bone histomorphometric parameters for the osteoblast and osteoclast action are the bone formation rate (BFR/BV) defined as the percentage of bone formed per year, and the bone resorption rate (BRs.R/BV) defined as the percentage of bone resorbed per year. Since both parameters refer to the duration of 1 year, we have to perform an integration over 1 year of our instantaneously defined quantities to obtain the relationships between model parameters and parameters of bone histomorphometry:

$$\mathrm{BFR/BV} = \int_0^{1\,\mathrm{year}} \frac{j_{\mathrm{OB}}(t)}{\mathrm{BV}(t)}\mathrm{d}t \tag{A7}$$

$$\mathrm{BRs.R/BV} = \int_0^{1\,\mathrm{year}} \int_0^{c_{\max}} \frac{\omega_{\mathrm{OC}}(c,t)\rho(c,t)\mathrm{d}c}{\mathrm{BV}(t)}\mathrm{d}t. \tag{A8}$$

Appendix B. Steady state solution

Under the steady state assumption all the time dependencies are removed, i.e., $\rho(c,t)$ and $\omega_{\mathrm{OC}}(c,t)$ become functions only of mineral content: $\rho(c)$ and $\omega_{\mathrm{OC}}(c)$. Eq. (A4) and its boundary condition (Eq. (A5)) become also time independent and simplify to

$$\begin{cases} \frac{\mathrm{d}}{\mathrm{d}c}[\rho(c)v(c)] = -\omega_{\mathrm{OC}}(c)\rho(c) \\ \rho(c=0)v(c=0) = j_{\mathrm{OB}} \end{cases} \tag{B1}$$

This ordinary differential equation can be solved analytically to compute the mineralization law from a given mineralization distribution $\rho(c)$. The mineralization velocity reads as

$$v(c) = \frac{1}{\rho(c)}\left(\int_c^{c_{\max}} \omega_{\mathrm{OC}}(c')\rho(c')\mathrm{d}c'\right), \tag{B2}$$

and since $t(c) = \int_0^c \frac{\mathrm{d}c'}{v(c')}$, we find for the mineralization law expressed as $t(c)$,

$$t(c) = \int_0^c \frac{\rho(c')\mathrm{d}c'}{\int_{c'}^{c_{\max}} \omega_{\mathrm{OC}}(c'')\rho(c'')\mathrm{d}c''} \tag{B3}$$

For the inverse transformation, starting from a mineralization law, we obtain for the mineralization distribution,

$$\rho(c) = \frac{j_{OB}}{v(c)} \exp\left(- \int_0^c \frac{\omega_{OC}(c')}{v(c')} dc' \right), \quad \text{(B4)}$$

and with $v(c) = \frac{dc}{dt}(c)$ and using integration by parts leads to

$$\rho(c) = j_{OB} \frac{dt}{dc}(c) \exp(-\omega_{OC}(c) t(c)) \exp\left(- \int_0^c \frac{d\omega_{OC}}{dc'}(c') t(c') dc' \right). \quad \text{(B5)}$$

The BMDD depends on both, the mineralization law and a possible preference of bone resorption as a function of the mineral content. In the case discussed in the main text that ω_{OC} is a constant independent of c, $j_{OB} = \omega_{OC}$ BV, and with the dimensionless time parameter $\tau = \frac{t}{t_{TO}} = t \frac{j_{OB}}{BV}$, Eq. (B3) reduces to

$$\tau(c) = -\ln \int_c^{c_{max}} \frac{\rho(c')}{BV} dc', \quad \text{(B6)}$$

where the logarithm enters because Eq. (B3) is then an integral with the expression in the numerator equal to the derivative of the denominator. The reduction from Eq. (B5) to

$$\frac{\rho(c)}{BV} = -\frac{d}{dc} [\exp(-\tau(c))] \quad \text{(B7)}$$

is straightforward since the last exponential function on the right hand side of Eq. (B5) becomes equal to 1.

References

[1] Jager I, Fratzl P. Mineralized collagen fibrils: a mechanical model with a staggered arrangement of mineral particles. Biophys J 2000;79 (4):1737–46.

[2] Follet H, Boivin G, Rumelhart C, Meunier PJ. The degree of mineralization is a determinant of bone strength: a study on human calcanei. Bone 2004;34(5):783–9.

[3] van der Linden JC, Birkenhager-Frenkel DH, Verhaar JAN, Weinans H. Trabecular bone's mechanical properties are affected by its non-uniform mineral distribution. J Biomech 2001;34(12):1573–80.

[4] Currey JD. Bones: structure and mechanics. Princeton, NJ: Princeton Univ. Press; 2002. p. 436.

[5] Currey JD. Role of collagen and other organics in the mechanical properties of bone. Osteoporosis Int 2003;14:S29–36.

[6] Gao H, Ji B, Jager IL, Arzt E, Fratzl P. Materials become insensitive to flaws at nanoscale: lessons from nature. Proc Natl Acad Sci U S A 2003;100(10):5597–600.

[7] Eriksen EF, Axelrod DW, Melsen F. Bone histomorphometry. New York: Raven Press; 1994.

[8] Akkus O, Polyakova-Akkus A, Adar F, Schaffler MB. Aging of microstructural compartments in human compact bone. J Bone Miner Res 2003;18(6):1012–9.

[9] Misof BM, Roschger P, Cosman F, Kurland ES, Tesch W, Messmer P, et al. Effects of intermittent parathyroid hormone administration on bone mineralization density in iliac crest biopsies from patients with osteoporosis: a paired study before and after treatment. J Clin Endocrinol Metab 2003;88(3):1150–6.

[10] Parfitt AM. Osteonal and hemi-osteonal remodeling—The spatial and temporal framework for signal traffic in adult human bone. J Cell Biochem 1994;55(3):273–86.

[11] Jowsey J. Variations in bone mineralization with age and disease. In: Frost HM, editor. Bone biodynamics. Boston, MA: Little, Brown & Company; 1964. p. 461–79.

[12] Fratzl P, Gupta HS, Paschalis EP, Roschger P. Structure and mechanical quality of the collagen-mineral nano-composite in bone. J Mater Chem 2004;14(14):2115–23.

[13] Grynpas M. Age and disease-related changes in the mineral of bone. Calcif Tissue Int 1993;53:S57–64.

[14] Meunier PJ, Boivin G. Bone mineral density reflects bone mass but also the degree of mineralization of bone: therapeutic implications. Bone 1997;21(5):373–7.

[15] Boivin G, Meunier PJ. Methodological considerations in measurement of bone mineral content. Osteoporosis Int 2003;14:S22–7.

[16] Boivin G, Meunier PJ. The degree of mineralization of bone tissue measured by computerized quantitative contact microradiography. Calcif Tissue Int 2002;70(6):503–11.

[17] Skedros JG, Bloebaum RD, Bachus KN, Boyce TM, Constantz B. Influence of mineral-content and composition on graylevels in back-scattered electron images of bone. J Biomed Mater Res 1993;27(1):57–64.

[18] Roschger P, Fratzl P, Eschberger J, Klaushofer K. Validation of quantitative backscattered electron imaging for the measurement of mineral density distribution in human bone biopsies. Bone 1998;23 (4):319–26.

[19] Boyde A, Elliott JC, Jones SJ. Stereology and histogram analysis of backscattered electron images—Age-changes in bone. Bone 1993;14 (3):205–10.

[20] Roschger P, Plenk H, Klaushofer K, Eschberger J. A new scanning electron-microscopy approach to the quantification of bone-mineral distribution—backscattered electron image grey-levels correlated to calcium k-alpha-line intensities. Scanning Microsc 1995;9(1):75–88.

[21] Nuzzo S, Lafage-Proust MH, Martin-Badosa E, Boivin G, Thomas T, Alexandre C, et al. Synchrotron radiation microtomography allows the analysis of three-dimensional microarchitecture and degree of mineralization of human iliac crest biopsy specimens: effects of etidronate treatment. J Bone Miner Res 2002;17(8):1372–82.

[22] Bachus KN, Bloebaum RD. Projection effect errors in biomaterials and bone research. Cells Mater 1992;2(4):347–55.

[23] Roschger P, Gupta HS, Berzlanovich A, Ittner G, Dempster DW, Fratzl P, et al. Constant mineralization density distribution in cancellous human bone. Bone 2003;32(3):316–23.

[24] Roschger P, Grabner BM, Messmer P, Dempster DW, Cosman F, Nieves J, et al. Influence of intermittent PTH treatment on mineral distribution in the human ilium: a paired biopsy study before and after treatment. J Bone Miner Res 2001;16:S179.

[25] Camacho NP, Rinnerthaler S, Paschalis EP, Mendelsohn R, Boskey AL, Fratzl P. Complementary information on bone ultrastructure from scanning small angle X-ray scattering and Fourier-transform infrared microspectroscopy. Bone 1999;25(3):287–93.

[26] Roschger P, Fratzl P, Klaushofer K, Rodan G. Mineralization of cancellous bone after alendronate and sodium fluoride treatment: a quantitative backscattered electron imaging study on minipig ribs. Bone 1997;20 (5):393–7.

[27] Roschger P, Rinnerthaler S, Yates J, Rodan GA, Fratzl P, Klaushofer K. Alendronate increases degree and uniformity of mineralization in cancellous bone and decreases the porosity in cortical bone of osteoporotic women. Bone 2001;29(2):185–91.

[28] Zoehrer R, Roschger P, Durchschlag E, Fratzl P, Paschalis E, Recker R, et al. Bone mineralization density distribution in triple biopsies of the iliac crest in post-menopausal women. J Bone Miner Res 2006;21 (7):1106–12.

[29] Borah B, Dufresne TE, Ritman EL, Jorgensen SM, Liu S, Chmielewski PA, et al. Long-term risedronate treatment normalizes mineralization and continues to preserve trabecular architecture: sequential triple biopsy studies with micro-computed tomography. Bone 2006;39(2):345–52.

[30] Strogatz SH. Nonlinear dynamics and chaos. Perseus Books Publishing; 2000. p. 305–6.

[31] Murray JD. Mathematical Biology. Springer; 2002. p. 36–7. [Since the aging velocity is constant, the conservation law is simplied.].
[32] Boyde A, Travers R, Glorieux FH, Jones SJ. The mineralization density of iliac crest bone from children with osteogenesis imperfecta. Calcif Tissue Int 1999;64(3):185–90.
[33] Weber M, Roschger P, Fratzl-Zelman N, Schöberl T, Rauch F, Glorieux HF, et al. Pamidronate does not adversely affect bone intrinsic material properties in children with osteogenesis imperfecta. Bone 2006; 39:616–22.
[34] Burr D. Microdamage and bone strength. Osteoporosis Int 2003;14: S67–72.
[35] Schaffler MB. Role of bone turnover in microdamage. Osteoporosis Int 2003;14:S73–7.
[36] Eriksen EF, Melsen F, Sod E, Barton I, Chines A. Effects of long-term risedronate on bone quality and bone turnover in women with postmenopausal osteoporosis. Bone 2002;31(5):620–5.
[37] Roschger P, Fratzl P, Eschberger J, Klaushofer K. Response to the letter to the editor by E.G. Vajda and J.G. Skedros. Bone 1999;24(6): 620–621.
[38] Boivin GY, Chavassieux PM, Santora AC, Yates J, Meunier PJ. Alendronate increases bone strength by increasing the mean degree of mineralization of bone tissue in osteoporotic women. Bone 2000;27 (5):687–94.

Bibliography

[1] Galileo Galilei. *Dialogues Concerning Two New Sciences*. Northwestern University Press, 1939.

[2] J.D. Currey. *Bones - structure and mechanics*. Princeton University Press, 2002.

[3] D.R. Carter and G.S. Beaupre. *Skeletal function and form*. Cambridge University Press, 2001.

[4] S. Weiner and H.D. Wagner. The material bone: structure-mechanical function realations. *Annual Review of Material Science*, 28:271–98, 1998.

[5] A.J. Hodge AJ and J.A. Petruska. *Aspects of protein structure*. Academic Press, 1963.

[6] W.J. Landis, K.J. Hodgens, J. Arena, M.J. Song, and B.F. McEwen. Structural relations between collagen and mineral in bone as determined by high voltage electron microscopic tomography. *Microscopy Research and Technique*, 33:192–202, 1996.

[7] S.W. White, D.J.S. Hulmes, A. Miller, and P.A. Timmins. Collagen-mineral axial relationship in calcified turkey leg 785 tendon by x-ray and neutron-diffraction. *Nature*, 266:421–5, 1977.

[8] K.E. Kadler, D.F.T. Holmes, and J.A. Chapman. Collagen fibril formation. *Biochemical Journal*, 316:111, 1996.

[9] E.P. Paschalis, K. Verdelis, S.B. Doty, and A.L. Boskey. Spectroscopic characterization of collagen cross-links in bone. *Journal of Bone and Mineral Research*, 16:1821–28, 2001.

[10] L. Knott and A.J. Bailey. Collagen cross-links in mineralizing tissues: A review of their chemistry, function, and clinical relevance. *Bone*, 22:18187, 1998.

[11] J. Koewitz, M. Knippel, T Schuhr, and J. Mach. Alteration in the extent of collagen i hydroxylation, isolated from femoral heads of women with a femoral neck fracture caused by osteoporosis. *Calcified Tissue International*, 60:501–5, 1997.

[12] X. Banse, T.J. Sims, and A.J. Bailey. Mechanical properties of adult vertebral cancellous bone: Correlation with collagen intermolecular cross-links. *Journal of Bone and Mineral Research*, 17:1621–28, 2002.

[13] P. Fratzl, H. S. Gupta, E. P. Paschalis, and P. Roschger. Structure and mechanical quality of the collagenmineral nano-composite in bone. *Journal of Material Chemistry*, 14:2115–23, 2004.

[14] S. Mann. *Biomineralization. Principles and concepts in bioinorganic materials chemistry*. Oxford University Press, 2001.

[15] E.P. Paschalis, F. Betts, E. DiCarlo, R. Mendelsohn, and A.L. Boskey. Ftir microspectroscopic analysis of normal human cortical and trabecular bone. *Calcified Tissue International*, 61:480–486, 1997.

[16] O. Akkus, F. Adar, and M.B. Schaffler. Age-related changes in physicochemical properties of mineral crystals are related to impaired mechanical function of cortical bone. *Bone*, 34:443–53, 2004.

[17] J. Aizenberg, S. Albeck, S. Weiner, and L. Addadi. Crystal protein interactions studied by overgrowth of calcite on biogenic skeletal elements. *Journal of Crystal Growth*, 142:156–64, 1994.

[18] W.J. Landis. Mineral characterization in calcifying tissues: atomic, molecular and macromolecular perspectives. *Connective Tissue International*, 35:1–8, 1996.

[19] W. Traub, T. Arad, and S. Weiner. Origin of mineral crystal-growth in collagen fibrils. *Matrix*, 12:251–5, 1992.

[20] P. Fratzl, N. Fratzl-Zelman, K. Klaushofer, G. Vogl, and K. Koller. Nucleation and growth of mineral crystals in bone studied by small-angle x-ray scattering. *Calcified Tissue International*, 48:407–13, 1991.

[21] A. Boskey. Bone mineral crystal size. *Osteoporosis International*, 14:S16–S21, 2003.

[22] T. Hassenkam, G.E. Fantner, J.A. Cutroni, J.C. Weaver, D.E. Morse, and P.K. Hansma. High-resolution afm imaging of intact and fractured trabecular bone. *Bone*, 35:4–10, 2004.

[23] P. Fratzl and R. Weinkamer. Natures hierarchical materials. *Progress in Materials Science*, In Press, 2007.

[24] S. Lees and H.A. Mook. Equatorial diffraction spacing as a function of water-content in fully mineralized cow bone determined by neutron-diffraction. *Calcified Tissue International*, 39:291–2, 1986.

[25] P. Fratzl, N. Fratzl-Zelman, and K. Klaushofer. Collagen packing and mineralization an x-ray-scattering investigation of turkey leg tendon. *Biophysical Journal*, 64:260–6, 1993.

[26] H.S. Gupta, J. Seto, W. Wagermaier, P. Zaslansky, P. Boesecke, and P. Fratzl. Cooperative deformation of mineral and collagen in bone at the nanoscale. *Proceedings of the National Academic of Science*, 103:17741–6, 2006.

[27] M.F. Ashby, L.J. Gibson LJ, U. Wegst, and R. Olive. The mechanical-properties of natural materials. 1. material property charts. *Proceedings of the Royal Society of London*, 450:123–40, 1995.

[28] U.G.K. Wegst and M.F. Ashby. The mechanical efficiency of natural materials. *Philosphical Magazine*, 84:2167–81, 2004.

[29] I. Jaeger and P. Fratzl. Mineralized collagen fibrils: A mechanical model with a staggered arrangement of mineral particles. *Biophysical Journal*, 79:173746, 2000.

[30] H. Gao, B. Ji, I. Jaeger, E. Arzt, and P. Fratzl. Materials become insensitive to flaws at nanoscale: lessons from nature. *Proceedings of the National Academic of Science*, 100:5597–5600, 2003.

[31] H.S. Gupta, W. Wagermaier, G. Zickler, D.R. Aroush, S.S. Funari, P. Roschger, H.D. Wagner, and P. Fratzl. Nanoscale deformation mechanisms in bone. *Nano Letters*, 5:2108–11, 2005.

[32] R.P. Heaney. Remodeling and skeletal fragility. *Osteoporosis International*, 14:S12–15, 2003.

[33] R. Huiskes, R. Ruimerman, G. H. van Lenthe, and J. D. Janssen. Effects of mechanical forces on maintenance and adaptation of form in trabecular bone. *Nature*, 405:704, 2000.

[34] H.M. Frost. Bone "mass" and the "mechanostat": a proposal. *Anatomical Record*, 219:1–9, 1987.

[35] D.B. Burr. Targeted and nontargeted remodeling. *Bone*, 30:2–4, 2002.

[36] A. M. Parfitt. Misconceptions (3): calcium leaves bone only by resorption and enters only by formation. *Bone*, 33:259–63, 2003.

[37] M.J. Favus, editor. *Primer on the metabolic bone diseases and disorders of mineral metabolism*. American society for bone and mineral research, 1999.

[38] W.S.S. Jee. *Bone mechanics handbook*, chapter Integrated bone tissue physiology: anatomy and physiology.

[39] A.M. Parfitt. What is the normal rate of bone remodeling? *Bone*, 35:1–3, 2004.

[40] R.S. Weinstein and S.C. Manolagas. Apoptosis and osteoporosis. *American Journal of The Medical Sciences*, 108:153–64, 2000.

[41] L.M. McNamara, J.C. Van der Linden, H. Weinans, and P.J. Prendergast. Stress-concentrating effect of resorption lacunae in trabecular bone. *Journal of Biomechanics*, 39:734–41, 2006.

[42] E. Seeman. Pathogenesis of bone fragility in women and men. *Lancet*, 359:1841–50, 2002.

[43] S. Vajjhala, A.M. Kraynik, and L.J. Gibson. A cellular solid model for modulus reduction due to resorption of trabeculae in bone. *Journal of Biomechanical Engineering*, 122:511–515, 2000.

[44] D.B. Burr. Microdamage and bone strength. *Osteoporosis International*, 14:S67–72, 2003.

[45] T. Mashiba, C.H. Turner, T. Hirano, M.R. Forwood, C.C. Johnston, and D.B. Burr DB. Effects of suppressed bone turnover by bisphosphonates on microdamage accumulation and biomechanical properties in clinically relevant skeletal sites in beagles. *Bone*, 28:524–31, 2001.

[46] R. Zoehrer, P. Roschger, E.P. Paschalis, J.G. Hofstaetter, E. Durchschlag, P. Fratzl, R. Phipps, and K. Klaushofer. Effects of 3- and 5-year treatment with risedronate on bone mineralization density distribution in triple biopsies of the iliac crest in postmenopausal women. *Journal of Bone and Mineral Research*, 21:1106–12, 2006.

[47] D. Ruffoni, P. Fratzl, P. Roschger, K. Klaushofer, and R. Weinkamer. The bone mineralization density distribution as a fingerprint of the mineralization process. *Bone*, 40:1308–19, 2007.

[48] C.H. Turner. Biomechanics of bone: Determinants of skeletal fragility and bone quality. *Osteoporosis International*, 13:97–104, 2002.

[49] N.B. Watts. Clinical utility of biochemical markers of bone remodeling. *Clinical Chemistry*, 45:1359–68, 1999.

[50] A. M. Parfitt, M. K. Drezner, F. H. Glorieux, J. A. Kanis, H. Malluche, P.J. Meunier, S.M. Ott, and R. Recker. Bone histomorphometry: standardization of nomenclature, symbols, and units. *Journal of Bone and Mineral Research*, 2:595–610, 1987.

[51] E.F. Eriksen, F. Melsen, E. Sod, I. Barton, and A. Chines. Effects of long-term risedronate on bone quality and bone turnover in women with postmenopausal osteoporosis. *Bone*, 31:620–5, 2002.

[52] B. Borah, E.L. Ritman, T.E. Dufresne, S.M. Jorgensen, S.L. Liu, J.Sacha, R.J. Phipps, and R.T. Turner. The effect of risedronate on bone mineralization as measured by micro-computed tomography with synchrotron radiation: Correlation to histomorphometric indices of turnover. *Bone*, 37:1–9, 2005.

[53] M.R. Allen and D.B. Burr. Mineralization, microdamage, and matrix: how bisphosphonates influence material properties of bone. *BoneKey-Osteovision*, 4:49–60, 2007.

[54] P. Garnero, E. SornayRendu, M.C. Chapuy, and P.D. Delmas. Increased bone turnover in late postmenopausal women is a major determinant of osteoporosis. *Journal of Bone and Mineral Research*, 11:337–349, 1996.

[55] J.C. van der Linden, J.A. Verhaar, H.A. Pols, , and H. Weinans. A simulation model at trabecular level to predict effects of antiresorptive treatment after menopause. *Calcified Tissue International*, 73:537–44, 2003.

[56] R. Recker, J. Lappe, K.M. Davies, and R. Heaney. Bone remodeling increases substantially in the years after manopause and remains increased in older osteoporosis patients. *Journal of Bone and Mineral Research*, 19:1628–33, 2004.

[57] H. Tsangari, D.M. Findlay, and N.L. Fazzalari. Structural and remodeling indices in the cancellous bone of the proximal femur across adulthood. *Bone*, 40:211–217, 2007.

[58] P.D. Delmas. Different effects of antiresorptive therapies on vertebral and non-vertebral fractures in postmenopausal osteoporosis. *Bone*, 30:14–7, 2002.

[59] J.J. Stepan, F. Alenfeld, G. Boivin, J.H.M. Feyen, and P. Lakatos. Mechanism of action of antiresorptive therapies of postmenopausal osteoporosis. *Endocrine Regulations*, 37:227–40, 2003.

[60] D.D. Mellstrom, O.H. Sorensen, S. Goemaere, C. Roux, T.D. Johnson, and A.A. Chines. Seven years of treatment with risedronate in women with postmenopausal osteoporosis. *Calcified Tissue International*, 75:662–68, 2004.

[61] B. Borah, T.E. Dufresne, P.A. Chmielewski, T.D. Johnson, A. Chines, and M.D. Manhart. Risedronate preserves bone architecture in postmenopausal women with osteoporosis as measured by three-dimensional microcomputed tomography. *Bone*, 34:736–46, 2004.

[62] G. Boivin and P.J. Meunier. The degree of mineralization of bone tissue measured by computerized quantitative contact microradiography. *Calcified Tissue International*, 70:503–511, 2002.

[63] P. Roschger, B.M. Grabner, S. Rinnerthaler, W. Tesch, M. Kneissel, A. Berzlanovich, K. Klaushofer, and P. Fratzl. Structural development of the mineralized tissue in the human l4 vertebral body. *Journal of Structural Biology*, 136:126–36, 2001.

[64] S. Weiner, I. Sagi, and L. Addadi. Choosing the crystallization path less traveled. *Science*, 309:1027–28, 2005.

[65] J. Aizenberg, J.C. Weaver, M.S. Thanawala, V.C. Sundar, D.E. Morse, and P. Fratzl. Skeleton of euplectella sp.: structural hierarchy from the nanoscale to the macroscale. *Science*, 309:275–78, 2005.

[66] A.W. Xu, Y.R. Ma, and H. Colfen. Biomimetic mineralization. *Journal of Materials Chemistry*, 5:415–49, 2007.

[67] M.J. Glimcher. Molecular biology of mineralized tissue with particular reference to bone. *Reviews of Modern Physics*, 31:359, 1959.

[68] A.L. Boskey, M. Maresca, W. Ullrich, S.B. Doty, W.T. Butler, and C.W. Prince. Osteopontin-hydroxyapatite interactions in vitro: inhibition of hydroxyapatite formation and growth in a gelatin-gel. *Bone and Mineral*, 22:147, 1993.

[69] C. Schafer, A. Heiss, A. Schwarz, R. Westenfeld, M. Ketteler, J. Floege, W. Muller-Esterl, T. Schinke, and W. Jahnen Dechent. The serum protein alpha(2)-heremans-schmid glycoprotein/fetuin-a is a systemically acting inhibitor of ectopic calcification. *Journal of Clinical Investigation*, 112:357–66, 2003.

[70] A.L. Boskey. *Bone mechanics handbook*, chapter Bone Mineralization.

[71] W.G. Cole. The molecular pathology of osteogenesis imperfecta. *Clinical Orthopaedics and related research*, 343:235, 1997.

[72] K. Misof, W. J. Landis, K. Klaushofer, and P. Fratzl. Collagen from the osteogenesis imperfecta mouse model (oim) shows reduced resistance against tensile stress. *Journal of Clinical Investigation*, 100:40, 1997.

[73] P. Roschger, P. Fratzl, J. Eschberger, and K. Klaushofer. Validation of quantitative backscattered electron imaging for the measurement of mineral density distribution in human bone biopsies. *Bone*, 23:319–26, 1998.

[74] P. Fratzl, P. Roschger, N. Fratzl Zelman, E.P. Paschalis, R. Phipps, and K. Klaushofer. Evidence that treatment with risedronate in women with postmenopausal osteoporosis affects bone mineralization and bone volume. *Calcified Tissue International*, DOI 10.1007/s00223-007-9039-8, 2007.

[75] S. Nuzzo, M.H. Lafage-Proust, E. Martin-Basoda, G. Boivin, T. Thomas, C. Alexandre, and et al. Synchrotron radiation microtomography allows the analysis of three-dimensional microarchitecture and degree of mineralization of human iliac crest biopsy specimens: effects of etidronate treatment. *Journal of Bone and Mineral Research*, 17:1372–82, 2002.

[76] K.N. Bachus and R.D. Bloebaum. Projection effect errors in biomaterials and bone research. *Cells and Materials*, 2:347–55, 1992.

[77] B. Borah, T.E. Dufresne, E.L. Ritman, S.M. Jorgensen, S. Liu, P.A. Chmielewski, R.J. Phipps, X. Zhou, J.D. Sibonga, and R.T. Turner. Long-term risedronate treatment normalizes mineralization and continues to preserve trabecular architecture: Sequential triple biopsy studies with micro-computed tomography. *Bone*, 39:345–52, 2006.

[78] J. I.Goldstein, D. E. Newbury, P. Echlin, D. C. Joy, A. D. Romig, Jr., C. E. Lyman, C. Fiori, and E. Lifshin. *Scanning Electron Microscopy and X-Ray Microanalysis*.

[79] P. Roschger, H.S. Gupta, A. Berzlanovich, G. Ittner, D.W. Dempster, P. Fratzl, and et al. Constant mineralization density distribution in cancellous human bone. *Bone*, 32:316–23, 2003.

[80] R.J. LeVeque. *Finite Volume Methods for Hyperbolic Problems*. Cambridge University Press, 2002.

[81] R. Recker, J. Lappe, K.M. Davies, and R. Heaney. Characterization of perimenopausal bone loss: A prospective study. *Journal of Bone and Mineral Research*, 15:1965–73, 2000.

[82] J.C. van der Linden, D.H. Birkenhaeger-Frenkel, J.A.N. Verhaar, and H. Weinans. Trabecular bones mechanical properties are affected by its non-uniform mineral distribution. *Journal of Biomechanics*, 34:1573–80, 2001.

[83] R. Huiskes. If bone is the answer, then what is the question? *Journal of Anatomy*, 197:145–56, 2000.

[84] L.J. Gibson and M.F. Ashby. *Cellular solids: structure and properties.* Cambridge University Press, 1997.

[85] S. Torquato. *Random heterogeneous materials: microstructure and macroscopic properties.* Springer, 2002.

[86] S.R. Deans. *The Radon Transform and Some of Its Applications.* John Wiley and Sons, 1983.

[87] P.J. Thurner, P. Wyss, R. Voide, M. Stauber, M. Stampanoni, U. Sennhauser, and R. Mller. Time-lapsed investigation of three-dimensional failure and damage accumulation in trabecular bone using synchrotron light. *Bone*, 39:28999, 2006.

[88] J.H. Waarsing, J.S. Day, J.C. van der Linden, A.G. Ederveen, C. Spanjers, N. De Clerck, A. Sasov, J.A.N. Verhaar, and H. Weinans. Detecting and tracking local changes in the tibiae of individual rats: a novel method to analyse longitudinal in vivo micro-ct data. *Bone*, 34:163–169, 2004.

[89] A. Nazarian and R. Mueller. Time-lapsed microstructural imaging of bone failure behavior. *Journal of Biomechanics*, 37:55–65, 2004.

[90] M.J. Silva and L.J. Gibson. Modeling the mechanical behavior of vertebral trabecular bone: effects of age-related changes in microstructure. *Bone*, 21:191–99, 1997.

[91] M.J. Silva and L.J. Gibson. The effects of non-periodic microstructure and defects on the compressive strength of two dimensional cellular solids. *International Journal of Mechanical Science*, 39:549–63, 1997.

[92] S. Boutroy, M.L. Bouxsein, F. Munoz, and P.D. Delmas. Non invasive measurement of trabecular architecture by 3d-pqct discriminates osteopenic women with and without fractures. *Journal of Bone and Mineral Research*, 9:S91, 2005.

[93] J.A. Hipp, A. Jansujwicz, C.A. Simmons, and B.D. Snyder. Trabecular bone morphology from micro-magnetic resonance imaging. *Journal of Bone and Mineral Research*, 11:286–92, 1996.

[94] T.M. Link, S. Majumdar, P. Augat, J.C. Lin, D. Newitt, Y. Lu, N.E. Lane, and H.K. Genant. In vivo high resolution mri of the calcaneus: Differences in trabecular structure in osteoporosis patients. *Journal of Bone and Mineral Research*, 13:1175–82, 1998.

[95] T. Hildebrand and P. Ruegsegger. A new method for the model-independent assesment of thickness in three dimensional images. *Journal of Microscopy*, 185:67–75, 1997.

[96] M Stauber and R. Mueller. Volumetric spatial decomposition of trabecular bone into rods and plates - a new method for local bone morphometry. *Bone*, 38:475–484, 2006.

[97] P. Saparin, J.S. Thomsen, S. Prohaska, A. Zaikin, J. Kurths, H.C. Hege, and Wolfgang Gowin. Quantification of spatial structure of human proximal tibial bone biopsies using 3d measures of complexity. *Acta Astronautica*, 56:820–830, 2005.

[98] N. Marwan, P. Saparin, and J. Kurths. Measures of complexity for 3d image analysis of trabecular bone. *European Physical Journal - Special Topics*, 143:109–116, 2007.

[99] N. Marwan, J. Kurths, and P. Saparin. Generalised recurrence plot analysis for spatial data. *Physics Letters A*, 360:545–551, 2007.

[100] A. Odgaard. *Bone mechanics handbook*, chapter Quantification of cancellous bone architecture.

[101] W.J. Whitehouse. The quantitative morphology of anisotropic trabecular bone. *Journal of Microscopy*, 101:153–68, 1974.

[102] A. Odgaard and H.J. Gundersen. Quantification of connectivity in cancellous bone, with special emphasis on 3-d reconstructions. *Bone*, 14:173–82, 1993.

[103] P.K. Saha and B.B. Chaudhuri. 3d digital topology under binary transformation with applications. *Computer Vision and Image Understanding*, 63:418–29, 1996.

[104] M. Stauber, L. Rapillard, G.H. van Lenthe, P. Zysset, and R. Mueller. Importance of individual rods and plates in the assessment of bone quality and their contribution to bone stiffness. *Journal of Bone and Mineral Research*, 21:586–95, 2006.

[105] T. Hildebrand and P. Ruegsegger. Quantification of bone microarchitecture with the structure model index. *Computer Methods in Biomechanics and Biomedical Engineering*, 1:15–23, 1997.

[106] C.H. Turner and D.B. Burr. Basic biomechanical measurements of bone: a tutorial. *Bone*, 14:595–608, 1993.

[107] T.M. Keaveny, E.F. Wachtel, C.M. Ford, and W.C. Hayes. Differences between the tensile and compressive strengths of bovine tibial trabecular bone depend on modulus. *Journal of Biomechanics*, 27:1137–46, 1994.

[108] T.M. Keaveny, T.P. Pinilla, R.P. Crawford, D.L. Kopperdahl, and A. Lou. Systematic and random errors in compression testing of trabecular bone. *Journal of Orthopaedic Research*, 15:101–10, 1997.

[109] B. Borah, G.J. Gross, T.E. Dufresne, T.S. Smith, M.D. Cockman, P.A. Chmielewski, M.W. Lundy, J.R. Hartke, and E.W. Sod. Three-dimensional microimaging (mrmi and mct), finite element modeling, and rapid prototyping provide unique insights into bone architecture in osteoporosis. *The Anatomical Record*, 265:101–110, 2001.

[110] A Woesz, J. Stampfl, and P. Fratzl. Cellular solids beyond the apparent density - an experimental assessment of mechanical properties. *Advanced Enineering Materials*, 6:134–38, 2004.

[111] O.C. Zienkiewicz. *The Finite Element Method*. McGraw Hill Higher Education, 1977.

[112] G.L. Niebur, M.J. Feldstein, J.C. Yuen, T.J. Chen, and T.M. Keaveny. High-resolution finite element models with tissue strength asymmetry accurately predict failure of trabecular bone. *Journal of Biomechanics*, 33:1575–83, 2000.

[113] J. Homminga, B. van Rietbergen, E.M. Lochmueller, c.H. Weinans, F. Eckstein, and R. Huiskes. The osteoporotic vertebral structure is well adapted to the loads of daily life, but not to infrequent error loads. *Bone*, 34:510–16, 2004.

[114] G.H. van Lenthe, M. Stauber, and R. Mller. Specimen-specific beam models for fast and accurate prediction of human trabecular bone mechanical properties. *Bone*, 39:1182–89, 2006.

[115] G.H. Gunaratne, C.S. Rajapaksa, K.E. Bassler, K.K. Mohanty, and S.J. Wimalawansa. Model for bone strength and osteoporotic fractures. *Physical Review Letters*, 88:068101, 2002.

[116] C.S. Rajapakse, J.S. Thomsen, J.S.E. Ortiz, S.J. Wimalawansa, E.N. Ebbesen, L. Mosekilde, and G.H. Gunaratne. An expression relating breaking stress and density of trabecular bone. *Journal of Biomechanics*, 37:1241–1249, 2004.

[117] T.P. Harrigan, M. Jasty, R.W. Mann, and W.H. Harris. Limitations of the continuum assumption in cancellous bone. *Journal of Biomechanics*, 21:269–75, 1988.

[118] G.Y. Yang, J. Kabel, B. Van Rietbergen, A. Odgaard, R. Huiskes, and S.C. Cowin. The anisotropic hookes law for cancellous bone and wood. *Journal of Elasticity*, 53:125–46, 1999.

[119] S.C. Cowin. The relationship between the elasticity tensor and the fabric tensor. *Mechanics of Materials*, 4:137–147, 1985.

[120] J. Homminga, B.R. Mccreadie, H.Weinans, and R. Huiskes. The dependence of the elastic properties of osteoporotic cancellous bone on volume fraction and fabric. *Journal of Biomechanics*, 36:1461–67, 2003.

[121] P.K. Zysset and A. Curnier. An alternative model for anisotropic elasticity based on fabric tensor. *Mechanics of Materials*, 21:243–250, 1995.

[122] J. Kabel, B. van Rietbergen, A. Odgaard, and R. Huiskes. Constitutive relationships of fabric, density, and elastic properties in cancellous bone architecture. *Bone*, 25:481–86, 1999.

[123] P.K. Zysset, R.W. Goulet, and S.J. Hollister. A global relationship between trabecular bone morphology and homogenized elastic properties. *Journal of Biomechanical Engineering*, 120:640–46, 1998.

[124] J. Kabel, B. van Rietbergen, A. Odgaard, and R. Huiskes. Connectivity and the elastic properties of cancellous bone. *Bone*, 24:115–20, 1999.

[125] J.H. Kinney and A.J.C. Ladd. The relationship between three-dimensional connectivity and the elastic properties of trabecular bone. *Journal of Bone and Mineral Research*, 13:839–45, 1998.

[126] V.S. Deshpande, M.F. Ashby, and N.A. Fleck. Foam topology bending versus stretching dominated architecture. *Acta materialia*, 49:1035–40, 2001.

[127] D.W. Overaker, A.M. Cuitino, and N.A. Langrana. Elastoplastic micromechanical modeling of two-dimensional irregular convex and nonconvex (re-entrant) hexagonal foams. *Journal of Applied Mechanics*, 65:748–57, 1998.

[128] R.S. Kumar and D.L. McDowell. Generalized continuum modeling of 2-d periodic cellular solids. *International Journal of Solids and Structures*, 41:7399–7422, 2004.

[129] M.J. Silva, W.C. Hayes, and L.J. Gibson. The effects of non-periodic microstructure on the elastic properties of two-dimensional cellular solids. *International Journal of Mechanical Science*, 37:1161–77, 1995.

[130] P.R. Onck, E.W. Andrews, and L.J. Gibson. Size effects in ductile cellular solids. part one: modeling. *International Journal of Mechanical Sciences*, 43:681–699, 2001.

[131] C. Chen, T.J. Lu, and N.A. Fleck. Effect of imperfections on the yielding of two-dimensional foams. *Journal of the Mechanics and Physics of Solids*, 47:2235–72, 1999.

[132] R. Weinkamer, M.A. Hartmann, Y. Brechet, and P. Fratzl. Stochastic lattice model for bone remodeling and aging. *Physical Review Letters*, 93:228102, 2004.

Acknowledgements

First of all I would like to thank my supervisor and friend Richard (Ricci) Weinkamer for the excellent support, the enthusiasm and the patience he had during the supervision of my work. Working together with Ricci has been really a pleasure and, in addition to the exciting scientific discussions, I will remember the pleasant moments we had in Geneva, Prague and Ischia. I am grateful to Peter Fratzl for giving me the opportunity to work in his department at the Max Planck Institute of Colloids and Interfaces, and especially for always finding time for really excellent discussions. I would like to thank my office mate Monika for a very pleasant climate in the office and for all the help she gave me with the German language. John (JD) and Markus (Markuccio) were really essential both from the scientific side and for their friendship. I mention my personal gratitude to all members of the Biomaterial department, to Angelo and to the Marie Curie program for financial support. Last but not least I thank my girlfriend Palmy, my friend Antonio and my parents.